Ph.D. Dissertation

International Doctoral School in Information

and Communication Technology

DISI - University of Trento

Innovative Tiling Methodologies for the Synthesis of Phased Array Antennas for Advanced Radar and Communications Systems

Nicola Anselmi

Advisor:
Giacomo Oliveri, Aggregate Professor
University of Trento

April 2018

To my parents Marisa and Sergio, my sister Elena, and to my colleagues and friends of the ELEDIA Research Center. Thank you all.

Abstract

In this work, the synthesis of clustered phased array antennas characterized by an irregular organization of tiles modules is addressed. By exploiting tiling theorems drawn from the mathematical theory, optimal and sub-optimal methods for the optimization of tiles arrangements and the corresponding excitations minimizing user-defined cost functions are presented. An enumerative approach able to retrieve the optimal clustering providing the maximum aperture coverage and the best radiation performance is proposed to deal with the synthesis of low/medium-size arrays. Based on the same optimal theorems and still exploiting the algorithmic procedures at the basis of the enumerative approach, an innovative schemata-based optimization method is introduced for designing large arrays, as well. A set of numerical examples and full-wave simulations, concerned with different aperture sizes, is reported to assess the effectiveness, the limitations, and the ranges of computationally-admissible applicability of the proposed methods.

Published Journals Papers

[R1]   P. Rocca, L. Manica, N. Anselmi, and A. Massa, "Analysis of the pattern tolerances in linear arrays with arbitrary amplitude errors," *IEEE Antennas and Wireless Propagation Letters*, vol. 12, no. 1, pp. 639-642, May 2013.

[R2]   L. Manica, N. Anselmi, P. Rocca, and A. Massa, "Robust mask-constrained linear array synthesis through an interval-based particle swarm," *IET Microwaves, Antennas & Propagation*, vol. 7, no. 12, pp. 976-984, 2013.

[R3]   N. Anselmi, L. Manica, P. Rocca, and A. Massa, "Tolerance analysis of antenna arrays through interval arithmetic," *IEEE Transactions on Antennas and Propagation*, vol. 61, no 11, pp. 5496-5507, Aug. 2013.

[R4]   P. Rocca, L. Manica, N. Anselmi, and A. Massa, "Optimal synthesis of robust beamformer weights exploiting interval analysis and convex optimization," *IEEE Transactions on Antennas and Propagation*, vol. 62, no. 7, pp. 3603-3612, Jul. 2014.

[R5]   T. Moryama, L. Poli, N. Anselmi, M. Salucci, and P. Rocca, "Real array pattern tolerances from amplitude excitation errors," *IEICE Electronics Express*, vol. 11, no. 17, pp 1-8, Aug. 2014.

[R6]   G. Oliveri, N. Anselmi, and A. Massa, "Compressive sensing imaging of non-sparse 2D scatterers by a total-variation approach within the born approximation," *IEEE Transactions on Antennas and Propagation*, vol. 62, no. 10, pp. 5157-5170, Oct. 2014.

[R7]   P. Rocca, N. Anselmi, and A. Massa, "Interval arithmetic for pattern tolerance analysis of parabolic reflectors," *IEEE Transactions on Antennas and Propagation*, vol. 62, no. 10, pp. 4952-4960, Oct. 2014.

[R8]   G. Oliveri, F. Viani, N. Anselmi, and A. Massa, "Synthesis of multi-layer WAIM coatings for planar phased arrays within the system-by-design framework," *IEEE Transactions on Antennas and Propagation*, vol. 63, no. 6, pp. 2482-2495, Jun. 2015.

[R9]   L. Poli, P. Rocca, N. Anselmi, and A. Massa, "Dealing with uncertainties on phase weighting of linear antenna arrays by means of interval-based tolerance analysis," *IEEE Transactions on Antennas and Propagation*, vol. 63, no. 7, pp. 3229-3224, Jul. 2015.

[R10] N. Anselmi, G. Oliveri, and A. Massa, "Wavelet-based compressive imaging of sparse targets," *IEEE Transactions on Antennas and Propagation*, vol. 63, no. 11, pp. 4889-4900, Nov. 2015.

[R11] N. Anselmi, P. Rocca, M. Salucci, and A. Massa, "Optimization of excitation tolerances for robust beamforming in linear arrays," *IET Microwaves, Antennas & Propagation*, vol. 10, no. 2, pp. 208-214, Jan. 2016.

[R12] P. Rocca, L. Poli, N. Anselmi, M. Salucci, and A. Massa, "Predicting antenna pattern degradations in microstrip reflectarrays through interval arithmetic" *IET Microwaves, Antennas & Propagation*, vol. 10, no. 8, pp. 817-826, May 2016.

[R13] N. Anselmi, M. Salucci, P. Rocca, and A. Massa, "Generalized interval-based analysis tool for pattern distortions in reflector antennas with bump-like surface deformations" *IET Microwaves, Antennas & Propagation*, vol. 10, no. 9, pp. 909-916, June 2016.

[R14] N. Anselmi, M. Salucci, P. Rocca, and A. Massa, "Power pattern sensitivity to calibration errors and mutual coupling in linear arrays through circular interval arithmetics" *Sensors*, vol. 16, no. 6, 791, 2016.

[R15] M. Salucci, N. Anselmi, G. Oliveri, and A. Massa, "Real-time NDT-NDE through an innovative adaptive partial least squares SVR inversion approach," *IEEE Transactions on Geoscience and Remote Sensing*, vol. 54, no. 11, pp. 6818-6832, Nov. 2016.

[R16] L. Tenuti, N. Anselmi, P. Rocca, M. Salucci, and A. Massa, "Minkowski sum method for planar arrays sensitivity analysis with uncertain-but-bounded excitation tolerances," *IEEE Transactions on Antennas and Propagation*, vol. 65, no. 1, pp. 167-177, Jan. 2017.

[R17] F. Viani, A. Polo, P. Garofalo, N. Anselmi, M. Salucci, and E. Giarola, "Evolutionary optimization applied to wireless smart lighting in energy-efficient museums," *IEEE Sensors Journal*, vol. 17, no. 5, pp. 1213-1214, Mar. 2017.

[R18] M. Salucci, L. Poli, N. Anselmi, and A. Massa, "Multi-frequency particle swarm optimization for enhanced multi-resolution GPR microwave imaging," *IEEE Transactions on Geoscience and Remote Sensing*, vol. 55, no. 3, pp. 1305-1317, Mar. 2017.

[R19] N. Anselmi, G. Oliveri, M. A. Hannan, M. Salucci, and A. Massa, "Color compressive sensing imaging of arbitrary shaped scatterers,"

IEEE Transaction on Microwave Theory and Techniques, vol. 65, no. 6, pp. 1986-1999, Jun. 2017.

[R20]   G. Oliveri, M. Salucci, N. Anselmi, and A. Massa, "Compressive Sensing as applied to inverse problems for imaging: theory, applications, current trends, and open challenges," *IEEE Antennas and Propagation Magazine* - Special Issue on "Electromagnetic Inverse Problems for Sensing and Imaging," vol. 59, no. 5, pp. 34-46, Oct. 2017.

[R21]   M. Salucci, G. Oliveri, N. Anselmi, F. Viani, A. Fedeli, M. Pastorino, and A. Randazzo, "Three-dimensional electromagnetic imaging of dielectric targets by means of the multiscaling inexact-Newton method," *Journal of Optical Society of America A*, vol. 34, no. 7, pp. 1119-1131, Jul. 2017.

[R22]   N. Anselmi, P. Rocca, M. Salucci, and A. Massa, "Irregular phased array tiling by means of analytic schemata-driven optimization," *IEEE Transactions on Antennas and Propagation*, vol. 65, no. 9, pp. 4495-4510, Sep. 2017.

[R23]   G. Oliveri, M. Salucci, N. Anselmi and A. Massa, "Multiscale system-by-design synthesis of printed WAIMs for waveguide array enhancement," in *IEEE Journal on Multiscale and Multiphysics Computational Techniques*, vol. 2, pp. 84-96, 2017.

[R24]   M. Salucci, G. Gottardi, N. Anselmi, and G. Oliveri, "Planar thinned array design by hybrid analytical-stochastic optimization," *IET Microwaves, Antennas & Propagation*, vol. 11, no. 13, pp. 1841-1845, Oct. 2017.

[R25]   A. Massa, G. Oliveri, M. Salucci, N. Anselmi, and P. Rocca, "Learning-by-examples techniques as applied to electromagnetics," *Journal of Electromagnetic Waves and Applications*, Invited Review Article, pp. 1-16, 2017.

[R26]   M. Salucci, G. Oliveri, N. Anselmi, G. Gottardi, and A. Massa, "Performance enhancement of linear active electronically-scanned arrays by means of MbD-synthesized metalenses," *Journal of Electromagnetic Waves and Applications*, vol. 32, no. 8, pp. 927-955, 2018.

[R27]   G. Oliveri, M. Salucci, and N. Anselmi, "Tomographic imaging of sparse low-contrast targets in harsh environments through matrix completion," *IEEE Transactions on Microwave Theory and Techniques*, in press.

[R28]   N. Anselmi, L. Poli, G. Oliveri, and A. Massa, "Iterative multi-resolution Bayesian CS for microwave imaging," *IEEE Transactions on Antennas and Propagation*, in press.

Published Book Chapters

[B1]   A. Massa, G. Oliveri, P. Rocca, N. Anselmi, and M. Salucci, "Technologies of antenna and phased array for wireless power transfer via radio waves," Wireless Power Transfer - Theory, Technology, and Applications - Series "Studies in Computational Intelligence", Springer-Verlag Berlin Heidelberg, vol. 4, ISBN 978-3-642-12869-1, Ed. N. Shinohara, pp. 107-131, 2017, in press.

Published Conference Papers

[C1]   M. Salucci, D. Sartori, N. Anselmi, A. Randazzo, G. Oliveri, and A. Massa, "Imaging buried objects within the second-order Born approximation through a multiresolution-regularized inexact-Newton method," 2013 International Symposium on Electromagnetic Theory (EMTS 2013) , Hiroshima, Japan, pp. 116-118, May 20-24, 2013 (Invited).

[C2]   M. Carlin, N. Anselmi, L. Manica, P. Rocca, and A. Massa, "Exploiting interval arithmetic for predicting real arrays performances - The linear case," Proc. 2013 IEEE AP-S International Symposium, Lake Buena Vista, Florida, USA, pp. 298-299, July 7-12, 2013.

[C3]   L. Manica, P. Rocca, N. Anselmi, and A. Massa, "On the synthesis of reliable linear arrays through interval arithmetic," Proc. 2013 IEEE AP-S International Symposium, Lake Buena Vista, Florida, USA, pp. 296-297, July 7-12, 2013.

[C4]   N. Anselmi, L. Manica, P. Rocca and A. Massa, "Synthesis of robust linear antenna arrays exploiting an interval-based particle swarm optimizer," 8th European Conference on Antennas and Propagation (EUCAP 2014), The Hague, The Netherlands, pp. 2255-2258, April 6-11, 2014 (Invited).

[C5]   N. Anselmi, L. Manica, P. Rocca, and A. Massa, "Tolerance analysis of reconfigurable monopulse linear antenna arrays using interval arithmetic," 8th European Conference on Antennas and Propagation (EUCAP 2014), The Hague, The Netherlands, pp. 1509-1512, April 6-11, 2014.

[C6]   N. Anselmi, G. Oliveri, and A. Massa, "A total variation compressive sensing technique for imaging large scatterers", 8th European Conference on Antennas and Propagation (EUCAP 2014), The Hague, The Netherlands, pp. 1330-1333, April 6-11, 2014.

[C7]   P. Rocca, N. Anselmi, L. Poli, L. Manica, E. Giaccari, and A. Massa, "Modelling Uncertainty in Phased Arrays Through the Interval Analysis," Proc. IEEE International Symposium on Antennas and Propagation (IEEE AP-S 2014) and USNC-URSI National Radio Science Meeting, Memphis, Tennessee, USA, July 6-11, 2014.

[C8]   P. Rocca, N. Anselmi, L. Poli, L. Manica, E. Giaccari, and A. Massa, "Modeling uncertainty in phased arrays thorugh the interval analysis," Proc. 2014 IEEE AP-S International Symposium and USNC-URSI Radio Science Meeting, Memphis, Tennessee, USA, pp. 1157-1158, July 6-12, 2014.

[C9]   N. Anselmi, P. Rocca, E. Giaccari, and A. Massa, "Synthesis of robust beamforming weights for linear antenna arrays," Proc. 2014 IEEE Antenna Conference on Antenna Measurements and Applications (IEEE CAMA 2014), Antibes Juan-les-Pins, France, pp. 1-3, November 16-19, 2014.

[C10]   P. Rocca, N. Anselmi, T. Moriyama, D. Bresciani, and A. Massa, "Interval- based tolerance analysis with localized surface errors in parabolic reflectors," Proc. 2014 IEEE Antenna Conference on Antenna Measurements and Applications (IEEE CAMA 2014), Antibes Juan-les-Pins, France, pp. 1-3, November 16-19, 2014.

[C11]   P. Rocca, T. Moriyama, N. Anselmi, and A. Massa, "Robust prediction of the radiated pattern features with uncertainties in reflectarray design," Proc. 2014 IEEE Antenna Conference on Antenna Measurements and Applications (IEEE CAMA 2014), Antibes Juan-les-Pins, France, pp. 1-3, November 16-19, 2014.

[C12]   T. Moriyama, N. Anselmi, G. Oliveri, and A. Massa, "Innovative CS imaging methods in transformed domains," Proc. 2014 IEEE Antenna Conference on Antenna Measurements and Applications (IEEE CAMA 2014), Antibes Juan-les-Pins, France, pp. 1- 3, November 16-19, 2014.

[C13]   T. Moriyama, L. Poli, N. Anselmi, P.-P. Ding, and G. Oliveri, "A compressive sensing approach to NDE/NDT," Proc. 2014 IEEE Antenna Conference on Antenna Measurements and Applications (IEEE CAMA 2014), Antibes Juan-les-Pins, France, pp. 1-3, November 16-19, 2014.

[C14]   N. Anselmi, L. Poli, G. Oliveri, and A. Massa, "A Quantitative inverse scattering with sparseness constraints - The compressive sensing paradigm," 9th International Conference on Computational Physics (ICCP-9), Singapore, January 7-11, 2015.

[C15]   L. Poli, N. Anselmi, M. Carlin, and P. Rocca, "Compressive sensing technique for multi-frequency sparse linear array design," 9th European Conference on Antennas and Propagation (EUCAP 2015), Lisbon, Portugal, April 12-17, 2015.

[C16]   N. Anselmi, L. Poli, P. Rocca, F. Viani, and A. Massa, "Sensitivity analysis of mutual coupling effects in antenna arrays through interval analysis," Proc. 2015 IEEE AP-S International Symposium and USNC-URSI Radio Science Meeting, Vancouver, BC, Canada, pp. 426-427, July 19-25, 2015.

[C17]   N. Anselmi, L. Poli, L. Tenuti, P. Rocca, F. Viani, and A. Massa, "Tolerance analysis of planar arrays through Minkowski-based interval analysis," Proc. 2015 IEEE AP-S International Symposium and USNC-URSI Radio Science Meeting, Vancouver, BC, Canada, pp. 2501-2502, July 19-25, 2015.

[C18]   F. Viani, N. Anselmi, M. Donelli, P. Garofalo, G. Gottardi, G. Oliveri, L. Poli, A. Polo, P. Rocca, M. Salucci, L. Tenuti, and A. Massa, "On the role of information in inversion and synthesis - challenges, tools, and trends," Proc. 2015 IEEE Mediterranean Microwave Symposium (MMS-2015), Lecce, Italy, pp. 1-4, November 30 - December 2, 2015.

[C19]   N. Anselmi, L. Poli, G. Oliveri, P. Rocca and A. Massa, "Microwave Imaging of 2D Scatterers through Wavelet-Based Alphabet and Compressive Sensing," Assemble generale Interferences d'Ondes (GDR Ondes), Lyon, France, Oct. 19-21, 2015.

[C20]   G. Oliveri, P. Rocca, L. Poli, N. Anselmi, M. Salucci, T. Moriyama, T. Takenaka, A. Massa, "Real-time eddy-current-testing of metallic structures through statistical learning methodology," PIERS 2016 in Shangai, Shanghai, China, August 8-11, pp. 3957-3958, 2016 (Invited)

[C21]   A. Massa, G. Oliveri, N. Anselmi, and L. Poli, "Compressive sensing as applied to electromagnetics - Challenges, solutions, and future trends," 10th European Conference on Antennas and Propagation (EUCAP 2016), Davos, Switzerland, pp. 1-4, April 11-15, 2016 (Invited).

[C22]   N. Anselmi, P. Rocca, and A. Massa, "A Minkowski-based interval analysis tool for pattern distortions in reflector antennas with localized surface deformations," 10th European Conference on Antennas and Propagation (EUCAP 2016), Davos, Switzerland, pp. 1-4, April 11-15, 2016.

[C23] A. Massa, G. Oliveri, N. Anselmi, L. Poli, and L. Tenuti, "CS-based computational imaging at microwave frequencies," Proc. 2016 IEEE AP-S International Symposium and USNC-URSI Radio Science Meeting, Fajardo, Puerto Rico, pp. 1061-1062, June 26 - July 1, 2016 (Invited paper).

[C24] L. Poli, N. Anselmi, G. Gottardi, P. Rocca, and A. Massa, "Probabilistic interval method for phased array sensitivity analysis," Proc. 2016 IEEE AP-S International Symposium and USNC-URSI Radio Science Meeting, Fajardo, Puerto Rico, pp. 919-920, June 26 - July 1, 2016.

[C25] N. Anselmi, P. Rocca, and A. Massa, "An innovative optimization strategy for phased array tiling," Proc. 2016 IEEE AP-S International Symposium and USNC-URSI Radio Science Meeting, Fajardo, Puerto Rico, pp. 769-770, June 26 - July 1, 2016.

[C26] N. Anselmi, L. Poli, A. Randazzo, and G. Oliveri, "Alphabet CS for inverse scattering," 2016 International Symposium on Electromagnetic Theory (EMTS 2016), Espoo, Finland, pp. 141-143, August 14-18, 2016 (Invited).

[C27] N. Ebrahimi, N. Anselmi, P. Rocca, and A. Massa, "Tolerance analysis of the reflectarray antenna through Minkowski-based interval analysis," 11th European Conference on Antennas and Propagation (EUCAP 2017), Paris, France, pp. 2392-2395, March 19-24, 2017.

[C28] N. Anselmi, G. Oliveri, and A. Massa, "Synthesis of clustered arrays based on a total variation compressive sensing approach," 11th European Conference on Antennas and Propagation (EUCAP 2017), Paris, France, pp. 862-864, March 19-24, 2017.

[C29] A. Massa, N. Anselmi, G. Gottardi, G. Oliveri, L. Poli, P. Rocca, M. Salucci, and L. Tenuti, "Unconventional techniques for the synthesis of modern antenna arrays," 11th European Conference on Antennas and Propagation (EUCAP 2017), Paris, France, pp. 2843-2845, March 19-24, 2017 (Invited).

[C30] S. Ahmed, M. Salucci, R. Miorelli, N. Anselmi, G. Oliveri, P. Calmon, C. Reboud, and A. Massa, "Real time groove characterization combining partial least squares and SVR strategies: application to eddy current testing," 7th International Workshop on New Computational Methods for Inverse Problems (NCMIP 2017), Cachan, France, May 12, 2017.

[C31]   N. Anselmi and T. Moriyama, "An inversion strategy for energy saving in smart building through wireless monitoring," 7th International Workshop on New Computational Methods for Inverse Problems (NCMIP 2017), Cachan, France, May 12, 2017.

[C32]   N. Anselmi, P. Rocca, M. Salucci, G. Gottardi, and A. Massa "A mask matching tiling optimization method for clustered phased arrays," Proc. 2017 IEEE AP-S International Symposium and USNC-URSI Radio Science Meeting, San Diego, California, USA, July 9-15, 2017.

[C33]   G. Oliveri, P. Rocca, L. Poli, G. Gottardi, N. Anselmi, M. Salucci, R. Lombardi, M. Chuan, M. Mattivi, P. Vinetti, F. Morgia, and A. Massa, "Innovative array architectures for 5G communications," Proc. 2017 IEEE AP-S International Symposium and USNC-URSI Radio Science Meeting, San Diego, California, USA, July 9-15, 2017.

[C34]   N. Anselmi, P. Rocca, G. Gottardi, M. Salucci, and A. Massa, "Tiling optimization of orthogonal-polygon shaped aperture for phased array antennas," Proc. 2017 IEEE AP-S International Symposium and USNC- URSI Radio Science Meeting, San Diego, California, USA, July 9-15, 2017.

[C35]   P. Rocca, N. Anselmi, M. Salucci, G. Gottardi, L. Poli, and A. Massa "A novel analytic beam steering approach for clustered phased array architectures," Proc. 2017 IEEE AP-S International Symposium and USNC-URSI Radio Science Meeting, San Diego, California, USA, July 9-15, 2017.

[C36]   M. Salucci, S. Ahmed, N. Anselmi, G. Oliveri, P. Calmon, R. Miorelli, C. Reboud, and A. Massa "Real-time crack characterization in conductive tubes through an adaptive partial least squares approach," Proc. 2017 IEEE AP-S International Symposium and USNC-URSI Radio Science Meeting, San Diego, California, USA, July 9-15, 2017.

[C37]   G. Gottardi, L. Turrina, N. Anselmi, G. Oliveri, and P. Rocca "Sparse conformal array design for multiple patterns generation through multi-task bayesian compressive sensing," Proc. 2017 IEEE AP-S International Symposium and USNC-URSI Radio Science Meeting, San Diego, California, USA, July 9-15, 2017.

[C38]   M. A. Hannan, N. Anselmi, G. Oliveri, and P. Rocca, "Joint DoA and bandwidth estimation of unknown signals through single snapshot data and MT-BCS approach," Proc. 2017 IEEE AP-S International Symposium and USNC-URSI Radio Science Meeting, San Diego, California, USA, July9-15, 2017.

[C39]   L. T. P. Bui, N. Anselmi, G. Gottardi, L. Poli, and P. Rocca, "Wide-band phased arrays synthesis with maximum bandwidth through iterative convex optimization," Proc. 2017 IEEE AP-S International Symposium and USNC-URSI Radio Science Meeting, San Diego, California, USA, July 9-15, 2017.

[C40]   A-M. Yao, N. Anselmi, and P. Rocca, "A novel planar frequency diverse array design approach for far-field wireless power transmission," Proc. 2017 IEEE AP-S International Symposium and USNC-URSI Radio Science Meeting, San Diego, California, USA, July 9-15, 2017.

Contents

List of Tables

List of Figures

Chapter 1

Introduction

Phased array antennas are enabling technologies for high radiation performance and fast beam scanning, but they are still quite expensive solutions. It is known that almost half of the cost of a phased array is due to the transmission/reception modules (TRMs) that control the amplitude and the phase/time-delay of each radiating element to perform beam forming [1]. To minimize the costs, still yielding satisfactory radiation features, unconventional architectures such as sub-arrayed/clustered, thinned, or sparse arrays have been proposed instead of fully-populated "ideal" solutions [2]. Such sub-optimal/compromise solutions are gaining more and more attention because of the most recent market requirements of scanning and beam forming capabilities [2] in modern radars and communication systems. In such a framework, clustered phased arrays implement low-cost architectures by composing the array aperture with multiple elementary tiles of two or more radiating elements, each tile being fed by a single TRM [3], still keeping good radiation efficiencies. Besides the smaller number of TRMs with respect to fully-populated architectures, a further reduction of the costs can be yielded if the sub-arrays have simple and similar shapes suitable for a modular assembling of the radiating system as well as the production of only few types of tiles [4]. Indeed modularity is advantageous in phased array antenna manufacturing since it allows the implementation of light and low profile structures [4], an easy maintenance, and integrated cooling systems [5].

Unfortunately, despite those positive features and because of the use of sub-array TRM instead of one per array element [6], a key issue to be faced is the presence of undesired high sidelobes. As a matter of fact, when reducing the architectural complexity of the array structure by simply partitioning its aperture into rectangular sub-arrays of equal shapes and orientations, the radiated power pattern turns out to be characterized by undesired grating lobes whose number unavoidably increases widening the operational bandwidth as well as extending the scanning angle [7]-[9]. To cope with this drawback, aperiodic sub-array arrangements [10]-[32] or tiles having irregular shapes and/or irregularly located within the antenna aperture [19]-[31] have been proposed. The advantages of

aperiodic tiling arrangements against grating lobes have been firstly introduced in [15][16] for the design of aperiodic array layouts. Successively, in [17][18] irregular polyomino clustering have been investigated, while in [19] and [20] Penrose and Pinwheel tilings have been considered, respectively, showing that such aperiodic clustering configurations break the periodicity of the quantization and, consequently, reduce the level of the undesired sidelobes. Nevertheless no optimization strategies of the tiling configuration and of the sub-array weights have been proposed in these works. For this reason, the phased array partitioning problem has been widely addressed in the recent years, both for linear [21]-[28] and planar [29]-[32] geometries. Theoretical optimal strategies for the computation of the sub-array weights have been exploited, such as the analytic excitations matching (EM) technique [21][23][30] as well as hybrid methodologies combining analytic [28] or evolutionary [22] algorithms with convex programming (CP) optimizers. As regards the optimization of the clustering layout, several efficient local-search techniques have then been developed, for instance the Contiguous Partition Method (CPM) [23][29][32], the Weighted K-means Clustering Method ($WKCM$) [30], Genetic Algorithm (GA)-based approaches [24] and multi-objective strategies [25], that even if they guarantee a fast convergence, they don't allow to a-priori fix the size/shape of the clusters. Accordingly, random search based schemes [12][27], dictionary-based Compressive Sensing (CS) techniques [26] as well as GA-based methods [31], have been recently proposed for the optimization of clustering configurations with modularity constraints. Focusing on planar array developed methods, in [31] the position within the aperture and the orientation of fixed-sized polyomino-shaped tiles are optimized in order to minimize the side-lobe level (SLL) of the radiated power pattern. Anyway the exact partitioning of the aperture region is not assured because the tiles are allowed to partially cover the boundary of the region, consequently the use of additional and not expected tiles shapes is necessary in order to fill the gaps at the aperture borders, and even if the maximization of the directivity (D) is enforced in the cost function, a complete coverage of the entire aperture is not always ensured.

Although efficient clustering methods are available, it is worth pointing out that no optimal-design methodologies for array tiling (namely, the full coverage of the array aperture for a given tile shape/geometry) exist till now since array clustering (especially for large arrays) is mathematically a very complex problem [33]-[35]. On the other hand, optimal surface tiling theorems [36]-[47] and algorithms [48]-[53] have been derived in other fields of science (e.g., mathematics) for simple tile shapes such as dominoes [48]-[55], bars/planks [56][57], multiple rectangular tiles [58]-[62], as well as diamond shapes [63]-[66] and more complex figures, as instance L-shaped tiles [67], T-tetrominoes tiles [68]-[74], ribbon tiles [75]-[77] and general polyominoes [78]-[85]. Among these, useful rules can be profitably exploited for array design, as well. Indeed, in some cases they could allow one to *a-priori* state (i) whether an area (i.e., the aperture in array clus-

tering) is fully tilable with the tile shape at hand, (ii) what is the extension of the uncovered area when (i) does not hold true, and (iii) the total number of admissible tiling configurations. Moreover, mathematically-derived tiling algorithms usually permit - besides the definition of the optimal surface coverage - the iterative generation of all possible subarraying configurations as well as the analytical definition of a sub-set of reference clustering solutions.

In this thesis the optimal (low-medium size arrays) or best-optimized (large size arrays) design of irregular sub-arrayed rectangular planar phased arrays, composed by domino-like tiles (i.e. rectangular 1×2 and 2×1 modules), and radiating a pencil beam which is as close as possible to a reference one, is addressed by exploiting some available mathematical literature concerned with the optimal coverage of the aperture. First, an enumerative method (ETM) based on the optimal surface-tiling algorithms introduced in [48][53] is proposed to retrieve the optimal array coverage providing the best radiation performance in low/medium size arrays. Since the number of admissible clustering rapidly grows with the array size and the enumerative procedure is no more computationally possible for large arrangements, an innovative optimization method (OTM) based on an analytically schemata-driven version of the GA is also introduced. In such an implementation, the GA profitably benefits of the knowledge of a set of reference solutions/individuals characterized by a good genetic content, namely schemata [86][87] with high fitness-values/radiation-performance, and defined according to the tiling theorems/algorithms in [48][53]. Moreover, the synthesis of tiled phased arrays has been formulated as a multi-objective optimization problem (MOP) in order to deals with multiple beam pattern requirements, also addressing the case of arbitrarily shaped arrays (i.e. not only square/rectangular shaped apertures). Finally a mask-constrained domino-tiling synthesis method is presented, in which, starting from a set of ideal requirements on the array radiation performances defined by a power mask, aims at finding the optimal tiling configuration minimizing the distance of the tiled array power pattern with the mask, while maximizing the directivity of the radiated pattern. Accordingly three new optimization techniques, namely the $ETM - CP$, $EM - ETM/CP$, and $EM - OTM/CP$ methods, are proposed, positively compared with the ETM and OTM techniques, which unavoidably fail when dealing with a mask matching synthesis problem. With respect to the state-of-art clustering/tiling methodologies, this thesis covers the following novel contributions:

1. the domino tiling synthesis problem has been formulated, exploiting mathematical surface-tiling theorems providing conditions for the existence of the optimal array clustering (i.e., the full coverage of the antenna array aperture) as well as on the total number of different optimal sub-array configurations. Accordingly, the possibility to converge towards optimal solutions is discussed, proposing theoretically unfeasible and feasible optimization strategies for the problem at hand;

2. an enumerative, yet optimal, tiling method for determining the best sub-array configuration/s of low/medium size rectangular arrays guaranteeing the maximum performance for a given array aperture and tile shape;

3. a customized GA-based optimization tool for an effective exploration of the wide solution space of clustered configurations of large rectangular arrays thanks to a suitable exploitation of analytically-defined schemata blocks;

4. a novel synthesis method addressing the mask-constrained synthesis problem by jointly combining enumerative/GA-based approaches with optimal convex strategies, for the optimization of the tiling configuration and of the tiles excitations coefficients.

Thesis outline

The thesis is organized as follows. Firstly, the phased array tiling problem is mathematically formulated in Chapter 2. Then, the analytical/GA-based tiling methodologies for low/medium and large array sizes are described in Chapter 3. The mask-constrained tiling synthesis method is reported in Chapter 4, while the multi-objective optimization problem of orthogonal polygon shaped arrays, has been addressed in Chapter 5. Finally the conclusions are drawn in Chapter 6.

Chapter 2

Phased Array Tiling Problem

In this Chapter the mathematical formulation for the analysis of clustered planar phased arrays is reported. More in detail the formulation of the array factor when considering a sub-arrayed architecture is described, focusing on rectangular shaped aperture and domino-like sub-arrays. Moreover the phased array tiling synthesis problem is formulated, providing theoretical optimum and sub-optimum optimization strategies for the computation of the clustering configuration and of the amplitude and phase sub-array coefficients, in order to radiate a pencil beam which is as close as possible to a reference one.

2.1 Mathematical Formulation

Let us consider a planar phased array of radiating elements disposed on a rectangular lattice with inter-element spacing d_x and d_y along the two surface axes [Fig. 2.1(a)]. The electromagnetic (EM) field generated in far-field by such an arrangement is expressed as $\underline{E}(\theta, \phi) = \underline{\hat{f}}(\theta, \phi) AF(\theta, \phi)$ where $\underline{\hat{f}}(\theta, \phi)$ is the *embedded* or *active* element pattern [3][6], here assumed identical for all antennas [1], and $AF(\theta, \phi)$ the array factor equal to

$$AF(\theta, \phi) = \sum_{m=1}^{M} \sum_{n=1}^{N} I_{mn} e^{jk(x_m \sin\theta\cos\phi + y_n \sin\theta\sin\phi)} \tag{2.1}$$

being I_{mn} the complex (i.e., amplitude and phase) excitation of the (m, n)-th element ($m = 1, ..., M; n = 1, ..., N$), $k = \frac{2\pi}{\lambda}$ the wavenumber, with λ the working wavelength, (x_m, y_n) the centroid of the (m, n)-th array element, and (θ, ϕ) the polar variables, with the polar axis assumed perpendicular to the array plane. Moreover, let the control points of the beam-forming network (BFN), namely the amplifiers and the phase shifters or time-delay units, all located at the sub-array level [Fig. 2.1(b)]. Then, the array weights turn out to be a function of the sub-array coefficients as follows

$$I_{mn} = I_{c_{mn}} = \alpha_{c_{mn}} e^{j\beta_{c_{mn}}}$$
$$m = 1, ..., M; \; n = 1, ..., N; \; c_{mn} \in [1, Q] \tag{2.2}$$

where c_{mn} are the elements of an $M \times N$ matrix $\mathbf{C}$ (whose elements are ordered down-up instead of an usual up-down ordering), assuming Q integer values, Q ($Q \leq M \times N$) being the number of sub-arrays/tiles composing the array and covering totally or partially its surface, while $\alpha_{c_{mn}}$ and $\beta_{c_{mn}}$ are the c_{mn}-th ($c_{mn} \in [1, Q]$) sub-array amplitude and phase coefficients, respectively [Fig. 2.2(a)]. The vector of integer indexes $\mathbf{c} = \{\mathcal{C}_p = c_{mn}; \; p = 1, ..., M \times N, \; p = (m, n), \; m = 1, ..., M, \; n = 1, ..., N\}$, namely the sub-array aggregation, univocally describes a generic array tiling configuration that is the grouping of the $M \times N$ array elements into Q sub-arrays, $\boldsymbol{\sigma} = \{\sigma_{c_{mn}}; \; c_{mn} = 1, ..., Q\}$ [Fig. 2.2(b)], and it is built from the matrix $\mathbf{C}$ considering a raster order, starting from the lower-left array element, $(m, n) = (1, 1)$, to the lower right element $(m, n) = (M, 1)$, and from the lower row of elements, $(m, n) = (m, 1)$, to the upper row, $(m, n) = (m, N)$.

---

[1] This assumption will not affect the optimization methodologies proposed in the following chapters, in which isotropic radiators are considered. Only the reliability assessment reported in Sec. 3.4.1.2 considers, for the sake of simplicity, the embedded element pattern of a real radiator surrounded by two rings of elements as an acceptable approximation for all the array antennas (i.e. when the size of the array is reasonably large).
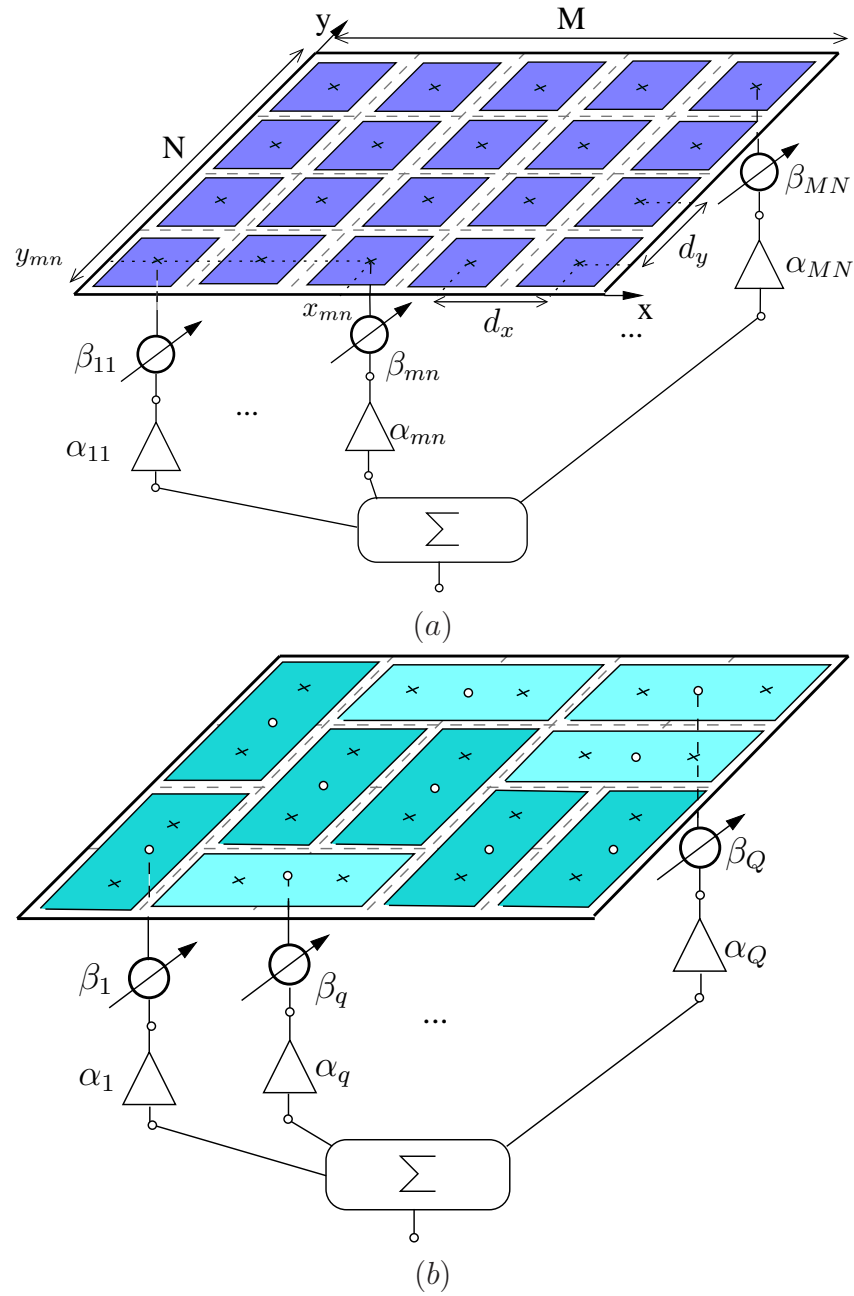
Figure 2.1: Sketch of the fully-populated array architecture *(a)* and of the sub-array architecture *(b)*.

7

2.2 Problem Statement

By supposing the use of two domino-like sub-arrays of two-elements[2] [i.e., $\sigma_{c_{mn}} = \sigma^V$ or $\sigma_{c_{mn}} = \sigma^H$ being $\sigma^V = \left\{ (x_m, y_n) \cup \left(x_m, y_{(n\pm1)}\right) \right\}$ and $\sigma^H = \{(x_m, y_n) \cup \left(x_{(m\pm1)}, y_n\right)\}$- Fig. 2.2(a)], the unknown clustered configuration, $\mathbf{c}$, and the corresponding values of the sub-array amplitudes, $\boldsymbol{\alpha} = \{\alpha_{c_{mn}}; c_{mn} = 1, ..., Q\}$, and phases, $\boldsymbol{\beta} = \{\beta_{c_{mn}}; c_{mn} = 1, ..., Q\}$, are determined by solving the following synthesis problem:

> *Phased Array Tiling Synthesis Problem* - given an array of $M \times N$ isotropic elements[3], positioned over a rectangular lattice, and two domino-like tiles $\left(\sigma^V, \sigma^H\right)$, find the optimal tiling/clustering configuration $\mathbf{c}^{opt}$ and the corresponding sub-array weights $\boldsymbol{\alpha}^{opt}$ and $\boldsymbol{\beta}^{opt}$, such that the radiated pattern fits user-defined requirements $\Phi\left(\mathbf{c}; \boldsymbol{\alpha}, \boldsymbol{\beta}\right)$, with the man lobe steered toward (θ_0, ϕ_0).

The global optimum of the array tiling synthesis problem can be theoretically reached by means of a full-global optimization approach, by jointly optimize the tiling configuration $\mathbf{c}$ and the tiles excitations coefficients $\boldsymbol{\alpha}$ and $\boldsymbol{\beta}$ as

$$\left(\mathbf{c}^{opt}; \boldsymbol{\alpha}^{opt}, \boldsymbol{\beta}^{opt}\right) = \arg\left[\min_{\mathbf{c}; \boldsymbol{\alpha}, \boldsymbol{\beta}} \left\{\Phi\left(\mathbf{c}; \boldsymbol{\alpha}, \boldsymbol{\beta}\right)\right\}\right] \quad (2.3)$$

It is clear that (2.3) turns out to be computationally unfeasible in most of the cases: it is necessary to set $2Q$ real values, for the amplitude and phase coefficients, and $M \times N$ integer numbers for the coding of the clustering configuration, which generate an extremely wide solution space even for very small arrays. This issues can be solved if the subset $\mathcal{T} = \{\mathbf{c}_t, t = 1, ..., T\}$, including all the existing tilings of the $M \times N$ array, is known, by solving the following nested optimization

$$\left(\mathbf{c}^{opt}; \boldsymbol{\alpha}^{opt}, \boldsymbol{\beta}^{opt}\right) = \arg\left[\min_{\mathbf{c}_t} \left\{\Phi\left(\mathbf{c}_t; \boldsymbol{\alpha}_t^{opt}, \boldsymbol{\beta}_t^{opt}\right)\right\}\right] \quad (2.4)$$

$$\left(\boldsymbol{\alpha}_t^{opt}, \boldsymbol{\beta}_t^{opt}\right) = \arg\left[\min_{\boldsymbol{\alpha}_t, \boldsymbol{\beta}_t} \left\{\Phi\left(\boldsymbol{\alpha}_t, \boldsymbol{\beta}_t \left| \mathbf{c}_t\right.\right)\right\}\right] \quad (2.5)$$

In order to solve such a synthesis problem, the locations and the orientations of the elementary domino shapes must be properly optimized to yield the maximum

---

[2]Each element can be either a radiating element or an aggregation (building block) of radiating elements. Without loss of generality and hereinafter, we will consider the domino-like sub-array as composed by two elementary radiating elements.

[3]The hypothesis of isotropic elements instead of real radiators as formulated in Sec. 2.1, is made for the sake of simplicity. The influence of the element factor will be analyzed in Sec. 3.4.1 and Sec. 4.4.4, for a sub-set of the optimized solutions reported in the respective sections.
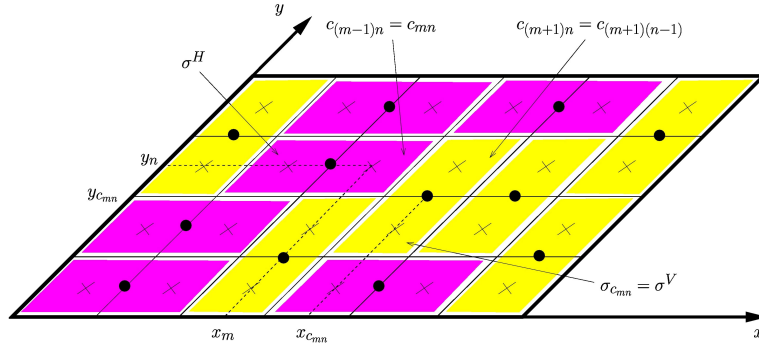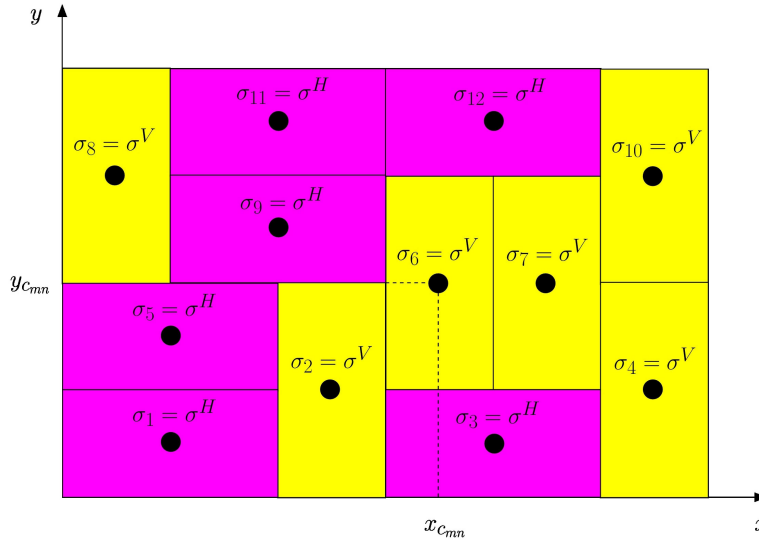
Figure 2.2: Sketch of the array aperture tiling (a)(b) when $\mathbf{c} = \{1, 1, 2, 3, 3, 4, 5, 5, 2, 6, 7, 4, 8, 9, 9, 6, 7, 10, 8, 11, 11, 12, 12, 10\}$ and $\boldsymbol{\sigma} = \{\sigma^H, \sigma^V, \sigma^H, \sigma^V, \sigma^H, \sigma^V, \sigma^V, \sigma^V, \sigma^H, \sigma^V, \sigma^H, \sigma^H\}$, being $M = 6$, $N = 4$, and $Q = 12$.

(total) coverage of the array aperture with an irregular sub-array arrangement for minimizing the level of the undesired "quantization lobes" [6]. Inspired by optimal tiling theorems and algorithms available in the scientific literature, two novel design methods will be presented in the following chapters to deal with small and large size arrays, respectively.

Chapter 3

Array Tiling Methodologies

In this Chapter two methodologies for the optimization of rectangular regions tiled by domino-like tiles are presented. By exploiting optimal analytic tiling algorithms, an enumerative-based approach able to sequentially generate all the existing complete tilings, is proposed for the optimization of domino-tiled phased arrays. When the dimension of the tiling solutions space is too large for an exhaustive search, an optimization-based methodology exploiting a customized GA optimizer is used for the synthesis of large tiled phased arrays. The numerical assessment validates the proposed approaches, considering small and medium/large apertures, also compared to state-of-art clustered solutions. Finally, the reliability assessment of the optimized solutions when considering real radiating elements, using a commercial full-wave simulator, is presented and discussed.

3.1 Tiling Theory and Theorems

Given a bounded region of the plane and a set of tile shapes, can we cover completely the region with the tiles? And in how many ways? This section is devoted to answer to these questions, exploiting the mathematical literature devoted at solving such a difficult problem. Useful theorems for the tilability of finite regions, as well as closed form formulas for the computation of the number of existing tilings are reported, with a focus on rectangular regions tiled by rectangular tiles.

Let us consider a set of S tiles shapes $\boldsymbol{\sigma} = \{\sigma_s;\ s = 1, ..., S\}$, and a bounded region A defined over a given lattice. We can say that $\boldsymbol{\sigma}$ *tiles* A (equivalently, that A is *tilable* by $\boldsymbol{\sigma}$) if A can be covered with translates of tiles $\sigma \in \boldsymbol{\sigma}$ such that each lattice cell in A is covered by exactly one tile (i.e. overlapping is not admissible). We can define two main tiling problems [40]:

- PLANE TILING PROBLEM

  Given a finite set $\boldsymbol{\sigma}$ of tiles, does $\boldsymbol{\sigma}$ tile the whole (i.e. infinite) lattice?

- FINITE TILING PROBLEM

  Given a region A and a finite set $\boldsymbol{\sigma}$ of tile, does $\boldsymbol{\sigma}$ tiles A?

The only regular polygons able to tile the plane are the square, the equilateral triangle and the hexagon [40]. These three tiles defines the three regular lattices in which the majority of tiling problems are defined. If for example we try to tile the plane with a single pentagonal shaped tile, for sure we end to leave some uncovered space in between the tiles, because the plane is not tilable by pentagons. It is well known in the literature that the Plane Tiling Problem is *undecidable.* The undecidability of tiling the plane has been proved by R. Berger in 1966 [33] in case of dominoes tiles, further discussed by R. M. Robinson in 1971 [34] for different shaped tiles. Moreover the undecidability of tiling the plane with polyominoes has been also treated by Golomb in [37] reducing the Plane Tiling Problem to the Wang Tile Problem [35]. The aim of this thesis is to exploit tiling problems for the design of antenna arrays which is an instance of the Finite Tiling Problem and, like for the Plane Tiling Problem it is usually a difficult task [40]-[45]. Even the counting of the number of existing tilings for medium/large apertures is generally an almost computationally intractable/impossible task.

In order to solve a Finite Tiling Problem we need to answer to the following questions:

Q1 *Given a tile shape, σ, is the region completely tilable? If not, what is the extension of the uncovered area?*

Q2 *Given a tile shape, σ, how many* "complete" *tiling configurations* (i.e., tiling configurations fully covering the whole region) *exist?*

In the following, some theoretical insights on these two fundamental questions will be given and, exploited in the next sections for defining suitable clustering methods for dealing with the synthesis of rectangular and fully tilable apertures with domino tiles.

3.1.1 Covering Theorem: "*Is the region tilable?*"

Answers to question $Q1$ are reported in the following, exploiting tiling theorems when considering rectangular regions and rectangular tiles, focusing on the case of domino-like tiles is treated.

Let us consider a region A discretized into $M \times N$ pixels, and rectangular shaped tiles of the class $B \times 1$ and $1 \times B$. In 1969 Klarner derived a useful condition in order to solve the respective tilability condition [42] :

T1 : An $M \times N$ rectangle A can be tiled by $\boldsymbol{\sigma} = \{B \times 1, 1 \times B\}$ tiles if and only if B divides M or N.

The theorem is then generalized for the more wide class of rectangular tiles $B \times D$ and $B \times D$, leading to the following theorem [42]:

T2 : An $M \times N$ rectangle A can be tiled by $\boldsymbol{\sigma} = \{B \times D, D \times B\}$ tiles if and only if B divides M or N, D divides M or N, and if BD divides one side of A, then the other side can be expressed in the form $Bx + Dy$ with $x, y \geq 0$.

In case the rectangle A is not tilable by the considered rectangular tiles, it is interesting to know how many pixels of A are left uncovered. We will refer to the uncovered pixel as *wasted* area. In 1979 Barnes, starting from the outcomes of the seminal work on rectangles packing [44] derived analytic relationships between the size of the region and of the tiles, with the wasted area, reported in the following theorem [44][45]:

T3 : Consider an $M \times N$ rectangle A tiled with $\boldsymbol{\sigma} \{B \times 1, 1 \times B\}$ tiles, and let

$$\hat{M} \equiv M \, mod \, B \tag{3.1}$$

$$\hat{N} \equiv N \, mod \, B \tag{3.2}$$

where $0 \leq \hat{M} < M$ and $0 \leq \hat{N} < N$, and mod being the modulo operation. Then the *wasted area* W in the best possible packing (i.e. a not complete tiling of A) with the tiles $\boldsymbol{\sigma}$ is given by

$$W = \begin{cases} \hat{M}\hat{N} & if \quad \hat{M} + \hat{N} \leq B \\ (B - \hat{M})(B - \hat{N}) & if \quad \hat{M} + \hat{N} \geq B \end{cases} \tag{3.3}$$

When considering domino-like tiles (i.e. $\boldsymbol{\sigma} = \{2 \times 1, 1 \times 2\}$) the tilability condition and the wasted area estimation are simplified in the following theorem:
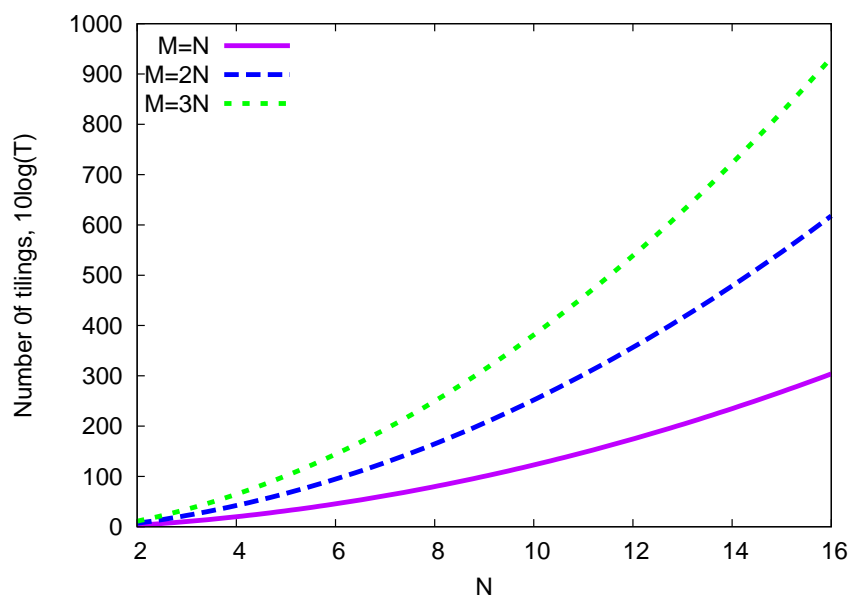
Figure 3.1: Number of complete domino tiling configurations, T, for square and rectangular $M \times N$ regions.

> **T4** : To check whether A may be fully covered with domino tiles, it is sufficient that one side of the rectangle A (either M or N) contains an even number of pixels [42]. Otherwise (i.e., only when both M and N are odd), the empty area extends to $W = 1$ square pixel [44][45].

3.1.2 Cardinality Theorem: "*How many* complete *tiling configurations?*"

In order to answers to question $Q2$, theorems and formulas taken from the mathematical literature are reported in the following. In particular the following closed form formula, will be very useful for solving the tiling problems of the following chapters, in which rectangular areas tiled by domino-like tiles are considered.

The number of tiling configurations that fully cover a surface A of dimensions $M \times N$ square pixels with domino tiles is equal to [46]

$$T = 2^{\frac{MN}{2}} \prod_{m=1}^{M} \prod_{n=1}^{N} \left[cos^2 \left(\frac{\pi m}{M+1} \right) + cos^2 \left(\frac{\pi n}{N+1} \right) \right]^{1/4} \tag{3.4}$$

To give an indication on the dimension of the solution space of the tiling problem at hand (i.e., the total number of *complete* tiling arrangements) Fig. 3.1 shows the values of T as function of the rectangle edge N for square (i.e. $M = N$) and rectangular (i.e $M = 2N$ and $M = 3N$) areas. Table 3.1 reports the exact numbers obtained using (3.4).

Table 3.1: Number of complete domino tiling configurations, T, for different sizes of square and rectangular $M \times N$ regions.

N	T		
	$N = M$	$N = 2M$	$N = 3M$
6	6.728×10^3	1.0692×10^8	1.7657×10^{12}
8	1.2989×10^7	5.4006×10^{14}	2.3334×10^{22}
10	2.5858×10^{11}	2.8942×10^{23}	3.3658×10^{35}
16	2.4449×10^{30}	6.3623×10^{61}	1.7204×10^{93}

3.2 Height Function based Encoding for Domino Tiling

In case the aperture A is totally tilable and the exhaustive analysis of the space of *complete* sub-arrays arrangements is computationally-affordable, an enumerative approach is proposed by properly customizing the analytic technique in [53] to the synthesis of sub-arrayed phased arrays. The method is based on the exploitation of the *height function* [48] that allows one to univocally identify a generic t-th tiling solution, $\mathbf{c}^{(t)}$ ($t = 1, ..., T$), namely the organization of vertical, σ^V, and horizontal, σ^H, domino tiles[1] within the array aperture A [Fig. 2.2(b)].

(A) Height Function Computation

In order to define the height function $h(\cdot)$ and its values, let us first describe the array aperture A, composed by $M \times N$ pixels, in terms of its pixel-vertices, $\{v_{mn}; \ m = 0, ..., M; \ n = 0, ..., N\}$, and pixel-edges, $\{e_{mn \to m(n\pm1)}, e_{mn \to (m\pm1)n}; \ m = 0, ..., M-1; \ n = 0, ..., N-1\}$ (Fig. 3.2). Indeed, the height function $h(\cdot)$ is defined on the pixel-vertices [i.e., $h_{mn} = h(v_{mn})$, $m = 0, ..., M; \ n = 0, ..., N$], while the h-values are determined by considering the pixel-edges. Towards this end, the aperture pixels are colored according to a black, $\zeta_{mn} = -1$, and white, $\zeta_{mn} = 1$, checkerboard pattern, starting with an arbitrary color for the first pixel $\zeta_{11} = \pm 1$ (e.g., $\zeta_{11} = 1$ in Figs. 3.2-3.3), and the edges of white/black pixels are oriented clockwise/counterclockwise (Fig. 3.2). Then, the following procedure (*Algorithm A1*) is used:

- *A1.1 Computation of the h-value of the boundary vertices of A ($\mathbf{v}_{ext}^{(t)} = \{v_{mn}^{(t)}; [m = \{0, M\}; n = 0, ..., N] \bigcup [n = \{0, N\}; m = 0, ..., M]\}$; $\mathbf{v}_{ext}^{(t)} \in \partial A$ being ∂A the contour/boundary of A) - Regardless of the t-th ($t = 1, ..., T$)*

---

[1] In case of non-circularly polarized radiators and to fit the required state-of-polarization (e.g., linear vertical/horizontal polarization) of the array, two tiles (σ^V and σ^H) equally-polarized must be built although with the same (rectangular) shape. Otherwise, only a rectangular domino tile is enough.
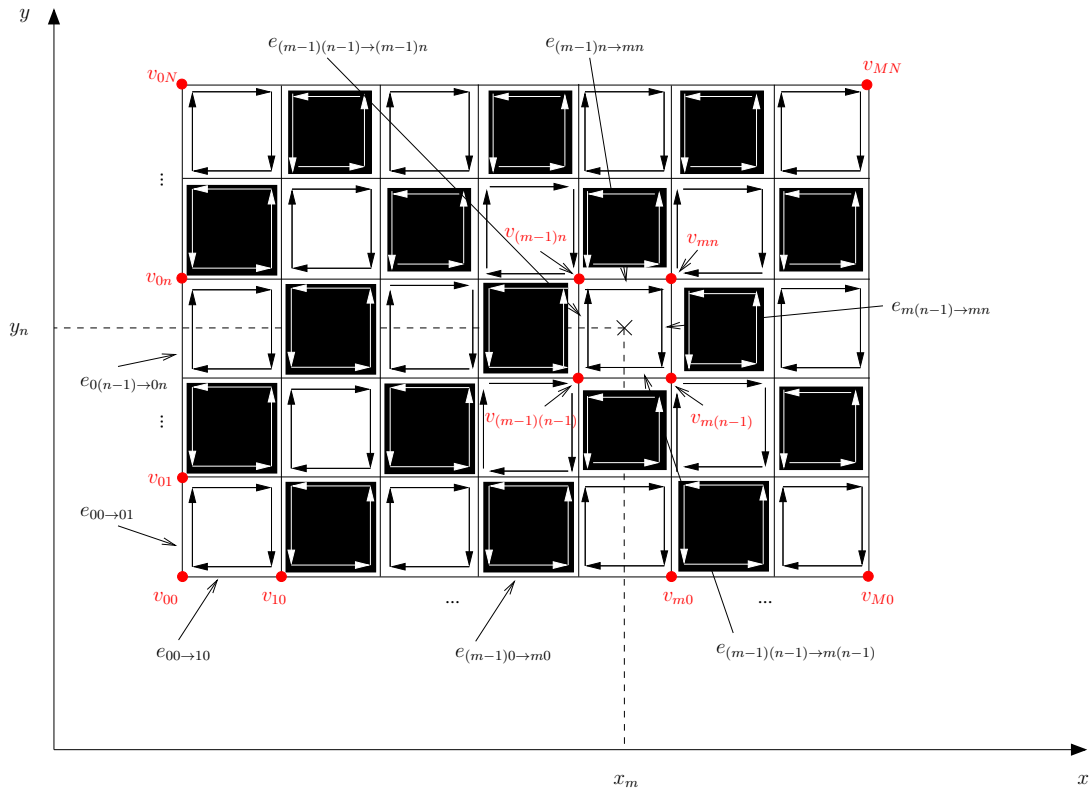
Figure 3.2: Black-and-white checkerboard representation of the array aperture A with pixel vertices v_{mn}, $m = 0, ..., M$, $n = 0, ..., N$ and edges $e_{mn \to m(n \pm 1)}$, $e_{mn \to (m \pm 1)n}$, $m = 0, ..., M-1$, $n = 0, ..., N-1$.

tiling configuration, $\mathbf{c}^{(t)}$, set the value of the height function of the vertex $v_{00} \in \mathbf{v}_{ext}^{(t)}$ to $h_{00} = h(v_{00}) = 0$ (Fig. 3.3). Then, starting from the pixel-vertex v_{00} and moving along ∂A clockwise, the value of the height function is increased/decreased of one unit from one vertex to the successive one if these latter belong to the edge of a white/black pixel

$$
\begin{aligned}
\Big\{ h_{(m-1)n} \big\rfloor_{\zeta_{mn}=\pm 1}, \; & h_{(m+1)n} \big\rfloor_{\zeta_{mn}=\pm 1}, \\
h_{m(n-1)} \big\rfloor_{\zeta_{mn}=\pm 1}, \; & h_{m(n+1)} \big\rfloor_{\zeta_{mn}=\pm 1} \Big\} = \\
& = h_{mn} \big\rfloor_{\zeta_{mn}=\pm 1} \pm 1.
\end{aligned}
\tag{3.5}
$$

It is worth pointing out that such a step is carried out only once and at the beginning of the synthesis procedure independently on the tiling ($\forall\, t \in [1, T]$) at hand;

- *A1.2 Computation of the h-value of the internal vertices of A ($\mathbf{v}_{int}^{(t)} = \{v_{mn}^{(t)}$; $m = 1, ..., M-1$; $n = 1, ..., N-1\}$)* - With reference to a clustered configuration $\mathbf{c}^{(t)}$ of tile shapes vertically or horizontally oriented (e.g., Fig. 3.4), select an internal vertex $v_{mn}^{(t)} \in \mathbf{v}_{int}^{(t)}$ with at least one neighboring vertex, denoted as $v_{pg}^{(t)} \in \overline{\mathbf{v}}_{mn}^{(t)}$ [$\overline{\mathbf{v}}_{mn}^{(t)} = \{v_{(m-1)n}^{(t)}, v_{(m+1)n}^{(t)}, v_{m(n-1)}^{(t)}, v_{m(n+1)}^{(t)}\}$ being the set of vertices neighbor to $v_{mn}^{(t)}$], having the height function value, $h_{pg}^{(t)} = h\left(v_{pg}^{(t)}\right)$ already set (i.e., $v_{pg}^{(t)} = v_{(m-1)n}^{(t)}$ or $v_{pg}^{(t)} = v_{(m+1)n}^{(t)}$ or $v_{pg}^{(t)} = v_{m(n-1)}^{(t)}$ [e.g., Fig. 3.4(b) and Fig. 3.4(d)] or $v_{pg}^{(t)} = v_{m(n+1)}^{(t)}$ [e.g., Fig. 3.4(a) and Fig. 3.4(c)]). Then, determine the unknown value $h_{mn}^{(t)}$ according to one of the following "*tiling rules*":

  - if the edge $e_{mn \to pg}$ is directed from $v_{mn}^{(t)}$ to $v_{pg}^{(t)}$ and it belongs to the contour of a tile of $\mathbf{c}^{(t)}$ [Fig. 3.4(a)] then $h_{mn}^{(t)} = h_{pg}^{(t)} - 1$;

  - if the edge $e_{mn \to pg}$ is directed from $v_{pg}^{(t)}$ to $v_{mn}^{(t)}$ and it belongs to the contour of a tile of $\mathbf{c}^{(t)}$ [Fig. 3.4(b)] then $h_{mn}^{(t)} = h_{pg}^{(t)} + 1$;

  - if the edge $e_{mn \to pg}$ is directed from $v_{pg}^{(t)}$ to $v_{mn}^{(t)}$ and it does not belong to the contour of a tile of $\mathbf{c}^{(t)}$ [Fig. 3.4(c)] then $h_{mn}^{(t)} = h_{pg}^{(t)} - 3$;

  - if the edge $e_{mn \to pg}$ is directed from $v_{mn}^{(t)}$ to $v_{pg}^{(t)}$ and it does not belong to the contour of a tile of $\mathbf{c}^{(t)}$ [Fig. 3.4(d)] then $h_{mn}^{(t)} = h_{pg}^{(t)} + 3$;

Iterate the process for all the internal vertices, $v_{mn}^{(t)} \in \mathbf{v}_{int}^{(t)}$, $m = 1, ..., M-1$; $n = 1, ..., N-1$ [Fig. 3.4(e)].

(B) Exhaustive Tiling Generation
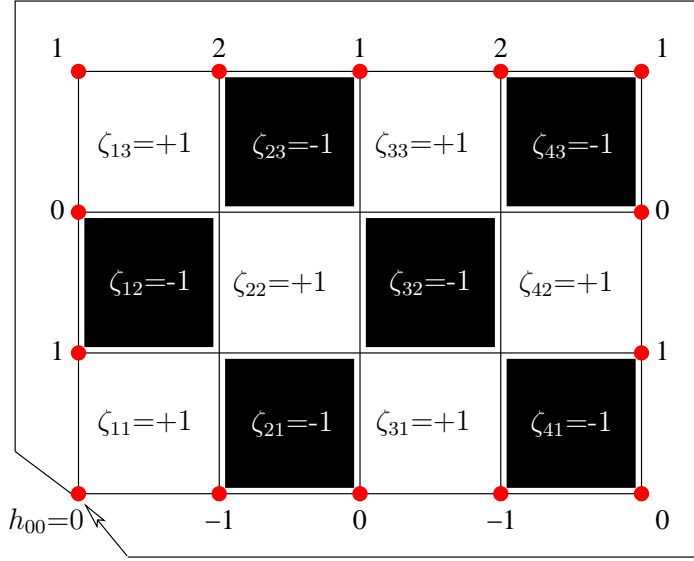
Figure 3.3: *Enumerative Tiling Method* ($M = 4$, $N = 3$) - Illustrative scheme for the computation and arising values of the height function of the boundary vertices $\mathbf{v}_{ext}^{(t)} \in \partial A$.

Starting from the definition of the height function, the analytic procedure for generating the full-set of T *complete* tilings is based on the definition of a sequence of tiling *words*, $\mathbf{w}^{(t)} = \left\{ w_l^{(t)} : l = 1, ..., L \right\}$ ($t = 1, ..., T$), each one corresponding to a sub-array configuration, $\mathbf{c}^{(t)}$, and composed by $L = (M - 1) \times (N - 1)$ integer entries (also called *letters*) whose values only[2] depend on the height function at the internal vertices, $\mathbf{v}_{int}^{(t)}$, as follows

$$w_l^{(t)} = \frac{h_{mn}^{(t)} - h_{mn}^{(1)}}{4}, \quad l = 1, ..., L \tag{3.6}$$

where $l \triangleq m + (n - 1) \times (M - 1)$, $h_{mn}^{(t)}$ and $h_{mn}^{(1)}$ being the height function value of the (m, n)-th ($m = 1, ..., M - 1$; $n = 1, ..., N - 1$) internal vertex of the t-th entry and of the first one (i.e., $\mathbf{c}^{(1)}$ also indicated as *minimal tiling* [48]) of the T-size list of *complete* configurations, respectively.

The *minimal tiling* is generated only once by means of the following algorithmic sequence (*Algorithm B1*):

- *B1.1 Vertex selection* - Select the vertex of ∂A with maximum height value

---

[2]Once again it is worth remembering that the values of the height function in correspondence with the boundary vertices, $\mathbf{v}_{ext}^{(t)} \in \partial A$, only depend on the shape of the array aperture A. Therefore, they are the same for a fixed surface A whatever the *complete* tiling configuration at hand.

(i.e., $v_{mn}^{(1)} = arg \left\{ max_{k=0,...,N}^{j=0,...,M} \left[h\left(v_{jk}^{(t)}\right); v_{jk}^{(t)} \in \mathbf{v}_{ext}^{(t)} \right] \right\}$). If there are two or more vertices with the same height function, arbitrarily select one of them;

- $B1.2$ *Domino tile placement* - Place a vertical, σ^V, or horizontal, σ^H, domino tile so that the two boundary vertices adjacent to $v_{mn}^{(1)}$ (i.e., $v_{(m\pm1)n}^{(1)} \in \mathbf{v}_{ext}^{(1)}$ [e.g., Fig. 3.5(a)] or $v_{m(n\pm1)}^{(1)} \in \mathbf{v}_{ext}^{(1)}$) are also vertices of the same domino tile;

- $B1.3$ *Aperture boundary and h-value update* - Complete the computation of the h-values of the vertices of the domino tile placed in A at the step $B1.2$, by determining the height function in correspondence of the internal vertices according to the rules defined in $A1.2$ of the "*Algorithm A1*" (Fig. 3.4). By subtracting the tile area $\sigma^{V/H}$ from the original surface of the aperture A, update the aperture boundary, $\partial A \leftarrow \partial\left(A - \sigma^{V/H}\right)$, as well as the extension of the aperture, $A \leftarrow \left(A - \sigma^{V/H}\right)$ [Fig. 3.5(b)];

- $B1.4$ *Stopping criterion* - Stop if the aperture is totally covered and the function h is computed for all (internal) vertices [Fig. 3.5(c)]. Otherwise, go to the "*B1.1 Vertex selection*" step.

It is worth noticing that the word "coding" such a *minimal tiling*, $\mathbf{c}^{(1)}$, is $\mathbf{w}^{(1)} = \mathbf{0}$ since all its *letters* are equal to zero (i.e., $w_l^{(1)} = 0, \forall l$) being $h_l^{(t)} = h_l^{(1)}$, $l = 1,...,L$ in (3.6).
The last tiling solution $\mathbf{c}^{(T)}$, called *maximal tiling* [48], is also analytically determined by still applying the *Algorithm B1*, but selecting the vertex with the minimum height function value on ∂A in "*B1.1 Vertex selection*".
As for the generation of the remaining *complete* tiling configurations ($t = 2,...,T-1$), once the h-values of the *minimal tiling* have been computed, $\{h_l^{(1)}, l = 1,...,L\}$, according to the "*Algorithm B1*", they are exhaustively generated as follows (*Algorithm B2*):

- $B2.1$ *Tiling word update* - Scan the tiling word $\mathbf{w}^{(t-1)}$ from the last letter ($l = L$) to the first one ($l = 1$) and stop when $h_{r-1}^{(t-1)} > h_r^{(t-1)}$, $r \in [2, L]$ [e.g., $r = L$ - Fig. 3.5(c)] or $r = 1$. Set the first r letters of the new tiling word $\mathbf{w}^{(t)}$ as follows

$$w_l^{(t)} = \begin{cases} w_l^{(t-1)} & l = 1,...,r-1 \\ w_l^{(t-1)} + 1 & l = r \end{cases} ; \qquad (3.7)$$

- $B2.2$ *Height function computation* - Compute the values of the height function of the first r internal vertices, $\{v_{mn}^{(t)} \in \mathbf{v}_{int}^{(t)}; n = \lfloor \frac{l-1}{M-1} \rfloor + 1; m = l - (n-1) \times (M-1); l = 1,...,r\}$, $\lfloor \cdot \rfloor$ being the floor function, corresponding to the letters $w_l^{(t)}$, $l = 1,...,r$ according to the rule

$$h_{mn}^{(t)} = 4w_l^{(t)} + h_{mn}^{(1)}; \qquad (3.8)$$
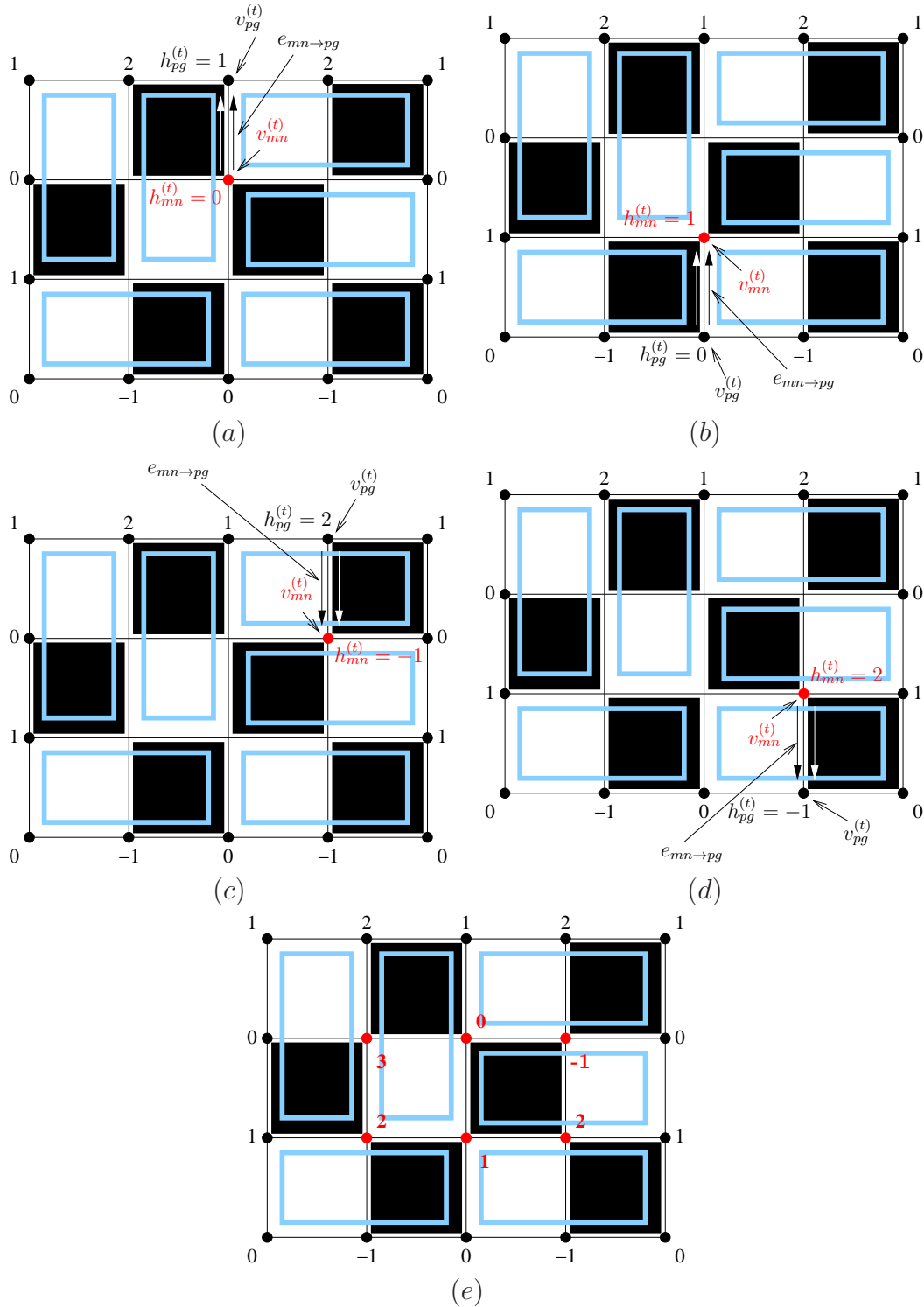
Figure 3.4: *Enumerative Tiling Method* ($M = 4$, $N = 3$) - Illustrative scheme for the computation $(a)(b)(c)(d)$ and (e) values of the height function of the internal vertices $\mathbf{v}_{int}^{(t)}$.
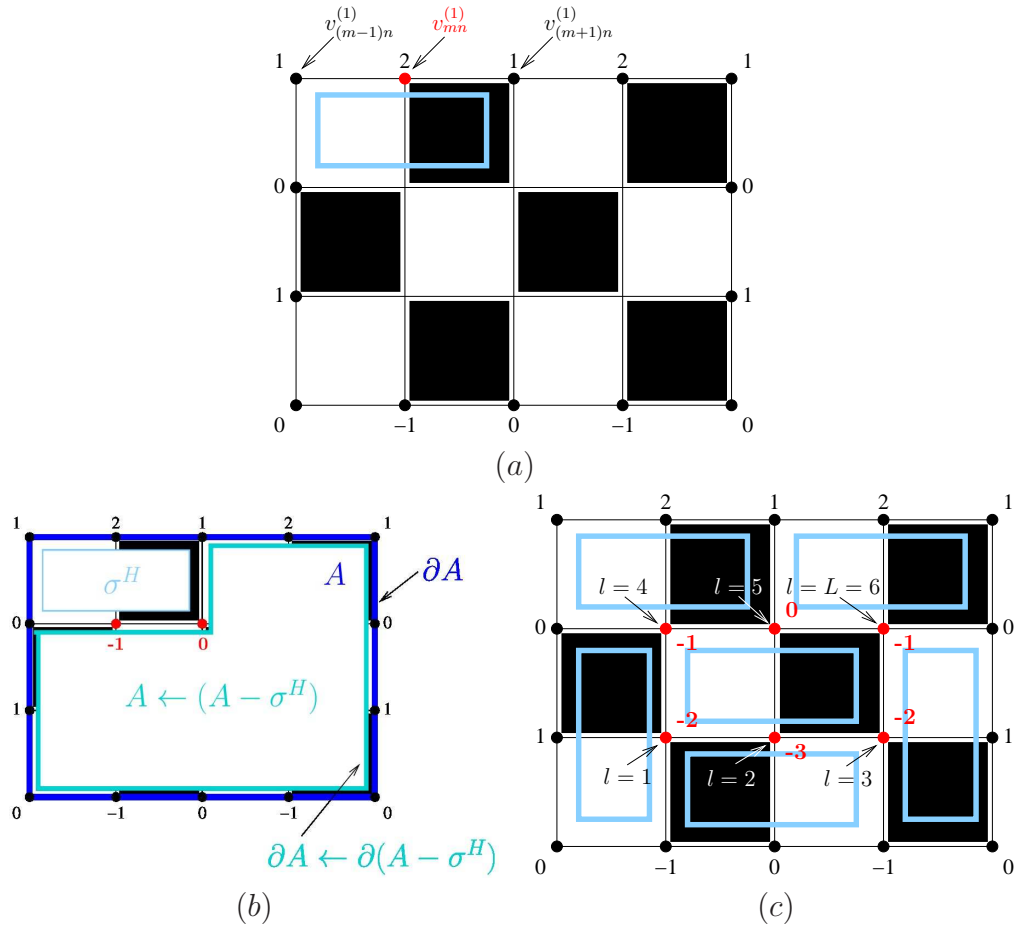
Figure 3.5: *Enumerative Tiling Method* ($M = 4$, $N = 3$) - Illustrative scheme for the definition of the *minimal tiling* configuration and for the computation of the height function values: (a) placement of a new domino tile; (b) computation of the height function of the new vertices and aperture/aperture-boundary update; (c) values of the height function of the *minimal tiling*.

- *B2.3 Feasibility Check* - Go to "*B2.4 - New tiling generation*" if the condition

$$\left| h_{mn}^{(t)} - h_{pg}^{(t)} \right| = \{1, 3\} \tag{3.9}$$

holds true, $v_{pg}^{(t)}$ being a neighboring vertex (i.e., $v_{pg}^{(t)} \in \overline{\mathbf{v}}_{mn}^{(t)}$) with an already defined height function value, $h_{pg}^{(t)} = h\left(v_{pg}^{(t)}\right)$. Otherwise, go to "*B2.1 Tiling word update*" and continue scanning the tiling word starting from $r = r - 1$;

- *B2.4 New tiling generation* - Known the values of $h(\cdot)$ on ∂A (*Algorithm A1*) and the height function values $h_{mn}^{(t)}$ computed through (3.8), place the domino tiles inside A to fit the "*tiling rules*" in "*A1.2 Computation of the h-value of the internal vertices of A*". Afterwards, define the new *complete* tiling configuration $\mathbf{c}^{(t)}$ by applying the "*Algorithm B1*". Once the array aperture A has been totally covered and the height function values are all defined, $\{h_{mn}^{(t)}; m = 1, ..., M - 1; n = 1, ..., N - 1\}$, compute the remaining letters $w_l^{(t)}$, $l = r + 1, ..., L$ through (3.6);

- *B2.5 Stopping criterion* - If $t = T - 1$, then stop the tiling generation. Otherwise, update t (i.e., $t \leftarrow t + 1$) and go to "*B2.1 Tiling word update*".

3.3 Pencil Beam Synthesis through the Enumerative Tiling Method (*ETM*)

Once the complete list of existing tilings has been generated, the nested optimization strategy described in Chapter 2 [eq. (2.4) and (2.5)] together with an excitation matching approach for a fast computation of the sub-array coefficients is here proposed in order to find the optimal tiling/clustered configuration, $\mathbf{c}^{opt}$ that totally covers the aperture and radiates the minimum sidelobe level (*SLL*) pencil beam pattern with its main beam steered along (θ_0, ϕ_0). Accordingly the cost function of the tiling array synthesis problem is defined as follows

$$\Phi\left(\mathbf{c}; \boldsymbol{\alpha}, \boldsymbol{\beta}\right) = SLL\left[\left|AF\left(\theta, \phi; \mathbf{c}, \boldsymbol{\alpha}, \boldsymbol{\beta}\right)\right|^2\right] \tag{3.10}$$

where in (3.10) $SLL\left[\cdot\right]$ is the function measuring the SLL of the power pattern $\left|AF\left(\theta, \phi; \mathbf{c}, \boldsymbol{\alpha}, \boldsymbol{\beta}\right)\right|^2$. The *Enumerative Tiling Method* (*ETM*) is summarized in the following steps:

- **Step 1.** *Reference Array*: given the ideal fully-populated array, the reference amplitude weights α_{mn}^{ref}, $m = 1, ..., M$, $n = 1, ..., N$ are obtained by means of standard methods (e.g., Taylor, Dolph-Chebyshev [91]) while the phases as

$$\beta_{c_{mn}} = -k\left(x_{c_{mn}} \sin\theta_0 \cos\phi_0 + y_{c_{mn}} \sin\theta_0 \sin\phi_0\right), \tag{3.11}$$

$x_{c_{mn}} = \left\{ \frac{x_m + x_{(m\pm1)}}{2} \right\}$ and $y_{c_{mn}} = \left\{ \frac{y_n + y_{(n\pm1)}}{2} \right\}$ being the planar coordinates of the c_{mn}-th sub-array center.

- **Step 2.** *Tilings Enumeration*: the optimal tiling generation method described in the previous section, is used for the enumeration of the whole set of clustering configurations $\mathbf{C}_\infty = \left\{ \mathbf{c}^{(t)}; t = 1, ..., T \right\}$;

- **Step 3.** *EM Sub-array Weights*: for each tiling $\mathbf{c}_t$;, $t = 1, ..., T$, the optimal compromise EM excitations coefficients $\left(\boldsymbol{\alpha}_t^{EM}, \boldsymbol{\beta}_t^{EM} \right)$ are obtained minimizing the following excitation matching problem[3]

$$\left(\boldsymbol{\alpha}_t^{EM}, \boldsymbol{\beta}_t^{EM} \right) = \arg \left[\min_{\boldsymbol{\alpha}, \boldsymbol{\beta}} \left\{ \sum_{m=1}^{M} \sum_{n=1}^{N} \left| I_{mn}^{ref} - I_{mn} \right| \right\} \right] \qquad (3.12)$$

The optimal amplitudes and phase coefficients solving (3.12), turn out to be analytically obtained as [29]

$$\alpha_{q,t}^{EM} = \frac{1}{2} \sum_{n=1}^{N} \sum_{m=1}^{M} \alpha_{mn}^{ref} \delta_{c_{mn}q}, \ q = 1, ..., Q \qquad (3.13)$$

$$\beta_{q,t}^{EM} = \frac{1}{2} \sum_{n=1}^{N} \sum_{m=1}^{M} \beta_{mn}^{ref} \delta_{c_{mn}q}, \ q = 1, ..., Q \qquad (3.14)$$

- **Step 4.** *Cost Function Evaluation*: evaluation of the SLL (3.10) for each of the T solutions and selection of the best tiling/sub-array weights, solving

$$\left(\mathbf{c}^{opt}; \boldsymbol{\alpha}^{opt}, \boldsymbol{\beta}^{opt} \right) = \arg \left[\min_{t=1,...,T} \left\{ \Phi \left(\mathbf{c}_t; \boldsymbol{\alpha}_t^{EM}, \boldsymbol{\beta}_t^{EM} \right) \right\} \right] \qquad (3.15)$$

3.3.1 Numerical Assessment

The first example is concerned with a planar array made of 40 ($M \times N = 8 \times 5$) ideal isotropic radiators (i.e. $\underline{E}(\theta, \phi) = AF(\theta, \phi)$) with inter-element spacing $d_x = d_y = d = \frac{\lambda}{2}$ [Fig. 3.6(a)]. The excitations of the reference fully-populated array [Fig. 3.6(a)], affording the power pattern shown in Fig. 3.6(b) and characterized by the pattern indexes in Tab. 3.2, have been defined as $\alpha_{mn}^{ref} \triangleq \alpha_m^{ref} \alpha_n^{ref}$, $\{ \alpha_m^{ref}; m = 1, ..., M \}$ and $\{ \alpha_n^{ref}; n = 1, ..., N \}$ being the weights of a Dolph-Chebyshev pattern [91] with $SLL = -20 \, dB$. It is worth noting

---

[3]A rigorous enumerative approach, minimizing (3.10), would require for each tiling solution the determination of the optimal set of excitations minimizing the SLL (e.g. by means of a convex optimization). Here a sub-optimal EM-based enumerative procedure is justified by the numerical efficiency of the analytic relationships used for the computation of the EM excitations. A detailed discussion about optimal ETM methods, jointly optimizing the sub-array configuration and the excitations coefficients, is reported in Chapter 4.

here that the chosen reference pattern is not an optimal reference, and has been
selected because is a simple "canonical" pattern, and if the proposed approach is
able to achieve a good approximation of the reference, the same would happen
for a true optimal pattern.

Since at least one side ($M = 8$) is even (i.e., $M \, mod \, 2 = 0$) and according to the
Covering Theorem (Sec. 3.1.2), the array aperture at hand turns out to be fully
tilable with domino tiles and the whole number of complete tiling configurations
(3.4) amounts to $T = 1.4824 \times 10^4$. Being $\Delta\tau \simeq 0.12$ [sec] ($\tau \simeq 0.178 \times 10^4$ [sec])
and $\Delta\tau_\Phi = 0.45$ [sec], the *CPU*-time for determining a clustering solution and for
computing the corresponding SLL value, respectively, the overall computational
cost of an exhaustive search is still viable ($\tau_{ETM} \simeq 0.845 \times 10^4$ [sec], being
$\tau_{ETM} \triangleq (\Delta\tau + \Delta\tau_\Phi) \times T$), thus the *ETM* (Sect. 3.3) has been profitably used
to find the globally-optimum sub-arraying configuration.

Figure 3.7 shows the SLL values of the whole set of complete tiling configu-
rations, $\mathbf{C}_\infty = \left\{ \mathbf{c}^{(t)}; t = 1, ..., T \right\}$, ordered from the worst (i.e., the clustered
arrangement with the highest SLL: $SLL^{worst} = -11.36 \, dB$) up to the best (i.e.,
$SLL^{best} = -18.89 \, dB$). While different solutions can have the same SLL value,
only a subset of the T sub-array configurations guarantees performance close to
that of the reference fully-populated array ($SLL_{th} = -20 \, dB$). More in detail,
only about 10% complete tiling solutions are characterized by $SLL < -18.0 \, dB$.
Such a percentage reduces to 1% for having $SLL < -18.5 \, dB$ and it turns out
to be less than 0.2% to guarantee a $SLL < -18.8 \, dB$.

Let us now focus on the solutions with the lowest sidelobes. There are four
different tiling configurations affording power patterns with the minimum SLL
value (i.e., $SLL^{best} = -18.89 \, dB$). They are shown in Fig. 3.8 along with
their sub-array amplitudes [Fig. 3.8(a), Fig. 3.8(c), Fig. 3.8(e), and Fig.
3.8(g)] and the radiated power patterns [Fig. 3.8(b), Fig. 3.8(d), Fig. 3.8(f),
and Fig. 3.8(h)]. For completeness, the corresponding tiling words $\mathbf{w}^{(t)}$, $t =$
$\{186, 1267, 3223, 9323\}$, are reported in Tab. 3.3. As it can be observed, these
architectures are irregularly organized with an unbalanced distributions of hori-
zontal, σ^H, and vertical, σ^V, tiles (i.e., 16 σ^H over 20). Moreover, it is worthwhile
noticing that, even though each arrangement corresponds to a different tiling-
word (Tab.3.3), all can be yielded from one of them by simple mirroring with
respect to a coordinate axis. For instance, the solutions $t = \{1267, 3223, 9323\}$
can be generated from the $t = 186$-th one [Fig.3.8(a)] by just applying an hor-
izontal [e.g., Fig. 3.8(g)] and/or a vertical [e.g., Fig. 3.8(c) and Fig. 3.8(e)]
flip/s. Such an observation will be further assessed in future works and (if veri-
fied) also fully exploited to further reduce the dimension of the solution space as
well as the *CPU*-time τ for generating $\mathbf{W}_\infty$, thus extending/enabling the use of
the *ETM* to larger array sizes to find without uncertainty the global optimum
clustering.

For comparative purposes, the worst-case solution ($t = 11729$) with the corre-
sponding sub-array excitations [Fig. 3.9(a)] and its power pattern [Fig. 3.9(b)]

(a) (b)
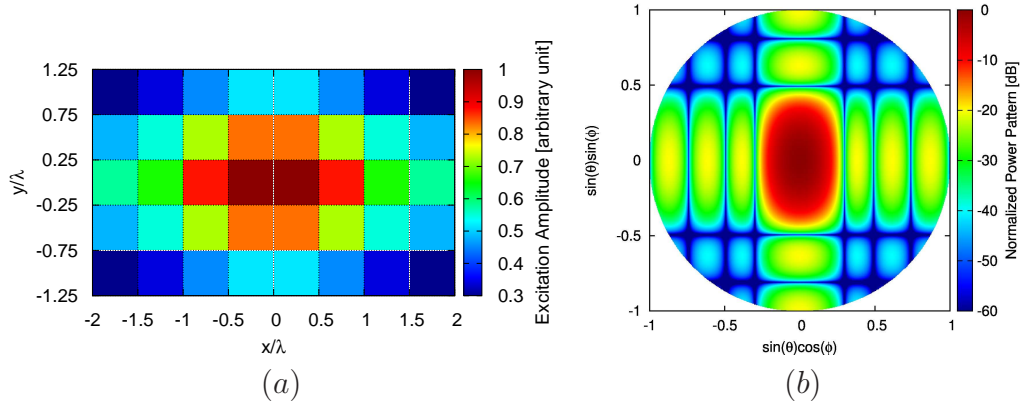
Figure 3.6: *ETM Numerical Assessment* ($M = 8$, $N = 5$; $d = 0.5\lambda$; $T = 1.4824 \times 10^4$) - Plots of (a) the array geometry and reference excitation amplitudes (α_{mn}^{ref}; $m = 1, ..., M$; $n = 1, ..., N$) and (b) the reference power pattern, $\left|\text{AF}^{ref}(\theta, \phi)\right|^2$.

Table 3.2: *ETM Numerical Assessment* ($M = 8$, $N = 5$; $d = 0.5\lambda$; $T = 1.4824 \times 10^4$) - Radiation performance (SLL, D, $HPBW_{az}$, $HPBW_{el}$) of the reference, the best, and the worst *ETM* tiling solutions.

	SLL [dB]	D [dBi]	$HPBW_{az}$ [deg]	$HPBW_{el}$ [deg]
Reference	-20.00	20.30	14.23	23.71
Best	-18.89	20.30	14.06	23.46
Worst	-11.36	20.03	14.18	21.87

is reported, as well. Unlike the optimal tilings in Fig. 3.8, which provide the lowest SLL (Tab. 3.2), the organization of domino tiles is here quite regular [Fig. 3.9(a)], thus unavoidably generating high sidelobes [6].

3.4 Pencil Beam Synthesis using the Optimization-Based Tiling Method (OTM)

The *ETM* approach allows to find the global optimum by a complete enumeration of the existing tilings. Anyway when the dimension of the array aperture increases, the number of tiles needed to completely cover it increases, and consequently the number of combinations for the aperture tiling increases. Table 3.4 reports a set of T values for different sizes of the aperture side of a square array (i.e., $M = N$). As it can be noticed, the admissible set of complete tilings exponentially grows with the array size, namely the number of elements $M \times N$,

25

Figure 3.7: *ETM Numerical Assessment* ($M = 8$, $N = 5$; $d = 0.5\lambda$; $T = 1.4824 \times 10^4$) - Values of the SLL of the whole set of complete tiling configurations, $\mathbf{C}_\infty = \left\{ \mathbf{c}^{(t)}; t = 1, ..., T \right\}$, ordered from the worst. to the best.

Table 3.3: *ETM Numerical Assessment* ($M = 8$, $N = 5$; $d = 0.5\lambda$; $T = 1.4824 \times 10^4$) - Tiling words corresponding to the *ETM* clustered arrays $t = 186$, $t = 1267$, $t = 3223$, and $t = 9323$ providing the global minimum SLL.

	t	$\mathbf{w}^{(t)}$
Best	186	00000000000011011111100111111
Best	1267	00000001100000011111011111110
Best	3223	00000011111111101222211111111
Best	9323	10000001111111122221011111111
Worst	11729	10101011111111101111100101010
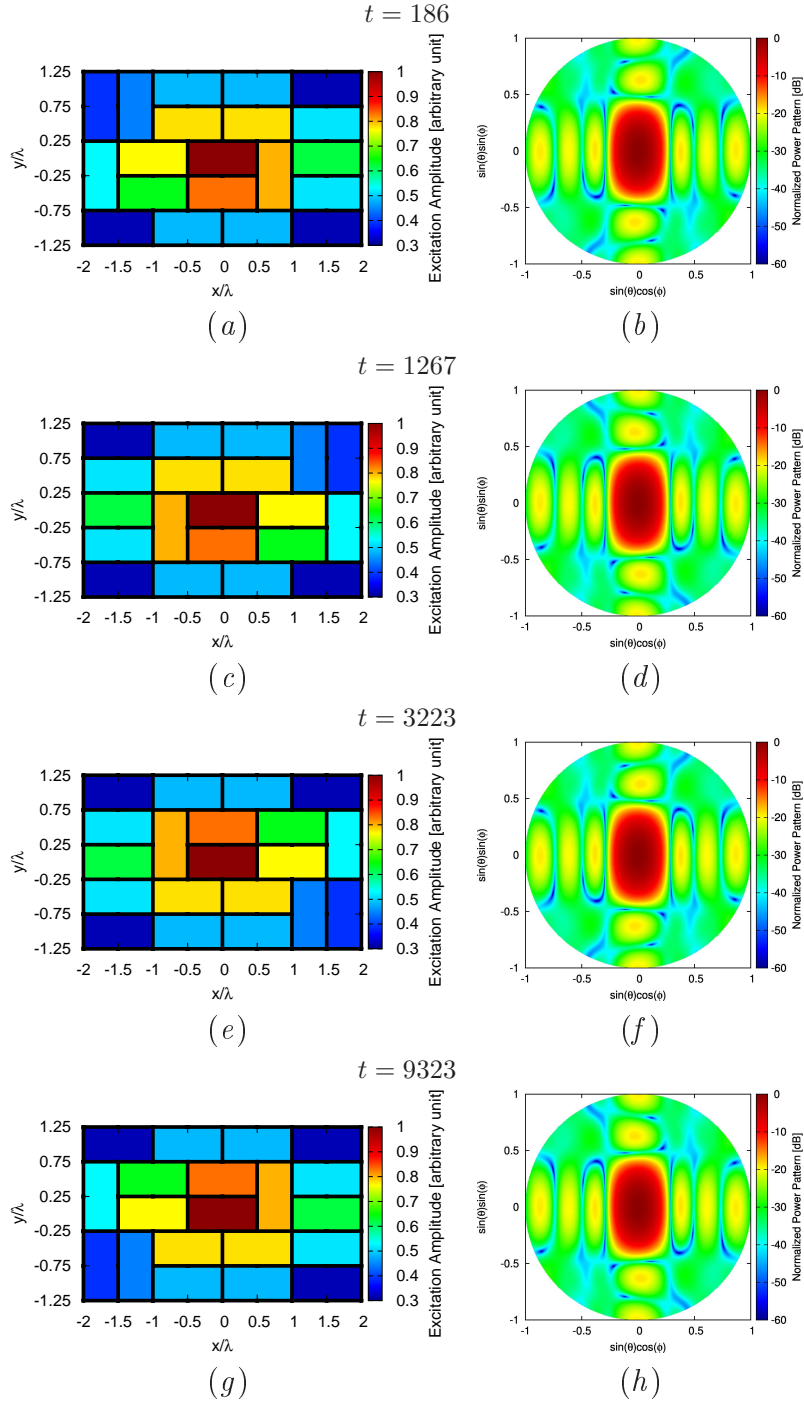
Figure 3.8: *ETM Numerical Assessment ($M = 8$, $N = 5$; $d = 0.5\lambda$; $T = 1.4824 \times 10^4$)* - Plots of $(a)(c)(e)(g)$ the tiling configurations and sub-array excitations, and $(b)(d)(f)(h)$ the power pattern of the solutions $(a)(b)$ $t = 186$, $(c)(d)$ $t = 1267$, $(e)(f)$ $t = 3223$, and $(g)(h)$ $t = 9323$ providing the global minimum *SLL*.

(a) (b)

Figure 3.9: *ETM Numerical Assessment* ($M = 8$, $N = 5$; $d = 0.5\lambda$; $T = 1.4824 \times 10^4$) - Plots of (a) the tiling configuration and the sub-array excitation amplitudes and (b) the power pattern of the worst complete clustering affording the global maximum *SLL*.

Table 3.4: Number of complete tiling configurations, T, and time requested for the generation of a single tiling solution ($\Delta\tau$) and all tiling configurations (τ) for different sizes of a square aperture, $M = N = \{6, 8, 10, 16\}$.

$M = N$	T	$\Delta\tau$ [sec]	τ [sec]
6	6728	0.10	6.72×10^2
8	1.29×10^7	0.15	1.94×10^6
10	2.58×10^{11}	0.20	5.16×10^{10}
16	2.44×10^{30}	0.40	9.76×10^{29}

pointing out that an enumerative sampling of the solution space looking for the "best" sub-array configuration turns out to be already unfeasible for $M = N = 8$ ($T = 1.29 \times 10^7$, $\Delta\tau = 0.15$ [sec] $\rightarrow \tau = 1.94 \times 10^6$ [sec]) and impossible when $M = N \geq 10$ ($T \geq 2.58 \times 10^{11}$, $\Delta\tau \geq 0.20$ [sec] $\rightarrow \tau = 5.16 \times 10^{10}$ [sec]), $\Delta\tau$ and τ being the *CPU*-time for generating one and the whole set of T complete tilings ($\tau \triangleq T \times \Delta\tau$), respectively, on a $2.4GHz$ PC with $2GB$ of RAM.

Accordingly, when the dimension of the aperture (i.e., the cardinality of the corresponding solution space) does not allow a computationally-feasible application of the enumerative approach (Sect. 3.3), the domino-like aperture tiling is solved through an innovative binary GA that exploits both a suitable coding and proper analytically-generated GA-"schemata" [87] to efficiently (i.e., maximizing the convergence rate as well as reducing the dimension of the solution space) explore the solution space for enabling the synthesis of large arrays. Before describing the optimization procedure, let us point out the following key-points concerned with the GAs and their effective/profitable use in high-dimensional

solution space (e.g., large array synthesis):

- **GA-Schemata and GA-Implicit Parallelism**
  *GA*s search mechanisms mainly rely on "schemata" and the arising "implicit parallelism" [87]. From [87], a *schemata* is a similarity template describing a subset of chromosomes (i.e., the coded representation of the unknown vector $\mathbf{w}$) with similarities at certain chromosome positions. For a binary alphabet, (i) there are 3^L admissible schemata, (ii) a *GA* population of U trial solutions, $\mathbf{W}^{(i)} = \left\{ \mathbf{w}_i^{(u)}; u = 1, ..., U \right\}$, contains between 2^L and $U \times 2^L$ schemata depending upon the population diversity, and (iii) at each i-th iteration ($i = 0, ..., I$; I being the maximum number of iterations) standard genetic operators (*i.e.*, *roulette-wheel* selection, *single-point* crossover, and mutation [94][88][89]) process something like U^3 schemata.
  The *Schemata theorem* [87] states that a schemata is replied in the successive iterations a number of times proportional to the average fitness of the corresponding trial chromosomes, $\Phi_i^{(u)} = \Phi\left(\mathbf{w}_i^{(u)}\right)$ being the fitness of $\mathbf{w}_i^{(u)}$. Therefore, the *GA* solution at the convergence (i.e., $i = I^{opt} \leq I$) is composed by the best schemata combined during the evolution by all *GA* operators, but mainly by the crossover, which is responsible of mixing the genetic content of the different chromosomes. Since a schemata is replied in the successive iterations a number of times proportional to the average fitness of the corresponding trial chromosomes [87], it turns out that "generating/selecting" from the beginning ($i = 0$ - Initialization) "good" schemata is a good receipt to increase the convergence rate (i.e., reducing the number of iterations I^{opt}) for reducing the *CPU*-time of the optimization process.
  Towards this end, let us consider that the probability to yield "good" schemata from a random generation of a population of U ($U \leq T$) tiling *words*, $\mathbf{W}^{(0)} = \left\{ \mathbf{w}_0^{(u)}; u = 1, ..., U \right\}$, $U \leq T$, is generally lower than randomly choosing/generating these latter from the total set of admissible T words, $\mathbf{W}_\infty = \left\{ \mathbf{w}^{(t)}; t = 1, ..., T \right\}$, to which the optimal one $\mathbf{w}^{opt}$ certainly belongs to, as well. On the other hand, since it is not computationally possible to generate all T words (as for the enumerative approach), a suitable algorithm for setting $\mathbf{w}_0^{(u)} \in \mathbf{W}_\infty$ without computing whole ensemble $\mathbf{W}_\infty$ is needed . As for this latter, the following "*word rules*" can be exploited:
  - *Rule #1*. By substituting (3.8) into (3.9) and re-writing the equation, it turns out that

$$4\left(w_l^{(t)} - w_k^{(t)}\right) + h_{mn}^{(1)} - h_{pg}^{(1)} = \{\pm 1, \pm 3\} \qquad (3.16)$$

where $w_k^{(t)} = \frac{h_{pg}^{(t)} - h_{mn}^{(1)}}{4}$ (3.6) is the letter corresponding to the neighboring vertex $v_{pg}^{(t)}$ and $k \triangleq p + (g - 1) \times (M - 1)$. Since $h_{mn}^{(1)} - h_{pg}^{(1)} = \{\pm 1, \pm 3\}$

from (3.9) and knowing that $w_l^{(t)}$ is an integer value, $\left(h_l^{(t)} - h_l^{(1)}\right)$ always being a multiple of 4 [52], the following condition holds true (*Rule #1*):

$$w_l^{(t)} - w_k^{(t)} = \{0, \pm 1\} \tag{3.17}$$

where $w_k^{(t)} = \left\{ w_{l-1}^{(t)}, w_{l+1}^{(t)}, w_{l-(M-1)}^{(t)}, w_{l+(M-1)}^{(t)} \right\}$ unless $w_k^{(t)} \neq w_{l+1}^{(t)}$ if $l \, mod \, (M-1) = 0$ and/or $w_k^{(t)} \neq w_{l-1}^{(t)}$ if $(l-1) \, mod \, (M-1) = 0$

- *Rule #2*. It has been proved [48] that the letters of the maximal tiling word, $\mathbf{w}^{(T)}$, with the same value belongs to connected regions over A, $\Upsilon_{int}^{(j)}$, $j = 1, ..., w^{max}$, being $w^{max} = \max_{l=1,...,L} \left\{ w_l^{(T)} \right\}$ [Fig. 3.10] and they satisfy (3.17), as well;

- *Rule #3*. From [53],

$$w_l^{(1)} \leq w_l^{(t)} \leq w_l^{(T)}, \quad l = 1, ..., L \tag{3.18}$$

$w_l^{(1)}$ and $w_l^{(T)}$ $(l = 1, ..., L)$ being the *l*-th letter of the minimal and the maximal tiling words, respectively. Therefore, since $w_l^{(1)} = 0$, $l = 1, ..., L$ and $w_l^{(T)} \leq w^{max}$ by definition of w^{max}, a generic letter $w_l^{(t)}$ is a non-negative integer value (i.e., $w_l^{(t)} \geq 0 \, \forall l \in [1, L]$);

- **GA-Coding**
  *GA*s are optimization tools devoted to minimize/maximize a suitably-defined cost function $\Phi(\cdot)$ that quantifies the fitting of a trial solution to the user-defined requirements. The computational burden of *GA*s is given by $\Delta\tau_\Psi \times I^{opt} \times U$ [92] where $\Delta\tau_\Psi$ is the *CPU*-time for a single cost-function evaluation, I^{opt} is the number of iterations to converge to the final solution, $\mathbf{c}^{opt}$, and U is the population dimension. Since U is proportional (usually greater than) to the number of problem unknowns, the use of the tiling word, $\mathbf{w} = \{w_l : l = 1, ..., L\}$, as unknown vector instead of the membership vector, $\mathbf{c} = \{c_{mn}; m = 1, ..., M; n = 1, ..., N\}$ is profitable since $L < M \times N$. Another key advantage in preferring $\mathbf{w}$ to $\mathbf{c}$ for saving computational resources lies in the cardinality of the corresponding solution space, indeed it drastically reduces from $Q^{M \times N}$ [29] to (3.4).

Within such guidelines, the following *GA*-based optimization strategy has been implemented:

- Step 1: *Population Initialization* $(i = 0)$ - Set the first $(u = 1)$ and the $\tilde{U}$-th $[\tilde{U} = \frac{w^{max} \times (w^{max} + 1)}{2} + 1^4]$ trial solutions of the initial population $\mathbf{W}^{(0)}$ to

---

[4]The value of $\tilde{U}$ is equal to the maximum number of different tiling words, all belonging to $\mathbf{W}_\infty$, that can be generated through (3.20).
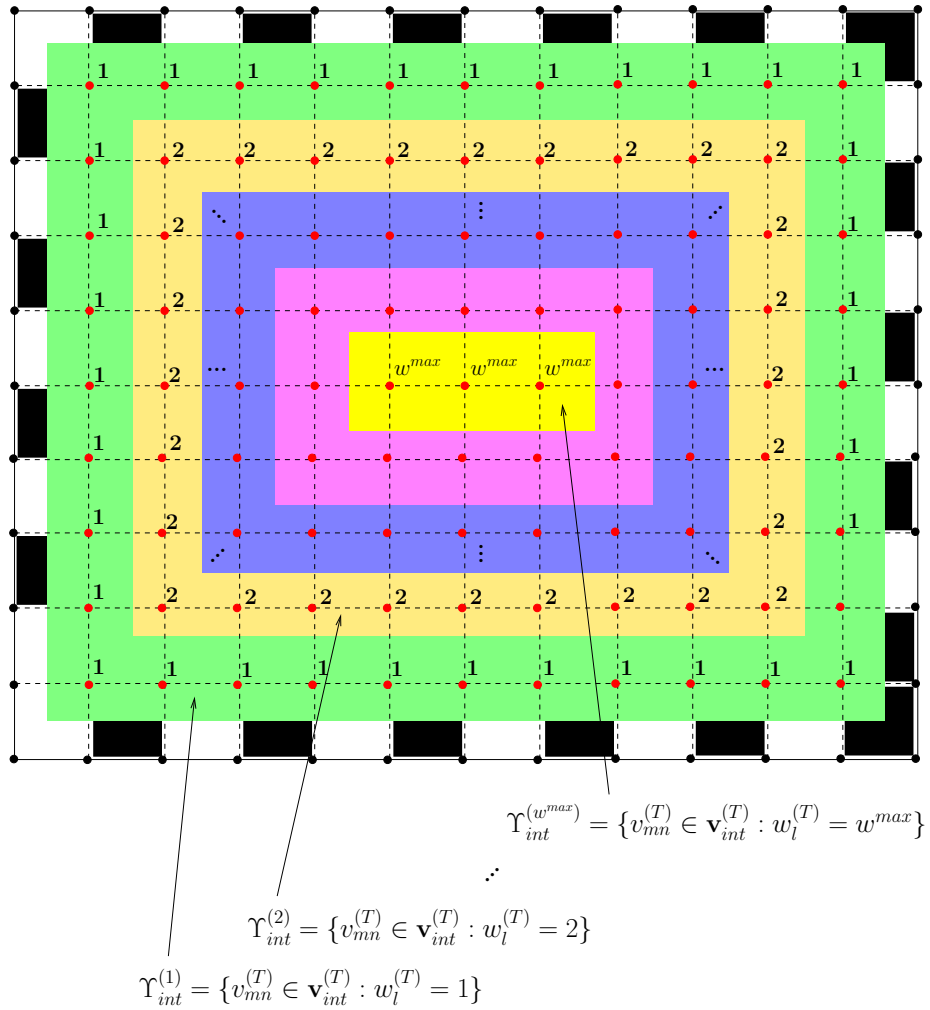
Figure 3.10: *Optimization-based Tiling Method* - Illustrative scheme for the definition of the letters of the *maximal tiling word* $\mathbf{w}^{(T)}$ on the internal vertices $\mathbf{v}_{int}^{(T)} \in A$.

the *minimal tiling* word (i.e., $\mathbf{w}_i^{(u)}\big|_{u=1,\,i=0} = \mathbf{w}^{(t)}\big|_{t=1}$) and to the *maximal tiling* word (i.e., $\mathbf{w}_i^{(u)}\big|_{u=\tilde{U},\,i=0} = \mathbf{w}^{(t)}\big|_{t=T}$), respectively.

As for the solutions from $u = 2$ to $u = \tilde{U} - 1$ still belonging to $\mathbf{W}_\infty$, consider $\mathbf{w}_0^{(1)} = \{w_{l,0}^{(1)} = 0;\, l = 1, ..., L\}$ as reference parent. Since (3.17) ("*Rule #1*") and (3.18) ("*Rule #3*") state that the l-th letter of $\mathbf{w}_i^{(u)}\big|_{u=2,\,i=0}$ can be only incremented by one (i.e., $w_{l,i}^{(u)} = w_{l,i}^{(u-1)} + 1$), set those letters whose corresponding vertices belong to the most internal region of the aperture (i.e., $v_{mn,0}^{(u)} \in \boldsymbol{\Upsilon}_{int}^{(w^{max})}$ [Fig. 3.10]) to $w_{l,i}^{(u)}\big|_{u=2,\,i=0} = w_{l,i}^{(u)}\big|_{u=1,\,i=0} + 1$. Afterwards, iteratively generate the solutions from $u = 3$ up to $\tilde{U} - 1$ by exploiting "*Rule #2*" and "*Rule #3*". More specifically, update by one the letters of the vertices in the region $\boldsymbol{\Upsilon}_{int}^{(j)}$, $j = w^{max} - u + \chi(u)$ [Fig. 3.10] being

$$\chi(u) = \begin{cases} 2 & if\ u \le w^{max} + 1 \\ 2 + \sum_{k=1}^{\xi(u)} (w^{max} - k + 1) & otherwise \end{cases} \qquad (3.19)$$

where $\xi(u) = \min\{[1, ..., w^{max} - 2] : \chi(u) \ge u\}$. Mathematically, the initialization of the u-th solution ($u = 2, ..., \tilde{U} - 1$) can be summarized as follows

$$w_{l,i}^{(u)} = \begin{cases} w_{l,i}^{(u-1)} + 1 & if\ v_{mn,i}^{(u)} \in \boldsymbol{\Upsilon}_{int}^{(j)} \\ w_{l,i}^{(u-1)} & otherwise \end{cases},\ l = 1, ..., L \qquad (3.20)$$

where

$$j = \begin{cases} w^{max} & if\ u = \chi(u) \\ j - 1 & otherwise \end{cases}. \qquad (3.21)$$

If $\tilde{U} < U$, define the remaining $(\tilde{U} - U)$ initial words by deriving at most $\left\lceil \frac{U}{\tilde{U}} \right\rceil$ ones from the application of the enumerative approach ("*Algorithm B1*") to each one of the first $\tilde{U} - 1$[5] words, $\{\mathbf{w}_0^{(u)}, u = 1, ..., \tilde{U} - 1\}$. Otherwise ($\tilde{U} > U$), randomly select the U solutions of $\mathbf{W}^{(0)}$ from the $\tilde{U}$ ones;

• Step 2: *Binary Coding* - According to (3.18) ("*Rule #3*"), the maximum number of bits for codifying a generic l-th letter of a word is equal to $B_{w_l} = \lceil \log_2 \{w^{max}\} \rceil$. Thus, code the u-th trial tiling word, $\mathbf{w}_i^{(u)}$, into a binary *GA*-chromosome of $B_\mathbf{w} = L \times \lceil \log_2 \{w^{max}\} \rceil$ bits, $\lceil \cdot \rceil$ being the ceiling function[6];

---

[5]The last word (i.e., $\mathbf{w}_0^{(\tilde{U})} = \mathbf{w}^{(T)}$) has no successive words and therefore it cannot be considered as starting point for generating new initial trial solutions.

[6]The advantage of considering $\mathbf{w}$ instead of $\mathbf{c}$ is even greater when dealing with the (binary) coded (i.e., more symbols are used in correspondence with an unknown) representation of the unknown vector since $B_\mathbf{w} \ll B_\mathbf{c}$, $B_\mathbf{c} = (M \times N) \times \lceil \log_2 Q \rceil$ being the number of bits needed for coding $\mathbf{c}$ and $w^{max} \ll Q$.

- Step 3: *Reproduction Cycle* - Apply the *roulette-wheel* selection, the *single-point* crossover with probability p_c, and the mutation with probability p_m [88][89]) (Fig. 3.11) to generate a new set of trial solutions, $\mathbf{W}^{(i)}$, $i \geq 1$. For each u-th ($u = 1, ..., U$) word, $\mathbf{w}_i^{(u)}$, compute the height function values of the corresponding vertices through (3.8) and check the condition (3.9). If this latter is not satisfied, discard this trial solution and generate a new one through the *GA* operators;

- Step 4: *Fitness Evaluation* - Determine the *GA*-population of U tiling configurations, $\{\mathbf{c}_i^{(u)}, \ u = 1, ..., U\}$, corresponding to the word set $\mathbf{W}^{(i)}$ through "*B2.4 - New tiling generation*" and compute their fitness values

$$\Phi_i^{(u)} = \Phi \left(\mathbf{c}_i^{(u)} \right) \tag{3.22}$$

  Close the *GA*-operation loop by finally applying the elitism operator [94] to keep the best solution found so far within the current i-th population;

- Step 5: *Convergence Check* - If $i = I$ or $\Phi \left(\mathbf{c}_i^{opt} \right) < SLL_{th}$,

$$\mathbf{c}_i^{opt} = \arg \left(\min_{u=1,..,U} \left\{ \Phi \left(\mathbf{c}_i^{(u)} \right) \right\} \right) \tag{3.23}$$

  and SLL_{th} being the optimal tiling at the i-th iteration and a user-defined fitness threshold, stop the iterations ($I^{opt} = i$) and set $\mathbf{c}^{opt} = \mathbf{c}_i^{opt}$. Otherwise, update the iteration index ($i \leftarrow i + 1$) and go to *Step 3*.

3.4.1 Numerical Assessment

The proposed schemata-driven synthesis framework and its implementation for the design of complete-aperture-coverage clustered planar arrays that radiate the minimum SLL power pattern are discussed in this Section by illustrating a set of representative numerical examples considering ideal-elements arrays as well as real-elements arrays, simulated using a full-wave commercial software.

3.4.1.1 Ideal-Elements Arrays

This sub-section is aimed at assessing the effectiveness of the analytically-driven *GA*-based tiling method (Sect. 3.4). Towards this end, the first benchmark is related to the same aperture of Sect. 3.3.1, therefore a tractable cardinality for the *ETM* that would not require in principle the exploitation of an optimization/solution-space-sampling strategy, but here dealt with the *OTM* for proving its capability to retrieve a global optimum solution (i.e., a clustered arrangement belonging to $\mathbf{C}_\infty$ with the lowest SLL value). The control parameters of the *GA* have been set according to [94]: $p_c = 0.9$ (crossover probability),
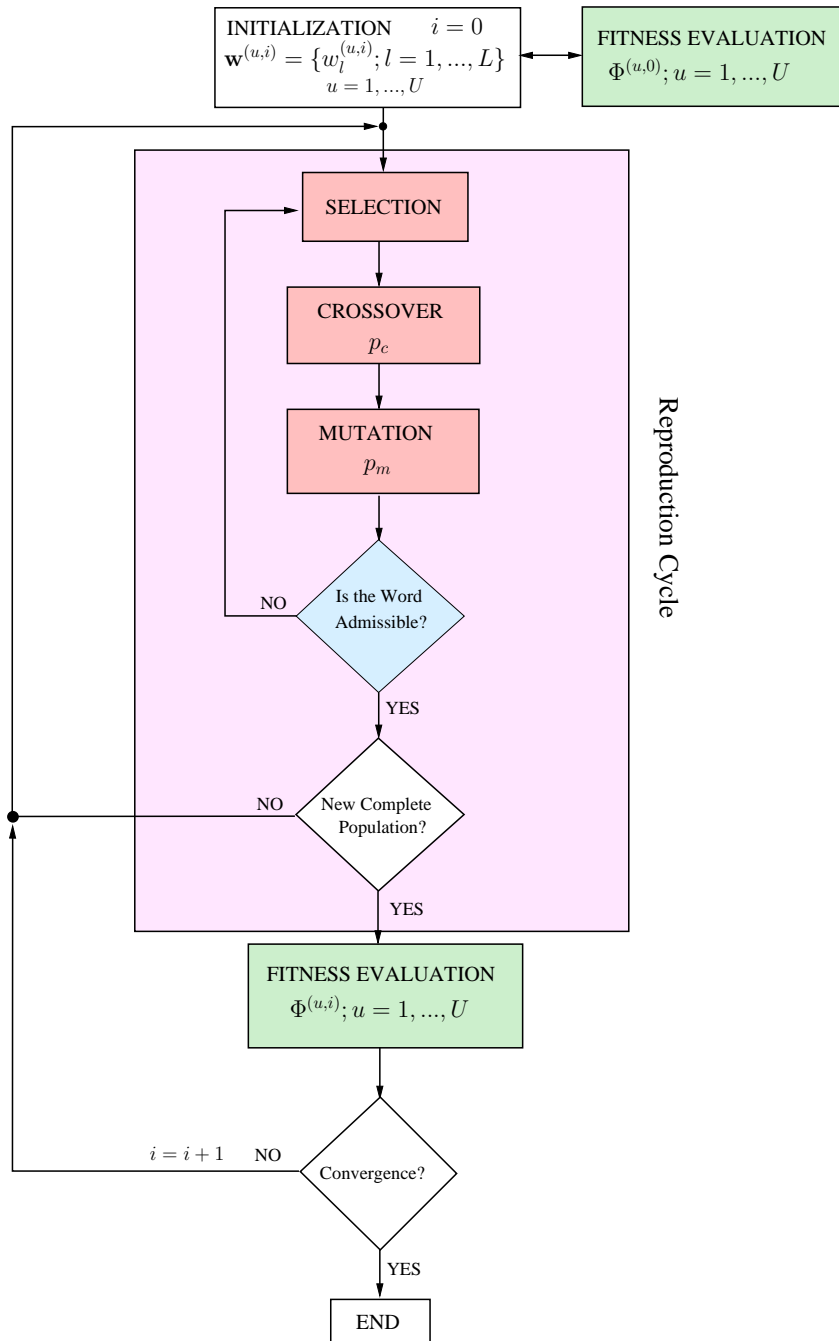
Figure 3.11: Flowchart of the *GA*-based *OTM* approach.

$p_m = 0.01$ (mutation probability), $U = 8$, and $I = 100$. Therefore, the number of trial tiling configurations potentially generated during the GA-optimization is at most $U \times I = 800$, that is about 5% of the total number of complete tiling solutions, $T = 1.4824 \times 10^4$. With reference to *Step 1* (Sect. 3.4) and the generation of the initial *tiling-words* population, $\mathbf{W}^{(0)} = \left\{ \mathbf{w}_0^{(u)}; u = 1, ..., U \right\}$ ($L = 28$ being the word length or number of *letters*), it turns out that $\tilde{U} = 4$ since $w^{max} = 2$, $\mathbf{w}^{(T)} = \{1111111122222211222211111111\}$ being the *maximal tiling word*. Table 3.5 reports the $\tilde{U} = 4$ analytically-generated words ($\mathbf{w}_0^{(1)} = \mathbf{w}^{(t)} \big]_{t=1}$ and $\mathbf{w}_0^{(\tilde{U})} = \mathbf{w}^{(t)} \big]_{t=T}$ being the *minimal* and the *maximal* tiling words, respectively), while the corresponding sub-array configurations are shown in Fig. 3.12. Due to the stochastic nature of the GA, $\Omega = 100$ runs have been executed to give statistically-meaningful insights on the OTM performance. For each ω-th ($\omega = 1, ..., \Omega$) run, the remaining $\left(U - \tilde{U} \right) = 4$ individuals for completing the initial population have been randomly generated by imposing non-equality conditions among both the whole set of U trial words and the different populations of the Ω independent runs. From such a statistical analysis, it turns out that the OTM converged to one of 4 different final solutions denoted as *Solution 1* [Figs. 3.14(a)-3.14(b)], *Solution 2* [Figs. 3.14(a)-3.14(b)], *Solution 3* [Figs. 3.14(c)-3.14(d)], and *Solution 4* [Figs. 3.14(e)-3.14(f)] whose radiation indexes are reported in Tab. 3.6. More specifically, the *Solution 1* with the lowest $SLL = -18.89 \, dB$ has been found with a success rate of 40%. Otherwise, even though the global optimum has not been reached, the GA-solution ς^{best} [$\varsigma^{best} \triangleq \arg \left(\max_{\omega=1,..,\Omega} \left\{ \Phi \left(\mathbf{c}_\omega^{opt} \right) \right\} \right)$] with the higher SLL value (*Solution 4* - Tab. 3.6) is characterized by a $SLL = \Phi \left(\varsigma^{best} \right) = -18.85 \, dB$, that is, only $0.04 \, dB$ above the global minimum of the cost function, Φ. Moreover, it is worth pointing out that always ($\forall \omega = 1, ..., \Omega$), the GA-synthesized arrangement belongs to the 0.2% pool of solutions having $SLL < -18.8 \, dB$ within the whole set of $T = 1.4824 \times 10^4$ complete tilings, thus confirming the effectiveness of the OTM in sampling the solution space.

A key item to be carefully discussed is the advantage of the smart GA-initialization of the OTM. Towards this end, let us analyze the behavior of $\Phi \left(\mathbf{c}_i^{opt} \right)$ versus the iteration index, $i = 1, ..., I$, for a representative set of the previous Ω runs along with that of a GA (denoted as *Bare Init GA*) where the U chromosomes of the initial population have been set to the first U words generated by the ETM (i.e., $\mathbf{w}_0^{(u)} = \mathbf{w}^{(t)}$, $u = t$, $t = 1, ..., U \leq T$) (Fig. 3.13). As it can be observed, whatever the initialization with good schemata, the GA-based optimizations are very efficient at the beginning ($\forall \omega$: $\Phi \left(\mathbf{c}_i^{opt} \right) \big]_{i \leq 3} \in [-16.7; -17.5] \, dB \rightarrow \Phi \left(\mathbf{c}_i^{opt} \right) \big]_{i \leq 3} \ll SLL^{worst} = -11.36 \, dB$), but the OTM-based ones quickly converge to the global minimum or close to it fitness/SLL value ($SLL^{best} = -18.89 \, dB$), while a "*bare*" initialization causes the corresponding clustering solution $\mathbf{c}_i^{opt}$ is trapped/sticks

Table 3.5: *OTM Numerical Assessment* ($M = 8$, $N = 5$; $d = 0.5\lambda$; $T = 1.4824 \times 10^4$; $L = 28$; $B = 56$; $U = 7$; $p_c = 0.9$; $p_m = 0.01$; $I = 100$) - $\tilde{U} = 4$ analytically-generated words, $\mathbf{w}_0^{(1)} = \mathbf{w}^{(t)}\rfloor_{t=1}$ and $\mathbf{w}_0^{(\tilde{U})} = \mathbf{w}^{(t)}\rfloor_{t=T}$ being the *minimal* and the *maximal* ones, respectively, of the initial OTM population.

u	$\mathbf{w}_0^{(u)}$	
1	00000000000000000000000000000000	$= \mathbf{w}^{(t)}\rfloor_{t=1}$
2	00000000111110011111100000000	
3	11111111111111111111111111111	
$\tilde{U} = 4$	11111111222221122222211111111	$= \mathbf{w}^{(t)}\rfloor_{t=T}$
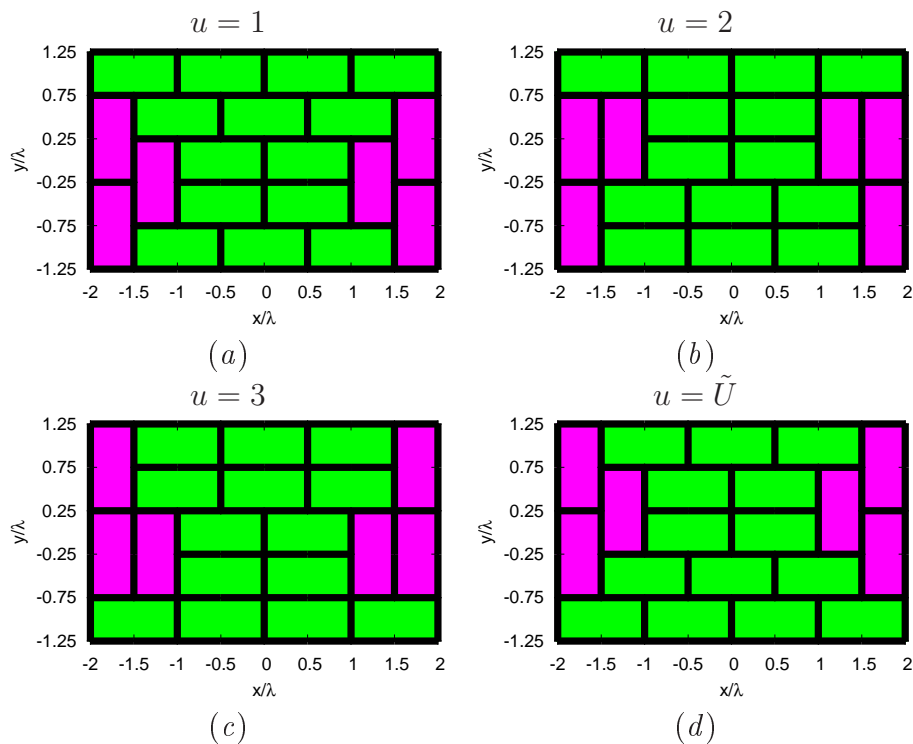
Figure 3.12: *OTM Numerical Assessment* ($M = 8$, $N = 5$; $d = 0.5\lambda$; $T = 1.4824 \times 10^4$; $L = 28$; $B = 56$; $U = 7$; $p_c = 0.9$; $p_m = 0.01$; $I = 100$) - Plots of the $\tilde{U} = 4$ tiling configurations used for the OTM initialization: (a) $u = 1$, (b) $u = 2$, (c) $u = 3$, and (d) $u = \tilde{U}$.
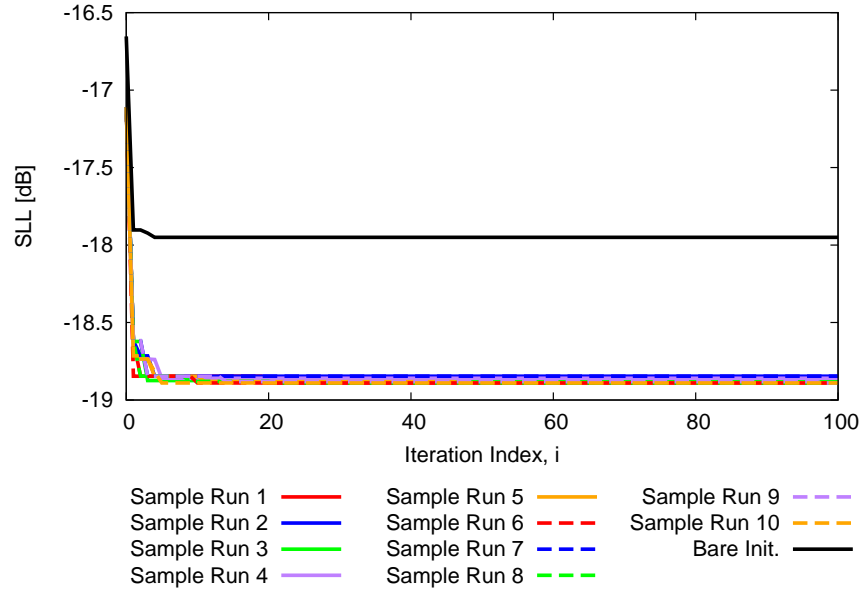
Figure 3.13: *OTM Numerical Assessment* ($M = 8$, $N = 5$; $d = 0.5\lambda$; $T = 1.4824 \times 10^4$; $L = 28$; $B = 56$; $U = 7$; $p_c = 0.9$; $p_m = 0.01$; $I = 100$) - Behavior of the optimal value of the cost function (3.22) versus the iteration index, i, for 10 representative sample runs of the *OTM* and for the *GA* run with "*bare*" initialization.

Table 3.6: *OTM Numerical Assessment* ($M = 8$, $N = 5$; $d = 0.5\lambda$; $T = 1.4824 \times 10^4$; $L = 28$; $B = 56$; $U = 7$; $p_c = 0.9$; $p_m = 0.01$; $I = 100$) - Radiation indexes (SLL, D, $HPBW_{az}$, $HPBW_{el}$) of the reference solution, of the convergence solutions synthesized in $\Omega = 100$ *OTM* runs, and when considering the *GA*-based tiling method with "*bare*" initialization.

	SLL	D	$HPBW_{az}$	$HPBW_{el}$
	[dB]	[dBi]	[deg]	[deg]
$OTM - Sol\,1$	-18.89	20.30	14.06	23.46
$OTM - Sol\,2$	-18.87	20.31	14.03	23.46
$OTM - Sol\,3$	-18.86	20.29	14.08	23.41
$OTM - Sol\,4$	-18.85	20.32	14.07	23.62
$GA - Bare$	-17.95	20.29	14.12	23.67
$Reference$	-20.00	20.30	14.23	23.71
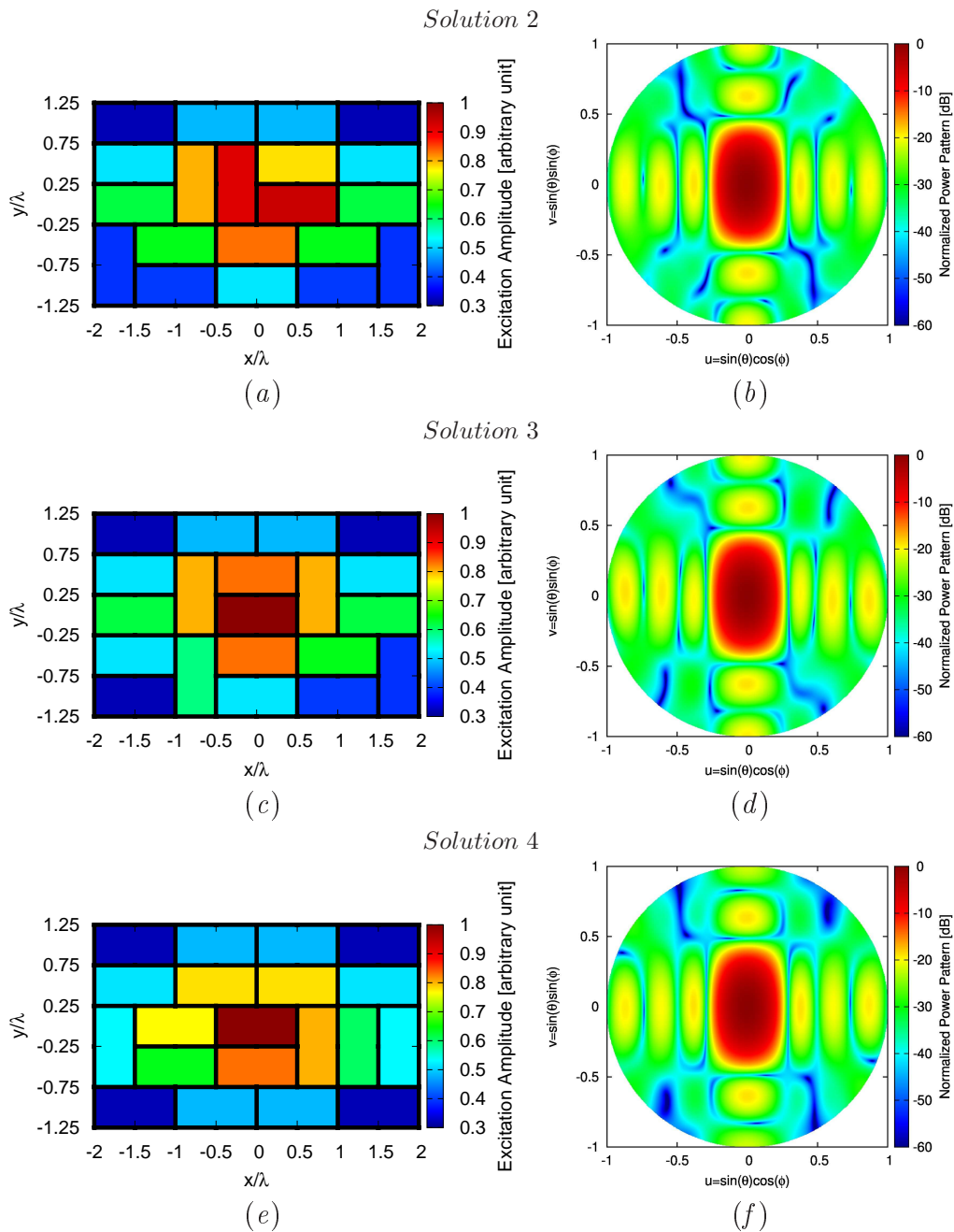
Figure 3.14: *OTM Numerical Assessment* ($M = 8$, $N = 5$; $d = 0.5\lambda$; $T = 1.4824 \times 10^4$; $L = 28$; $B = 56$; $U = 7$; $p_c = 0.9$; $p_m = 0.01$; $I = 100$) - Plots of $(a)(c)(e)$ the tiling configurations and the sub-array excitation amplitudes and $(b)(d)(f)$ the power pattern of the *Solution 2* $(a)(b)$, *Solution 3* $(c)(d)$, and *Solution 4* $(e)(f)$.

u	SLL [dB]	GA Chromosome
1	-16.67	0000000000000000000000000 0000000000000000 00000 00000000000
2	-18.07	00000000000000000101010101 00 0001 0101010100000 00000000000
3	-17.62	01010101010101010101010101010 10101 010101010101010 101 01010 101
4	-16.93	0101010101010101101010101001011 0101010101001010 101 01010 101
5	-17.11	0000000000000000000000000 0000000000000101 00000 0000000 100
6	-17.56	0000000000000000000000000 0000000000000101 00000 00000000 101
7	-17.78	000000000000000010101010 100 0001 010101010 00000 00001000 101
U=8	-17.34	0101010101010101010101010 101 0101010101100100010100 01010 100

$$(a)$$

u	SLL [dB]	GA Chromosome
1	-16.67	0000000000000000000000000000 0000000000000000 00000 00000000000
2	-17.11	0000000000000000000000000000 00000000000101 00000 00000000 100
3	-17.56	0000000000000000000000000000 00000000000101 00000 00000000 101
4	-16.14	0000000000000000000000000000 0000000101010 0 00000 00000000000
5	-17.64	0000000000000000000000000000 0000000101010 0 00000 00001000000
6	-16.80	0000000000000000000000000000 0000000 01010101 00000 00001000 100
7	-17.88	0000000000000000000000000000 0000000 01010101 00000 00001000 101
U=8	-16.11	0000000000000000000000000000 000 0001 01000000 00000 100000000000

$$(b)$$

SLL [dB]	Global-Optimum Chromosome
-18.89	0000000000000000000000000000 101 0001 01010101 00000 101 01010 101

$$(c)$$

Figure 3.15: *OTM Numerical Assessment* ($M = 8$, $N = 5$; $d = 0.5\lambda$; $T = 1.4824 \times 10^4$; $L = 28$; $B = 56$; $U = 7$; $p_c = 0.9$; $p_m = 0.01$; $I = 100$) - Chromosomal sequence of the initial *GA* population as generated in the *OTM* (*a*) and through the "bare" strategy (*b*) together with the global optimum one (*c*).

u	SLL [dB]	GA Chromosome
1	-18.71	0 0 0 0 0 0 0 0 0 0 0 0 0 0 0 0 1 0 1 0 1 0 1 0 1 0 1 0 0 0 1 0 1 0 1 0 1 0 1 0 0 0 0 0 0 0 0 0 0 0 0 0 1 0 1
2	-18.09	0 0 0 0 0 0 0 0 0 0 0 0 0 0 0 0 1 0 1 0 1 0 0 0 1 0 0 0 0 0 1 0 1 0 1 0 1 0 1 0 0 0 1 0 1 0 1 0 1 0 1 0 1 0 1
3	-18.72	0 0 0 0 0 0 0 0 0 0 0 0 0 0 1 0 1 0 1 0 1 0 1 0 1 0 0 0 0 1 0 1 0 1 0 1 0 1 0 0 0 0 0 0 0 0 0 0 0 0 1 0 1
4	-18.71	0 0 0 0 0 0 0 0 0 0 0 0 0 0 0 1 0 1 0 1 0 1 0 1 0 1 0 0 0 1 0 1 0 1 0 1 0 1 0 0 0 0 0 0 0 0 0 0 0 0 1 0 1
5	-18.85	0 0 0 0 0 0 0 0 0 0 0 0 0 0 0 0 0 0 0 0 0 0 1 0 0 0 0 0 1 0 1 0 1 0 1 0 1 0 0 0 1 0 1 0 1 0 1 0 1 0 1 0 1
6	-18.85	0 0 0 0 0 0 0 0 0 0 0 0 0 0 0 0 0 0 0 0 0 0 1 0 0 0 0 0 1 0 1 0 1 0 1 0 1 0 0 0 1 0 1 0 1 0 1 0 1 0 1 0 1
7	-18.56	0 0 0 0 0 0 0 0 0 0 0 0 0 0 1 0 1 0 1 0 1 0 1 0 0 0 0 1 0 1 0 1 0 1 0 1 0 0 0 0 0 0 0 0 0 0 0 0 1 0 1
U=8	-18.35	0 0 0 0 0 0 0 0 0 0 0 0 0 0 1 0 1 0 0 0 0 0 0 0 1 0 0 0 0 0 1 0 1 0 1 0 1 0 1 0 0 0 0 0 0 0 0 0 0 0 0 0 1 0 1

(*a*)

u	SLL [dB]	GA Chromosome
1	-18.85	0 0 0 0 0 0 0 0 0 0 0 0 0 0 0 0 0 0 0 0 0 0 0 0 1 0 0 0 0 0 1 0 1 0 1 0 1 0 1 0 0 0 1 0 1 0 1 0 1 0 1 0 1
2	-18.72	0 0 0 0 0 0 0 0 0 0 0 0 0 0 1 0 1 0 1 0 1 0 1 0 1 0 0 0 0 1 0 1 0 1 0 1 0 1 0 0 0 0 0 0 0 0 0 0 0 0 1 0 1
3	-17.83	0 0 0 0 0 0 0 0 0 0 0 0 0 0 0 1 0 1 0 1 0 1 0 1 0 1 0 0 0 0 0 1 0 1 0 1 0 1 0 0 0 1 0 1 0 0 0 0 0 0 0 0 1 0 1
4	-18.47	0 0 0 0 0 0 0 0 0 0 0 0 0 0 0 0 0 0 0 0 0 0 1 0 0 0 0 0 1 0 1 0 1 0 1 0 1 0 0 0 0 0 0 0 0 0 0 0 0 0 1 0 1
5	-18.47	0 0 0 0 0 0 0 0 0 0 0 0 0 0 0 0 0 0 0 0 0 0 1 0 0 0 0 0 1 0 1 0 1 0 1 0 1 0 0 0 0 0 0 0 0 0 0 0 0 0 1 0 1
6	-18.89	0 0 0 0 0 0 0 0 0 0 0 0 0 0 0 0 0 0 0 0 0 1 0 1 0 0 0 1 0 1 0 1 0 1 0 1 0 0 0 0 0 1 0 1 0 1 0 1 0 1 0 1
7	-18.82	0 0 0 0 0 0 0 0 0 0 0 0 0 0 0 0 0 0 0 0 0 1 0 1 0 0 0 1 0 1 0 1 0 1 0 1 0 0 0 1 0 1 0 1 0 1 0 1 0 1 0 1
U=8	-18.45	0 0 0 0 0 0 0 0 0 0 0 0 0 0 0 0 0 0 0 0 0 0 1 0 0 0 0 0 1 0 1 0 1 0 1 0 1 0 0 0 0 0 1 0 1 0 1 0 1 0 1 0 1

(*b*)

u	SLL [dB]	GA Chromosome
1	-18.89	0 0 0 0 0 0 0 0 0 0 0 0 0 0 0 0 0 0 0 0 0 1 0 1 0 0 0 1 0 1 0 1 0 1 0 1 0 0 0 0 0 1 0 1 0 1 0 1 0 1 0 1
2	-18.89	0 0 0 0 0 0 0 0 0 0 0 0 0 0 0 0 0 0 0 0 0 1 0 1 0 0 0 1 0 1 0 1 0 1 0 1 0 0 0 0 0 1 0 1 0 1 0 1 0 1 0 1
3	-18.89	0 0 0 0 0 0 0 0 0 0 0 0 0 0 0 0 0 0 0 0 0 1 0 1 0 0 0 1 0 1 0 1 0 1 0 1 0 0 0 0 0 1 0 1 0 1 0 1 0 1 0 1
4	-18.18	0 0 0 0 0 0 0 0 0 0 0 0 0 0 0 0 0 0 0 0 0 1 0 1 0 0 0 1 0 1 0 1 0 1 0 1 0 0 0 0 0 1 0 1 0 1 0 1 0 1 0 0
5	-18.89	0 0 0 0 0 0 0 0 0 0 0 0 0 0 0 0 0 0 0 0 0 1 0 1 0 0 0 1 0 1 0 1 0 1 0 1 0 0 0 0 0 1 0 1 0 1 0 1 0 1 0 1
6	-18.89	0 0 0 0 0 0 0 0 0 0 0 0 0 0 0 0 0 0 0 0 0 1 0 1 0 0 0 1 0 1 0 1 0 1 0 1 0 0 0 0 0 1 0 1 0 1 0 1 0 1 0 1
7	-18.89	0 0 0 0 0 0 0 0 0 0 0 0 0 0 0 0 0 0 0 0 0 1 0 1 0 0 0 1 0 1 0 1 0 1 0 1 0 0 0 0 0 1 0 1 0 1 0 1 0 1 0 1
U=8	-18.18	0 0 0 0 0 0 0 0 0 0 0 0 0 0 0 0 0 0 0 0 0 1 0 1 0 0 0 1 0 1 0 1 0 1 0 1 0 0 0 0 0 1 0 1 0 1 0 1 0 1 0 0

(*c*)

u	SLL [dB]	GA Chromosome
1	-17.95	0 0 0 0 0 0 0 0 0 0 0 0 0 0 0 0 0 0 0 0 0 0 0 0 0 0 0 0 0 1 0 1 0 1 0 1 0 0 0 0 0 1 0 1 0 0 0 0 0 0 0 0 0 0
2	-17.73	0 0 0 0 0 0 0 0 0 0 0 0 0 0 0 0 0 0 0 0 0 0 0 0 0 0 0 0 0 1 0 1 0 1 0 0 0 0 0 0 0 1 0 1 0 0 0 0 0 0 0 0 0 0
3	-17.95	0 0 0 0 0 0 0 0 0 0 0 0 0 0 0 0 0 0 0 0 0 0 0 0 0 0 0 0 0 1 0 1 0 1 0 1 0 0 0 0 0 1 0 1 0 0 0 0 0 0 0 0 0 0
4	-17.95	0 0 0 0 0 0 0 0 0 0 0 0 0 0 0 0 0 0 0 0 0 0 0 0 0 0 0 0 0 1 0 1 0 1 0 1 0 0 0 0 0 1 0 1 0 0 0 0 0 0 0 0 0 0
5	-17.95	0 0 0 0 0 0 0 0 0 0 0 0 0 0 0 0 0 0 0 0 0 0 0 0 0 0 0 0 0 1 0 1 0 1 0 1 0 0 0 0 0 1 0 1 0 0 0 0 0 0 0 0 0 0
6	-17.95	0 0 0 0 0 0 0 0 0 0 0 0 0 0 0 0 0 0 0 0 0 0 0 0 0 0 0 0 0 1 0 1 0 1 0 1 0 0 0 0 0 1 0 1 0 0 0 0 0 0 0 0 0 0
7	-17.95	0 0 0 0 0 0 0 0 0 0 0 0 0 0 0 0 0 0 0 0 0 0 0 0 0 0 0 0 0 1 0 1 0 1 0 1 0 0 0 0 0 1 0 1 0 0 0 0 0 0 0 0 0 0
U=8	-17.95	0 0 0 0 0 0 0 0 0 0 0 0 0 0 0 0 0 0 0 0 0 0 0 0 0 0 0 0 0 1 0 1 0 1 0 1 0 0 0 0 0 1 0 1 0 0 0 0 0 0 0 0 0 0

(*d*)

Figure 3.16: *OTM Numerical Assessment* ($M = 8$, $N = 5$; $d = 0.5\lambda$; $T = 1.4824 \times 10^4$; $L = 28$; $B = 56$; $U = 7$; $p_c = 0.9$; $p_m = 0.01$; $I = 100$) - Chromosomal sequence of the *GA* population at the iterations (*a*) $i = 10$, (*b*) $i = 20$, and (*c*)(*d*) $i = I = 100$ for the *OTM* (*a*)(*b*)(*c*) and (*d*) when exploiting the bare *GA*-initialization.

in a local/non-optimal minimum of Φ with $SLL > -18\,dB$ (Fig. 3.13) just after 4 iterations.

The benefit of adopting the OTM smart GA-initialization can be further outlined from the perspective of the *Schemata theorem* [87], as well. Keeping in mind the key-argumentations in Sect. 3.4, one can deduce that whether the initial GA-population does not contain the "good" schemata of the global optimum, the optimization will difficulty converge to it in a reasonable/finite amount of iterations without a lucky mutation, this latter usually performed with low probability [87][94], as well. Therefore, a key-issue for increasing the convergence rate (or, at least, the probability to reach the global optimum in a finite CPU-time) to the optimal solution is to define an initialization procedure able to include the "schemata" of the (unknown) global optimum within the population $\mathbf{W}^{(0)}$. To assess this property, let us analyze the chromosomes (i.e., the coded version of the tiling words where the "schemata" can be identified) of the initial population generated in the OTM according to (3.20) [Fig. 3.15(a)] and through the "bare" strategy [Fig. 3.15(b)] with respect to the global optimum sequence [Fig. 3.15(c)]. Different color boxes highlight some representative schemata of the global-optimum chromosome [Fig. 3.15(c)]. As it can observed, these latter are all present in the initial OTM population [Fig. 3.15(a)], while only a subset of them can be found in the chromosomal sequences from the bare initialization [Fig. 3.15(b)]. For instance, the "yellow" schemata characterized by the fixed alleles $\{101\}$ at the bit positions 26, 27, and 28 is not present in Fig. 3.15(b). During the iterative process [see Figs. 3.16(a)-3.16(b) - OTM], the GA effectively recombines the best schemata of the initial population until the convergence. Unlike the bare GA [Fig. 3.16(d) - *Bare Init*], the OTM is able to find at the convergence ($i = I^{opt} = I$) the global optimum chromosome, which is also shared in almost all individuals [Fig. 3.16(c) - OTM] as an effect of the well-known genetic pressure.

In order to assess the potentialities of the GA-based tiling approach as an enabling tool for dealing with more complex/high-dimensional syntheses, the domino clustering of a larger planar array has been addressed. The array at hand is composed by 264 $\frac{\lambda}{2}$-spaced elements ($M = 22$, $N = 12$), while the two sets of reference excitations $\{\alpha_m^{ref}; \ m = 1, ..., M\}$ and $\{\alpha_n^{ref}; \ n = 1, ..., N\}$ have been still set to the Dolph-Chebyshev ones [91] to afford a power pattern with $SLL = -20\,dB$. Because of the array size, the problem cardinality is now extremely large ($T \simeq 1.9898 \times 10^{31}$), thus preventing the application of the enumerative method, while requiring the exploitation of a non-exhaustive sampling of the solution space such as that performed by the OTM. Due to the problem dimensionality, the maximum number of GA iterations has been increased with respect to the previous test case ($I = 10^3$) as well as the population size ($U = 2 \times L = 462$ [94], $L = 231$ being the number of unknowns equal the number of internal vertices). On the other hand, it is worth pointing out that, despite the
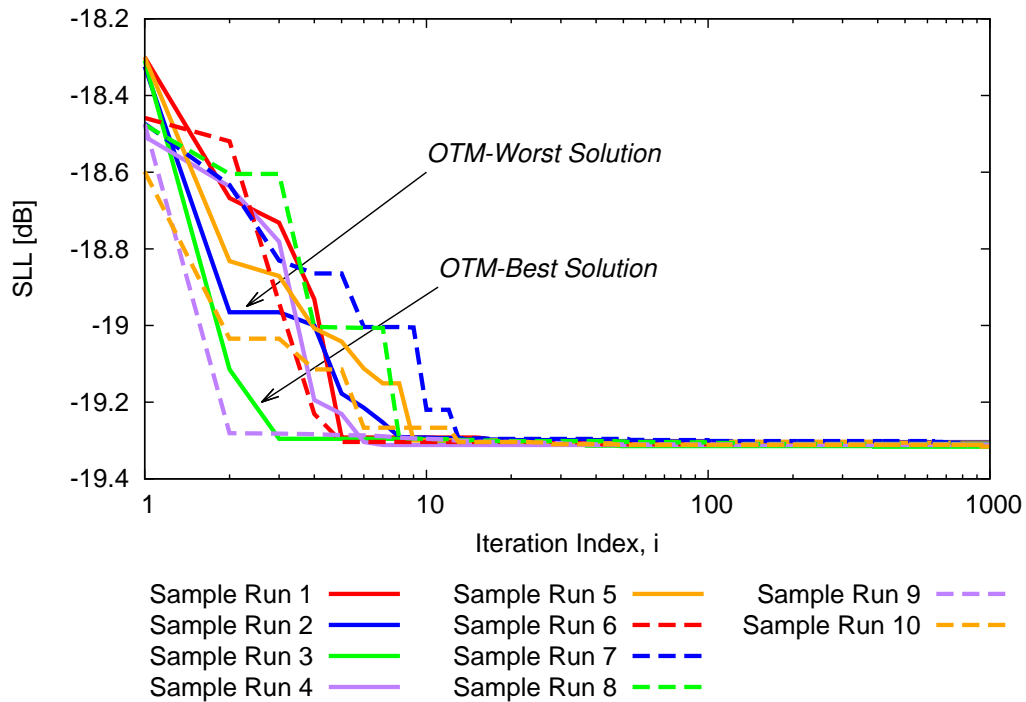
Figure 3.17: *OTM Numerical Assessment ($M = 22$, $N = 12$; $d = 0.5\lambda$; $T \simeq 1.99 \times 10^{31}$; $L = 231$; $B = 693$; $U = 462$; $p_c = 0.9$; $p_m = 0.01$; $I = 1000$) - Behavior of $\Phi\left(\mathbf{c}_i^{opt}\right)$ versus the iteration index, $i = 1, ..., I$, for 10 representative OTM sample runs including the best, ς^{best}, and the worst, ς^{worst}, cases within the whole set of $\Omega = 100$ tests.*

Table 3.7: *OTM Numerical Assessment* ($M = 22$, $N = 12$; $d = 0.5\lambda$; $T \simeq 1.99 \times 10^{31}$; $L = 231$; $B = 693$; $U = 462$; $p_c = 0.9$; $p_m = 0.01$; $I = 1000$) - *Minimal tiling* word, $\mathbf{w}_0^{(1)} = \mathbf{w}^{(t)}\big|_{t=1}$, *maximal tiling* word, $\mathbf{w}_0^{(\tilde{U})} = \mathbf{w}^{(t)}\big|_{t=T}$, and intermediate tiling words, $\mathbf{w}_0^{(7)}$ and $\mathbf{w}_0^{(14)}$, of the initial *OTM* population.

u	$\mathbf{w}_0^{(u)}$	
1	0000000000000000000000000000000000000000000000000000000000 0000000000000000000000000000000000000000000000000000000000 0000000000000000000000000000000000000000000000000000000000 000000000000000000000000000000000000000000000000000000	$= \mathbf{w}^{(t)}\big|_{t=1}$
7	11111111111111111111111111111111111111111111111111111111111 11111111111111111111111111111111111111111111111111111111111 11111111111111111111111111111111111111111111111111111111111 11111111111111111111111111111111111111111111111111111111	
14	1111111111111111111111222222222222222222222211222222222222222 2222112222222222222222222211222333333333333322211222333333 333333322211222333333333333333322211222222222222222222221122222 2222222222222211222222222222222222222111111111111111111111	
$\tilde{U} = 22$	1111111111111111111111222222222222222222222211233333333333333 3332112344444444444444443211234555555555555543211234566666 6666654321123455555555555555432112344444444444444443211233333 333333333333211222222222222222222222111111111111111111111	$= \mathbf{w}^{(t)}\big|_{t=T}$

increment of the upper bound of the number of samples of the solution space (i.e., $U \times I\big|_{M \times N=22 \times 12} = 4.62 \times 10^5$ vs. $U \times I\big|_{M \times N=8 \times 5} = 8 \times 10^2$), the ratio between the maximum number of trial solutions checked during the iterative multi-agent optimization process and the set of complete tiling solutions has been drastically reduced (i.e., $\frac{U \times I}{T}\big|_{M \times N=22 \times 12} = 2.3 \times 10^{-26}$ vs. $\frac{U \times I}{T}\big|_{M \times N=8 \times 5} = 5.4 \times 10^{-2}$). According to the *OTM*, the *GA*-optimization has been initialized with $\tilde{U} = 22$ tiling words being $w^{max} = 6$. The *minimal tiling* word, $\mathbf{w}_0^{(1)} = \mathbf{w}^{(t)}\big|_{t=1}$, the *maximal tiling* word, $\mathbf{w}_0^{(\tilde{U})} = \mathbf{w}^{(t)}\big|_{t=T}$, and other two intermediate words (i.e., $\mathbf{w}_0^{(7)}$ and $\mathbf{w}_0^{(14)}$) of the initial trial population are reported in Tab. 3.7. Also in this case, the *GA* has been run $\Omega = 100$ times with different initial populations unless the analytically-defined $\tilde{U} = 22$ individuals. Unlike the previous case, all optimizations converged, in less than 10 hours, to a different final solution because of the extremely large problem cardinality, but all with *SLL* values below that of the best solution achievable for the smaller array $[\Phi(\mathbf{c}_\omega^{opt}) < -19.3\,dB$, $\forall \omega = 1, ..., \Omega$, while $SLL^{best}\big|_{M \times N=8 \times 5} = -18.89\,dB]$. This outcome is not surprising (even though it further confirms that the optimizer at hand "guarantees" what physically expected) since the number of domino tiles in the larger array is greater and therefore the quantization issues, causing the undesired high sidelobes, are less critical. What is relevant for assessing the effectiveness of the *OTM* in sampling a so-large solution space is that the discrepancy between the *SLL* performance of the worst ($\varsigma^{worst} \triangleq \arg(\min_{\omega=1,..,\Omega}\{\Phi(\mathbf{c}_\omega^{opt})\})$ - *OTM Worst Solution*) and the best (ς^{best} - *OTM Best Solution*) *GA* solutions is only $0.01\,dB$ (Tab. 3.8). For completeness, Figure 3.17 shows the behavior of $\Phi(\mathbf{c}_i^{opt})$ versus the iteration index, $i = 1, ..., I$, for 10 representative *OTM* runs, while the tiling configuration, the values of the resulting sub-array amplitude weights, and the

Figure 3.18: *OTM Numerical Assessment* ($M = 22$, $N = 12$; $d = 0.5\lambda$; $T \simeq 1.99 \times 10^{31}$; $L = 231$; $B = 693$; $U = 462$; $p_c = 0.9$; $p_m = 0.01$; $I = 1000$) - Plots of the (a)(b) the tiling configurations and the sub-array excitation amplitudes and (c)(d) the power pattern of the best, ς^{best}, and the worst, ς^{worst}, cases within the whole set of $\Omega = 100$ tests.

power patterns of the $OTM - Best\, Solution$ and of the $OTM - Worst\, Solution$ are shown on the left and the right column of Fig. 3.18, respectively. From Figures 3.18(a)-3.18(b), it turns out that a large part of the dominoes are horizontal, σ_H, while only 34 [Fig. 3.18(a)] and 36 [Fig. 3.18(b)] over 132 are vertical, σ_V, respectively.

In order to assess the proposed approach also when dealing with steered beam syntheses, the next benchmark example is concerned with the complete tiling of the same aperture of the previous example, but now providing the minimum SLL when the main lobe is steered in both principal planes, namely towards $(\theta_0, \phi_0) = (30, 90)$ [deg] and $(\theta_0, \phi_0) = (30, 0)$ [deg]. The best solution found at the convergence among $\Omega = 100$ OTM-GA runs for each pointing direction is shown in Fig. 3.19. Firstly, it is interesting to point out that the best tilings [Fig. 3.19(a) and Fig. 3.19(b)] are quite different from that synthesized when constraining the beam to point along boresight $(\theta_0, \phi_0) = (0, 0)$ [deg] (Fig. 3.18). Moreover, it is interesting to point out that there is a prevalence of horizontal tiles, σ_H, in Fig. 3.19(a) and vertical tiles, σ_V, in Fig. 3.19(b) since they are the
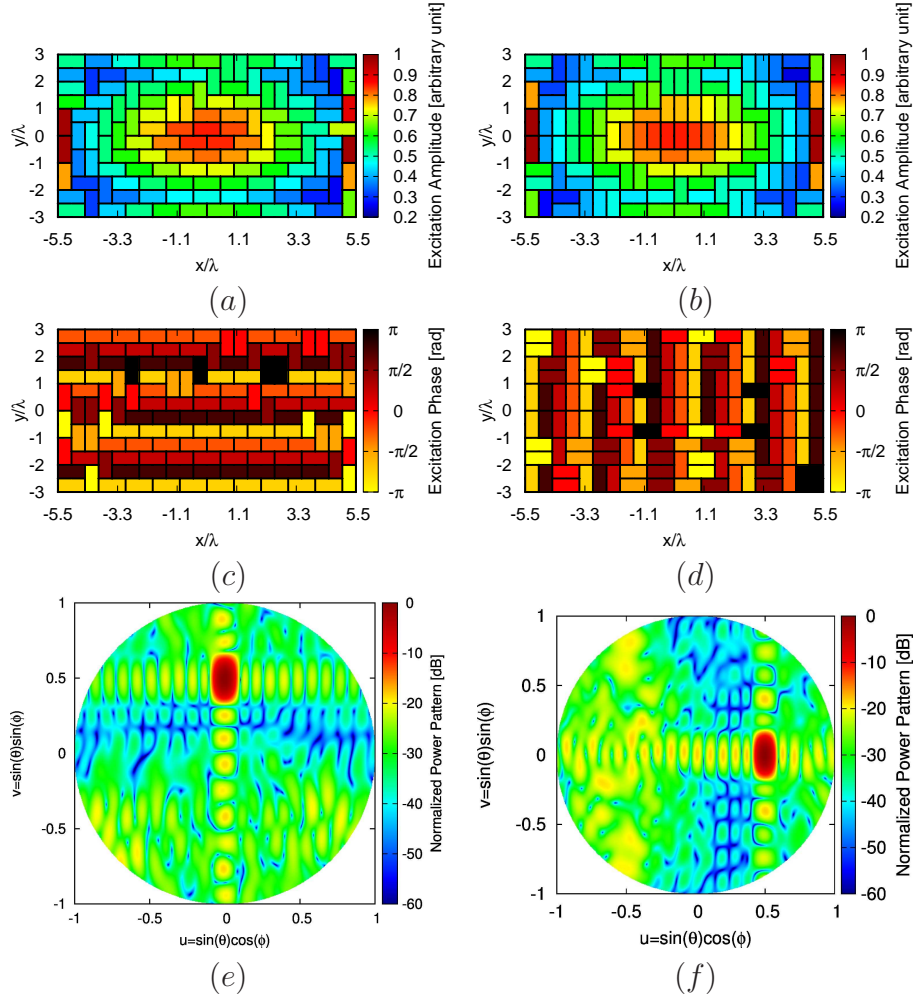
Figure 3.19: *OTM Numerical Assessment* ($M = 22$, $N = 12$; $d = 0.5\lambda$; $T \simeq 1.99 \times 10^{31}$; $L = 231$; $B = 693$; $U = 462$; $p_c = 0.9$; $p_m = 0.01$; $I = 10^3$) - Plots of the tiling configurations and the sub-array excitation $(a)(b)$ amplitudes and $(c)(d)$ phases, and $(e)(f)$ the power pattern of the best case within the whole set of $\Omega = 100$ tests when steering the beam towards $(a)(c)(e)$ $(\theta_0, \phi_0) = (30, 90)$ $[deg]$ and $(b)(d)(f)$ $(\theta_0, \phi_0) = (30, 0)$ $[deg]$.

(a)   (b)   (c)
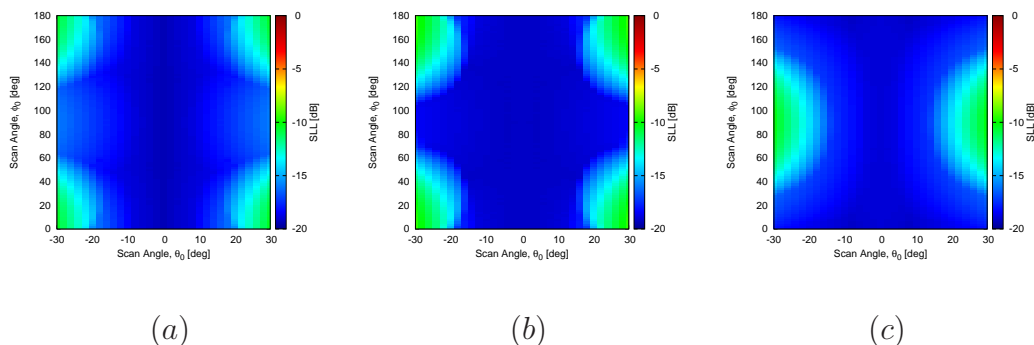
Figure 3.20: *OTM Numerical Assessment* ($M = 22$, $N = 12$; $d = 0.5\lambda$; $T \simeq 1.99 \times 10^{31}$; $L = 231$; $B = 693$; $U = 462$; $p_c = 0.9$; $p_m = 0.01$; $I = 1000$) - *SLL* values of the patterns generated by tiling configurations optimized for (*a*) $(\theta_0, \phi_0) = (0, 0)$ [*deg*] [Fig. 3.18(*a*)], (*b*) $(\theta_0, \phi_0) = (30, 90)$ [*deg*] [Fig. 3.19(*a*)], and (*c*) $(\theta_0, \phi_0) = (30, 0)$ [*deg*] [Fig. 3.19(*b*)] when scanning the beam in the sector $\{\theta_0 \in [-30, 30]\ [deg],\ \phi_0 \in [0, 180]\ [deg]\}$.

ones least affected by quantization when scanning the beam in the $\phi_0 = 90$ [*deg*] plane [Fig. 3.19(*e*)] and in the $\phi_0 = 0$ [*deg*] plane [Fig. 3.19(*f*)], respectively. As for the radiation performance, the peak level of the sidelobes of the power patterns in Fig. 3.19 is equal to $SLL = -18.33\,dB$ [Fig. 3.19(*e*)] and $SLL = -18.12\,dB$ [Fig. 3.19(*f*)], that is $1\,dB$ worse than that for the broadside case (Tab. 3.8 - $SLL = -19.32\,dB$). This is due to the phase quantization deriving from the use of a single phase shifter for each domino tile [Fig. 3.19(*c*) and Fig. 3.19(*d*)]. For completeness and in order to characterize the scanning performance of a synthesize array, the SLL values obtained when steering the main lobe in the sector $\theta_0 \in [-30, 30]$ [*deg*] and $\phi_0 \in [0, 180]$ [*deg*] are shown in Fig. 3.20 for the three tiling configurations optimized for $(\theta_0, \phi_0) = (0, 0)$ [*deg*] [Fig. 3.20(*a*)], $(\theta_0, \phi_0) = (30, 90)$ [*deg*] [Fig. 3.20(*b*)], and $(\theta_0, \phi_0) = (30, 0)$ [*deg*] [Fig. 3.20(*c*)]. It is possible to observe that a prevalence of horizontal tiles, σ_H, [Fig. 3.18(*a*) and Fig. 3.19(*a*)] provides lower SLL values when scanning the beam in the plane with $\phi_0 = 90$ [*deg*] [Figs. 3.20(*a*)-3.20(*b*)] because they are the least affected by quantization. Viceversa, better SLL performance are achieved in the $\phi_0 = 0$ [*deg*] (or $\phi_0 = 180$ [*deg*]) plane in case there are more vertical tiles, σ_v, [Fig. 3.19(*b*)].

3.4.1.2 Real-Elements Arrays

Finally, the practical reliability of the results from the proposed analytically-driven clustering methodology has been validated by considering arrays made of real radiating elements, as well. The aim is to show that, as expected, for moderate scanning angles, the element pattern does not significantly affect the synthesis results. Towards this end, the same tiling configurations

Table 3.8: *OTM Numerical Assessment* ($M = 22$, $N = 12$; $d = 0.5\lambda$; $T \simeq 1.99 \times 10^{31}$; $L = 231$; $B = 693$; $U = 462$; $p_c = 0.9$; $p_m = 0.01$; $I = 1000$) - Radiation indexes (SLL, D, $HPBW_{az}$, $HPBW_{el}$) of the reference solution as compared to the best, ς^{best}, and the worst, ς^{worst}, cases within the whole set of $\Omega = 100$ *OTM* tests.

	SLL [dB]	D [dBi]	$HPBW_{az}$ [deg]	$HPBW_{el}$ [deg]
Reference	-20.00	28.46	4.82	9.13
OTM $-$ Best Solution	-19.32	28.51	4.82	9.11
OTM $-$ Worst Solution	-19.31	28.52	4.82	9.11
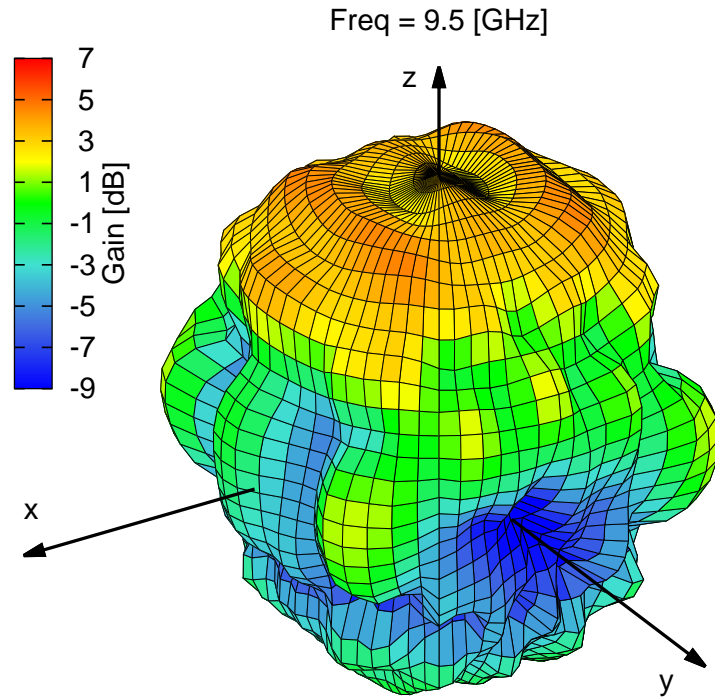
Figure 3.21: $3D$ Plot of the embedded gain pattern of the aperture-stacked patch microstrip antennas [93] resonating at the central operation frequency of $9.5\,GHz$ and located in a two rings of neighboring elements.
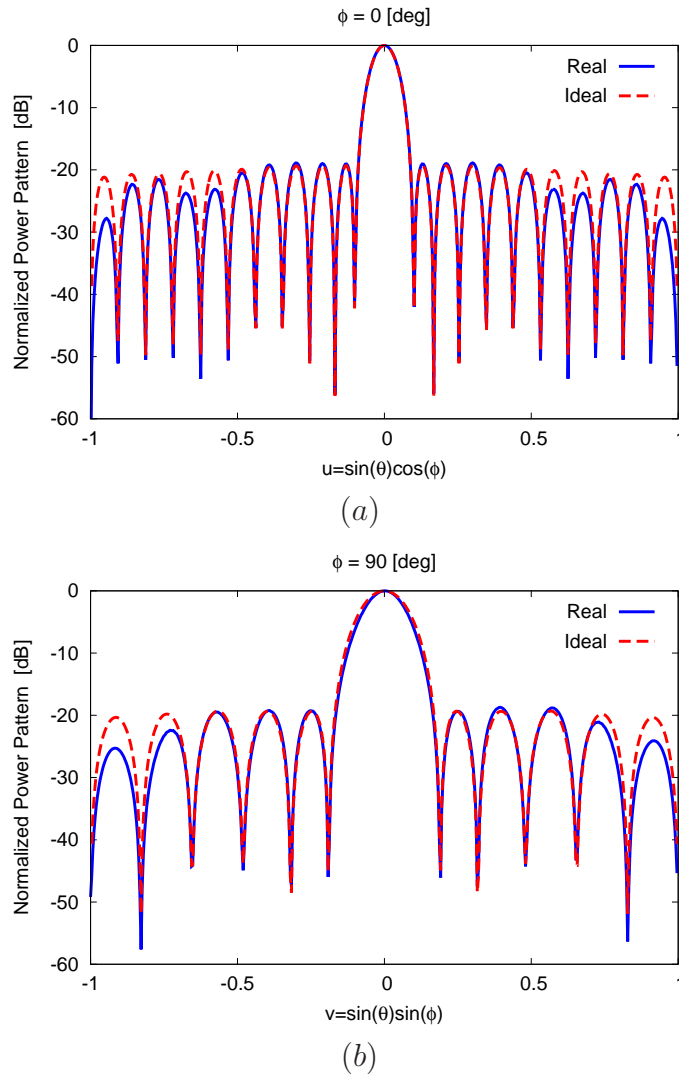
Figure 3.22: *OTM Numerical Assessment* (*Real Element Array*; $M = 22$, $N = 12$; $d = 0.5\lambda$) - Power pattern radiated by the ideal and the real arrays when setting the mainlobe steered along broadside: (*a*) horizontal ($\phi = 0 \, [deg]$) and (*b*) vertical ($\phi = 90 \, [deg]$) cuts.
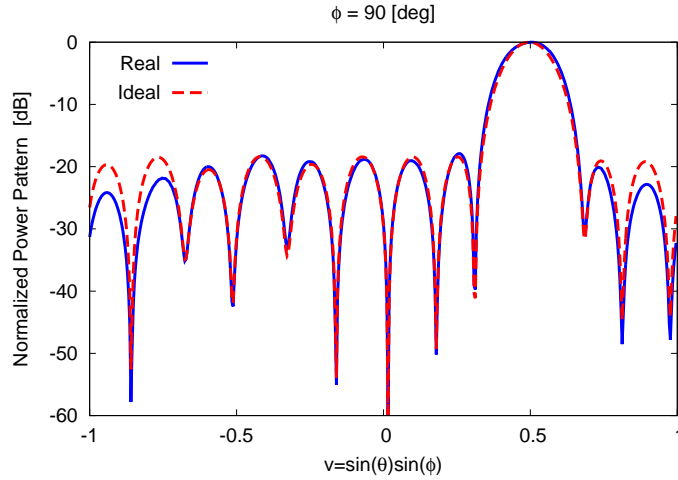
Figure 3.23: *OTM Numerical Assessment* (*Real Element Array*; $M = 22$, $N = 12$; $d = 0.5\lambda$) - Vertical ($\phi = 90\,[deg]$) cut of the power pattern radiated by the ideal and the real arrays when setting the mainlobe steered at $(\theta_0, \phi_0) = (30, 90)\,[deg]$.

for the aperture $M \times N = 22 \times 12$ synthesized when steering the beam along $(\theta_0, \phi_0) = (0, 0)\,[deg]$ and $(\theta_0, \phi_0) = (30, 90)\,[deg]$ have been considered, but substituting the isotropic/ideal elements with aperture-stacked patch microstrip antennas [93] resonating at the central operation frequency of $9.5\,GHz$. As for this latter, the embedded element pattern, $\hat{\underline{f}}(\theta, \phi)$, radiated at $9.5\,GHz$ has been calculated through a full-wave simulation when considering the interactions of two rings of neighboring elements (the results are coincident also when enlarging the neighbour set) so as to include the coupling effects is shown in Fig. 3.21. Figure 3.22 compares the normalized[7] broadside, $(\theta_0, \phi_0) = (0, 0)\,[deg]$, power pattern of the real and the ideal arrays $[\hat{\underline{f}}(\theta, \phi) = 1]$ along the horizontal [Fig. 3.22(a)] and the vertical [Fig. 3.22(b)] cuts. As it can be noticed, the behavior of the power pattern in the mainlobe region as well as for the first sidelobes for the real case turns out to be very similar to the ideal one since $\hat{f}(\theta, \phi)$ has a large beamwidth. Overall, the sidelobe of the real array is equal to $\overline{SLL} = -18.72\,dB$, thus there is a deterioration of $0.55\,dB$ with respect to the ideal case. Similar conclusions hold true also for the synthesis when setting the steering direction at $(\theta_0, \phi_0) = (30, 90)\,[deg]$ as proved by the plots along the steering plane (i.e., the vertical one) in Fig. 3.23.

---

[7]Each pattern has been normalized to its maximum in order to compare the SLL values.

Chapter 4

Mask-Constrained Optimization of Domino-Tiled Phased Arrays

In this Chapter a set of techniques based on the enumerative/optimization based methods presented in the previous Chapter, are presented to address the mask matching synthesis problem, considering pencil shaped beams. Starting from a set of ideal requirements on the array radiation performances defined by a power mask, the proposed methods aim at finding the optimal tiling configuration minimizing the mismatch of the tiled array power pattern with the mask. Optimal tiles excitations coefficients are obtained by means of convex optimization methods. The numerical assessment validates the proposed approaches, as well as the reliability assessment of the optimized solutions when considering real radiating elements through commercial full-wave simulators.

4.1 Introduction

The design of phased array antennas usually requires that the radiation pattern complies with a power mask, defining the maximum/minimum radiated power over a set of angular directions. In this way the user is allowed to define the desired radiation performances with high precision and high flexibility. As instance, it is possible to request a very low SLL only in a limited angular region for interfering signals suppression. Accordingly, the synthesis of tiled phased arrays minimizing the distance of the power pattern with user-defined reference power masks is here addressed. The matching with an user-defined power mask is considered as cost function of the tiling optimization, with the aim of find an optimal tiled arrays (i.e. a compromise with respect to the ideal fully populated array) whose power pattern is as close as possible to the reference mask. A set of new optimization methods, namely the $ETM - CP$, $EM - ETM/CP$, and $EM - OTM/CP$ methods, are proposed, addressing the mask matching tiling optimization by jointly combining enumerative/GA-based approaches with optimal convex strategies, for the optimization of the tiling configuration and of the tiles excitations coefficients. The presented techniques positively compared with the ETM and OTM optimization methods presented in the previous chapters, which unavoidably fail when dealing with a mask matching synthesis problem.

> *Mask Constrained Tiling Synthesis Problem* - given an array of $M \times N$ isotropic elements, positioned over a rectangular lattice, and two domino-like tiles $\left(\sigma^V, \sigma^H\right)$, find the optimal tiling/clustering configuration $\mathbf{c}^{opt}$ and the corresponding sub-array weights $\boldsymbol{\alpha}^{opt}$ and $\boldsymbol{\beta}^{opt}$, such that the pencil beam pattern radiated by the tiled array maximizes the matching with an user-defined power mask $M\left(u, v\right)$.

Accordingly, the cost function of the tiling optimization problem is defined as:

$$\Phi\left(\mathbf{c}; \boldsymbol{\alpha}, \boldsymbol{\beta}\right) = \chi\left(\mathbf{c}; \boldsymbol{\alpha}, \boldsymbol{\beta}\right) + \frac{\mathcal{H}\left[-\chi\left(\mathbf{c}; \boldsymbol{\alpha}, \boldsymbol{\beta}\right)\right]}{D\left(u_0, v_0\right)} \qquad (4.1)$$

where $D\left(u_0, v_0\right)$ is the peak directivity, $\left(u_0, v_0\right)$ being the beam pointing direction, and

$$\chi\left(\mathbf{c}; \boldsymbol{\alpha}, \boldsymbol{\beta}\right) = \max_{(u,v) \in \mathcal{V}} \left\{ \left|P\left(u, v\right) - M\left(u, v\right)\right| \mathcal{H}\left[P\left(u, v\right) - M\left(u, v\right)\right] \right\} \qquad (4.2)$$

is the maximum violation of the power pattern from the power mask in the $\left(u, v\right)-$plane, within the visible region $\mathcal{V} = \left\{(u, v) : u^2 + v^2 < 1\right\}$. Moreover $P\left(u, v\right)$ is the power pattern of the clustered array given as $P\left(u, v\right) = \left|AF\left(u, v; \mathbf{c}\right)\right|^2$, while $\mathcal{H}\left[\cdot\right]$ is the Heaviside function. As expressed by (4.1) the mask matching is

defined as the maximum distance of the power pattern from the mask $\chi\left(\mathbf{c};\boldsymbol{\alpha},\boldsymbol{\beta}\right)$ only in case the power pattern is above the mask, otherwise, the cost function accounts only the second term [i.e. the ratio $1/D\left(u_0, v_0\right)$] with the purpose of peak directivity maximization. Consequently, the ideal optimum (i.e. when $\chi\left(\mathbf{c};\boldsymbol{\alpha},\boldsymbol{\beta}\right) = 0$) is reached only if the power pattern is below the power mask in all the (u, v) points of $\mathcal{V}$. Such optimal matching can be easily obtained when considering conventional fully-populated architectures, providing feasible mask constraints. When instead a clustered architecture is considered, which is intrinsically a sub-optimal solution with respect to a fully-populated array, a perfect matching cannot be assured. Indeed, it is worth to point out here that the aim of the proposed methodologies is not to exactly fit the reference mask, but to find the closest compromise solution to a perfect mask matching.

4.2 Enumerative Approach with Convex Programming Optimization of Sub-Array Weights

As explained in detail in Chapter 2, the global optimum of the domino tiling synthesis problem can be theoretically reached by means of a full-global optimization approach, by jointly optimize the tiling configuration $\mathbf{c}$ and the tiles excitations coefficients $\boldsymbol{\alpha}, \boldsymbol{\beta}$. Such optimization approach turns out to be computationally unfeasible in most of the cases, mainly due to the wide solutions space when dealing with medium/large antenna apertures. The nested-optimization method is therefore proposed, by jointly exploiting the ETM approach and a Convex Programming (CP) optimization [100][101][102][28], denoted as ETM-CP and defined by the following steps:

- **Step 1.** *Tilings Enumeration*: the optimal tiling generation method described in Chapter 3 is used for the enumeration of the whole set of clustering configurations $\mathbf{C}_\infty = \left\{\mathbf{c}^{(t)}; t = 1, ..., T\right\}$

- **Step 2.** *CP Optimizations*: given the power mask $M\left(u, v\right)$ defining the ideal requirements on the power pattern, the following optimization problem is solved

$$\left(\boldsymbol{\alpha}_t^{CP}, \boldsymbol{\beta}_t^{CP}\right) = \arg\left[\min_{\boldsymbol{\alpha}_t, \boldsymbol{\beta}_t}\left\{\Phi\left(\boldsymbol{\alpha}_t, \boldsymbol{\beta}_t \,|\mathbf{c}_t\right)\right\}\right] \qquad (4.3)$$

where for each tiling $\mathbf{c}_t$, $t = 1, ..., T$, the optimization the sub-array weights is performed through the CP strategy presented in [102], in which the maximization of the power pattern directivity along the sum beam pointing direction is maximized, still satisfying the power mask $M\left(u, v\right)$. More in detail the power mask $M\left(u, v\right)$ is uniformly discretized in R sampling directions, (u_r, v_r), $r = 1, ..., R$ and a standard CP-based optimization technique is used to obtained the optimal subarray amplitude and phase

excitations $\left(\boldsymbol{\alpha}_t^{CP}, \boldsymbol{\beta}_t^{CP}\right)$ of the t-th trial clustering configuration $\mathbf{c}_t$, are obtained solving the following minimization problem

$$\min_{\Re\{\mathbf{I}_t\}, \Im\{\mathbf{I}_t\}} \int_0^\pi \int_0^{2\pi} P\left(\theta, \phi; \mathbf{c}_t\right) \sin\left(\theta\right) d\theta d\phi \qquad (4.4)$$

subject to the following constraints

$$P\left(u_0, v_0; \mathbf{c}_t\right) = 1 \qquad (4.5)$$

$$P\left(u_r, v_r; \mathbf{c}_t\right) \leq M\left(u_r, v_r\right) \\ r = 1, ..., R \qquad (4.6)$$

where in (4.4) $\mathbf{I}_t = \left\{I_{q,t} = \alpha_{q,t} e^{j\beta_{q,t}}; q = 1, ..., Q\right\}$ and $\Re$ and $\Im$ stand for real and imaginary part, respectively. The minimization of (4.4) subject to (4.5) implies the maximization of the antenna directivity (assuming the array does not radiate in the back half-space), defined as

$$D = \frac{4\pi \left|P\left(u_0, v_0; \mathbf{c}_t\right)\right|^2}{\int_0^\pi \int_0^{2\pi} \left|P\left(\theta, \phi; \mathbf{c}_t\right)\right|^2 \sin\left(\theta\right) d\theta d\phi}. \qquad (4.7)$$

- **Step 3.** *Cost Function Evaluation*: evaluation of the mask matching (4.1) between the tiled array power pattern $P\left(u, v; \mathbf{c}^{ETM-CP}\right)$ and the power mask $M\left(u, v\right)$, for each of the T $CP-$optimized solutions and selection of the best tiling/sub-array weights as

$$\left(\mathbf{c}^{ETM-CP}; \boldsymbol{\alpha}^{ETM-CP}, \boldsymbol{\beta}^{ETM-CP}\right) = \arg\left[\min_{t=1,...,T}\left\{\Phi\left(\mathbf{c}_t; \boldsymbol{\alpha}_t^{CP}, \boldsymbol{\beta}_t^{CP}\right)\right\}\right] \qquad (4.8)$$

The above procedure allows to reach the optimum of our problem with a total computational time equal to $\Delta t^{ETM-CP} = \Delta t^{ETM} + T\Delta t^{CP} + T\Delta t^\Phi$, being Δt^{ETM} the time necessary for the ETM simulation, Δt^{CP} is the time for a single CP optimization and Δt^Φ is the time for the evaluation of (4.1). It is worth noting here that the feasibility of the nested optimization, depends by: i) the cardinality of the solution space, dictated by T; ii) the computational cost needed to solve (4.4) under the constraints (4.5) and (4.6). Therefore, in case of small/medium arrays, even if T allows to enumerate $\mathbf{C}_\infty = \left\{\mathbf{c}^{(t)}; t = 1, ..., T\right\}$ in a reasonable time, the optimization is still compromised by (2.5), which turns out to be the real bottleneck of the nested optimization approach.

4.3 Excitation Matching-Based Approaches

In order to deal with medium/large arrays, a further approximation is needed. As done in the ETM technique presented in Chapter 3, the $ETM-CP$ method

is reduced to an excitation matching (EM) ETM approach, allowing a fast computation of the tiles excitations coefficients, by means of analytic relationships. Anyway such approximation is exploited only for the search of the optimal clustering configuration, while the final sub-array amplitude and phase coefficients are re-optimized using a CP-based optimization. Such an approach, called EM-ETM/CP, is implemented throughout the following procedural steps:

- **Step 1.** *Reference Array*: given the power mask $M(u, v)$ defining the ideal requirements on the power pattern, the optimal reference excitations weights $I^{ref} = \alpha_{mn}^{ref} e^{j\beta_{mn}^{ref}}$, $m = 1, \ ... \ , \ M$, $n = 1, \ ... \ , \ N$ are obtained through a CP optimization of the $M \times N$ fully-populated array [Fig. 2.1(a)];

- **Step 2.** *Tilings Enumeration*: the height function based methodology (Chapter 3) is used for the enumeration of the whole set of clustering configurations $\mathbf{c}_t;$, $t = 1, ..., T$;

- **Step 3.** *EM Sub-array Weights*: for each tiling $\mathbf{c}_t;$, $t = 1, ..., T$, the optimal compromise EM excitations coefficients $\left(\boldsymbol{\alpha}_t^{EM}, \boldsymbol{\beta}_t^{EM}\right)$ are obtained minimizing the following excitation matching problem

$$\left(\boldsymbol{\alpha}_t^{EM}, \boldsymbol{\beta}_t^{EM}\right) = \arg\left[\min_{\boldsymbol{\alpha},\boldsymbol{\beta}}\left\{\sum_{m=1}^{M}\sum_{n=1}^{N}\left|I_{mn}^{ref} - I_{mn}\right|\right\}\right] \qquad (4.9)$$

The optimal amplitudes and phase coefficients solving (4.9), turn out to be analytically obtained as [29]

$$\alpha_{q,t}^{EM} = \frac{1}{2}\sum_{n=1}^{N}\sum_{m=1}^{M}\alpha_{mn}^{ref}\delta_{c_{mn}q}, \ q = 1, ..., Q \qquad (4.10)$$

$$\beta_{q,t}^{EM} = \frac{1}{2}\sum_{n=1}^{N}\sum_{m=1}^{M}\beta_{mn}^{ref}\delta_{c_{mn}q}, \ q = 1, ..., Q \qquad (4.11)$$

- **Step 4.** *Cost Function Evaluation*: evaluation of the mask matching (4.1) for each of the T solutions and selection of the best tiling/sub-array weights, solving

$$\left(\mathbf{c}^{EM-ETM}; \boldsymbol{\alpha}^{EM-ETM}, \boldsymbol{\beta}^{EM-ETM}\right) = \arg\left[\min_{t=1,...,T}\left\{\Phi\left(\mathbf{c}_t; \boldsymbol{\alpha}_t^{EM}, \boldsymbol{\beta}_t^{EM}\right)\right\}\right] \quad (4.12)$$

- **Step 5.** *CP Optimization*: single final CP optimization of the amplitude and phase excitations of the $EM-$optimized clustering vector $\mathbf{c}^{EM-ETM}$

$$\left(\boldsymbol{\alpha}^{EM-ETM/CP}, \boldsymbol{\beta}^{EM-ETM/CP}\right) = \arg\left[\min_{\boldsymbol{\alpha},\boldsymbol{\beta}}\left\{\Phi\left(\boldsymbol{\alpha}, \boldsymbol{\beta} \,\middle|\, \mathbf{c}^{EM-ETM}\right)\right\}\right]$$
$$(4.13)$$

The EM-based methods allows to optimize the tiling with a total computational time equal to $\Delta t^{EM-ETM/CP} = \Delta t^{EM-ETM} + 2\Delta t^{CP} + T\Delta t^{\Phi}$, being Δt^{EM-ETM} the time necessary for the ETM simulation, including the EM excitation computation and the cost function. The use of the analytic formulas (4.10) and (4.11), allows a fast computation of the tiles excitations weights. In this case the convergence of the solution $\left(\mathbf{c}^{EM-ETM}; \boldsymbol{\alpha}^{EM-ETM/CP}, \boldsymbol{\beta}^{EM-ETM/CP}\right)$ toward the global optimum of the addressed problem cannot be assured as in (2.3), anyway the best possible compromise solution obtained in a feasible amount of time, is provided. Finally, in case T is large enough to make both $ETM-CP$ and $EM-ETM/CP$ methods unfeasible, the OTM methodology is used instead of the ETM method in Steps 2-5 of the $EM-ETM/CP$ procedure. For such an approach, called $EM\text{-}OTM/CP$, the Step 4 is implemented as

$$\left(\mathbf{c}^{EM-OTM}; \boldsymbol{\alpha}^{EM-OTM}, \boldsymbol{\beta}^{EM-OTM}\right) = \arg\left[\min_{k=1,...,K}\left\{\min_{\mathbf{c}_{t(k)}}\left\{\Phi\left(\mathbf{c}_{t(k)}; \boldsymbol{\alpha}_{t(k)}^{EM}, \boldsymbol{\beta}_{t(k)}^{EM}\right)\right\}\right\}\right]$$
$$(4.14)$$

where the set $\mathbf{c}_{t(k)} \subset \mathcal{T}$ is a fraction of the whole solution space, explored by the OTM at the $k-$th iteration, K being the maximum user-defined iterations number. Finally the optimal sub-array weights are obtained as:

$$\left(\boldsymbol{\alpha}^{EM-OTM/CP}, \boldsymbol{\beta}^{EM-OTM/CP}\right) = \arg\left[\min_{\boldsymbol{\alpha},\boldsymbol{\beta}}\left\{\Phi\left(\boldsymbol{\alpha}, \boldsymbol{\beta}\,|\mathbf{c}^{EM-OTM}\right)\right\}\right]. \quad (4.15)$$

4.4 Numerical Assessment

4.4.1 Small Dimensions Arrays

Let us consider a small rectangular aperture of dimensions $2.5\lambda \times 2\lambda$, filled by $M \times N = 5 \times 4$ elements, located over a square lattice, equally spaced by $d_x = d_y = \lambda/2$. The ideal design requirements are defined by the power mask of Fig. 4.1, where a rectangular window of dimension $BW_u \times BW_v = 1.00\,[u] \times 1.12\,[v]$ is allowed for the main beam, a sidelobe level equal to $SLL_{L1} = -20\,[\text{dB}]$ is required for the first sidelobes near the main beam, while the end-fire sidelobes along the azimuth plane are lowered to $SLL_{L2} = -25\,[\text{dB}]$. As can be seen the mask shows two symmetries along the azimuth ($\phi = 0\,[\text{deg}]$) and elevation ($\phi = 90\,[\text{deg}]$) planes, accordingly, the phase coefficients of the fully populated array are set to $\beta_{mn}^{ref} = 0, m = 1,...,M$, $n = 1,...,N$, while the amplitude coefficients have been optimized using a CP optimization strategy, obtaining the amplitudes showed in Fig. 4.2(a). The CP optimization has been carried out considering a maximum number of iterations equal to $I = 200$, and a fitness threshold equal to $\tau = 10^{-6}$ (the threshold τ is an user-defined value used to discriminate the solutions for which the mask matching $\chi(\mathbf{c}; \boldsymbol{\alpha}, \boldsymbol{\beta})$ is considered $\chi(\mathbf{c}; \boldsymbol{\alpha}, \boldsymbol{\beta}) = 0$). The top view of the corresponding synthesized ideal power pattern is shown in
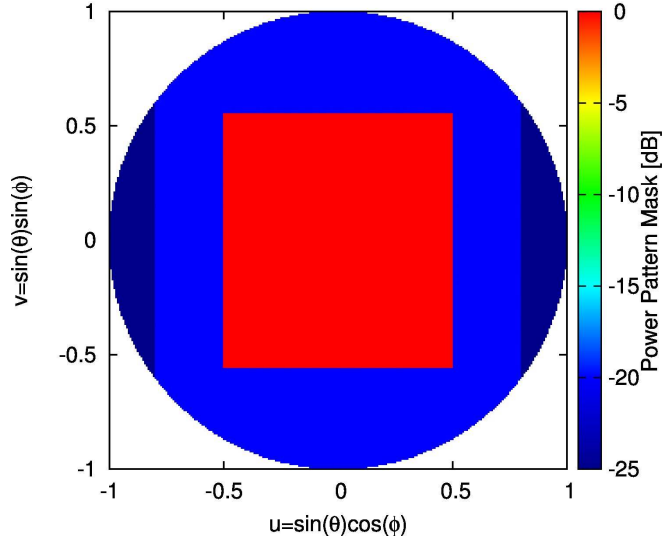
Figure 4.1: *Numerical Assessment (Small Array, Symmetric Mask*; $d = 0.5\lambda$,
$M \times N = 5 \times 4$ $N_{tot} = 20$, $T = 95$) - The power mask $M(u, v)$ defining the
constraints for the synthesis of an $M \times N = 5 \times 4$ array of isotropic elements.

Fig. 4.2(b). According to (3.4), the considered array allows to entirely cover
the aperture with $Q = 10$ tiles in $T = 95$ different ways. The limited number
of tiling configurations enables a full-global optimization approach, consequently
the $ETM - CP$ simulation has been executed in $\Delta t^{ETM-CP} = 9 : 44 : 30$
[h:min:sec] considering the same CP parameters used for the reference array
synthesis. Figure 4.3(a) shows the sorted values of the mask matching evaluated
for the T solutions. In order to discriminate among the convergent solutions
(i.e. solutions yielding a power pattern that completely fits the power mask) and
the non convergent solutions (i.e. the power pattern violates the power mask)
the fitness threshold is reported in the figure as a black dashed line. As can
be seen 6 $ETM - CP$ solutions have cost-function value that is below the fit-
ness threshold. The global optimum [Fig. 4.4(a)] has been analyzed in detail,
computing the radiated power pattern [Fig. 4.4(b)] and the respective power
pattern descriptors, namely the SLL, $HPBW_{AZ}$, $HPBW_{EL}$ D, reported in Tab
4.1. The comparisons of the power pattern with the power mask of the best
$ETM - CP$ solution, along the azimuth and elevation planes, are reported in
Fig. 4.3(b) and Fig. 4.3(c), respectively. As can be seen, the power pattern
completely meets the power mask, also confirmed by the mask matching value [
$\chi \left(\mathbf{c}^{ETM-CP}; \boldsymbol{\alpha}^{ETM-CP}, \boldsymbol{\beta}^{ETM-CP} \right) = 1.22 \times 10^{-9}$, Tab 4.1]. In order to validate
the $EM-$based proposed approaches, the "bare" $EM - ETM$ optimization has
been executed considering as reference excitations the optimal amplitudes coef-
ficients of Fig. 4.2(a). The evaluated cost function values have been reported in
Fig. 4.3(a) as compared to the $ETM-CP$ approach. However, as expected, none
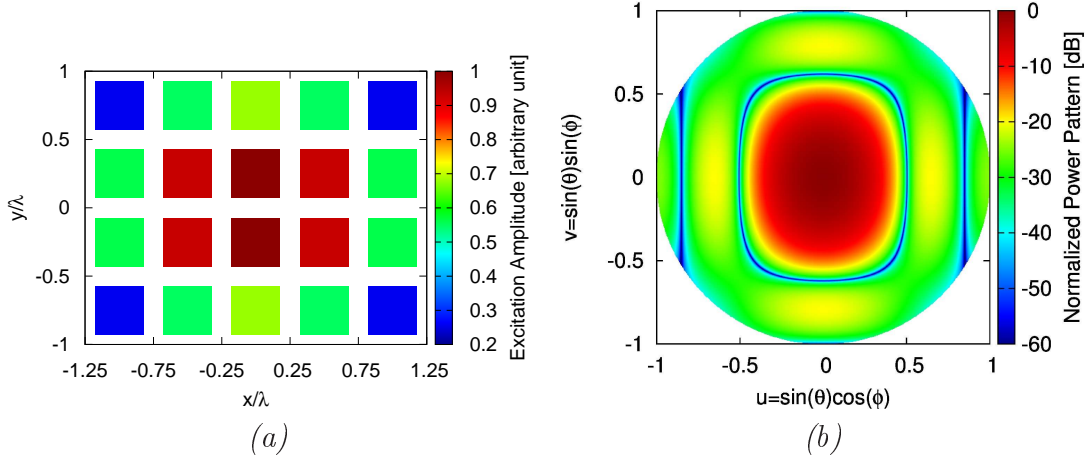
Figure 4.2: *Numerical Assessment (Small Array, Symmetric Mask; $d = 0.5\lambda$, $M \times N = 5 \times 4$ $N_{tot} = 20$, $T = 95$) - The reference solution of the fully-populated array obtained through a CP optimization. (a) The amplitude coefficients, and (b) the top-view power pattern.*

of the $EM - ETM$ solutions reach the fitness threshold, showing a non negligible distance of the $EM - ETM$ best solution from the global optimum reached by $ETM - CP$. Indeed, by observing Fig. 4.3(b)-(c) the power pattern cut along the azimuth and elevation planes of the $EM - ETM$ power pattern, considerably violates the power mask in both the principal planes cuts. Anyway, by observing the tiling/amplitudes configuration of the best $EM - ETM$ solution reported, in Fig, 4.4(c), the tiles arrangement is exactly the same of the $ETM - CP$ solution [Fig. 4.4(a)], while the sub-array amplitude coefficients shows different values. For this reason, the proposed $EM - ETM/CP$ approach, by a CP optimization of the tiles amplitudes [Fig. 4.4(e)], allows to exactly converge to the same $ETM - CP$ solution [Fig. 4.4(a)], accordingly the respective power patterns overlap [Fig. 4.3(b)-(c)]. It is worth noting here that the overall time needed to obtain the global optimal solution using the $EM - ETM/CP$ method has been estimated equal to $\Delta t^{EM-ETM/CP} = \Delta t^{ref} + \Delta t^{EM-ETM} + \Delta t^{CP} = 1 : 18$ [min:sec] (Tab 4.1), which means a time reduction of 99.7% with respect to the $ETM - CP$ approach. With the purpose of validating the $EM - OTM/CP$ strategy, the $GA-$based schemata-driven optimization, has been also executed. The GA control parameters have been set according to the rules described in Ch. 3 ($U = 6$, $K = 10$, $p_c = 0.9$, $p_m = 0.01$). For statistical reasons, the GA optimization has been executed for 10 different time converging to the $EM - ETM$ simulation [Fig. 4.3(b)-(c)], consequently the $EM - OTM/CP$ solution coincide to the $EM - ETM/CP$.

In order to quantify the robustness of the optimized tiled array, when the beam is steered off-broadside directions, the mask matching of the power pattern
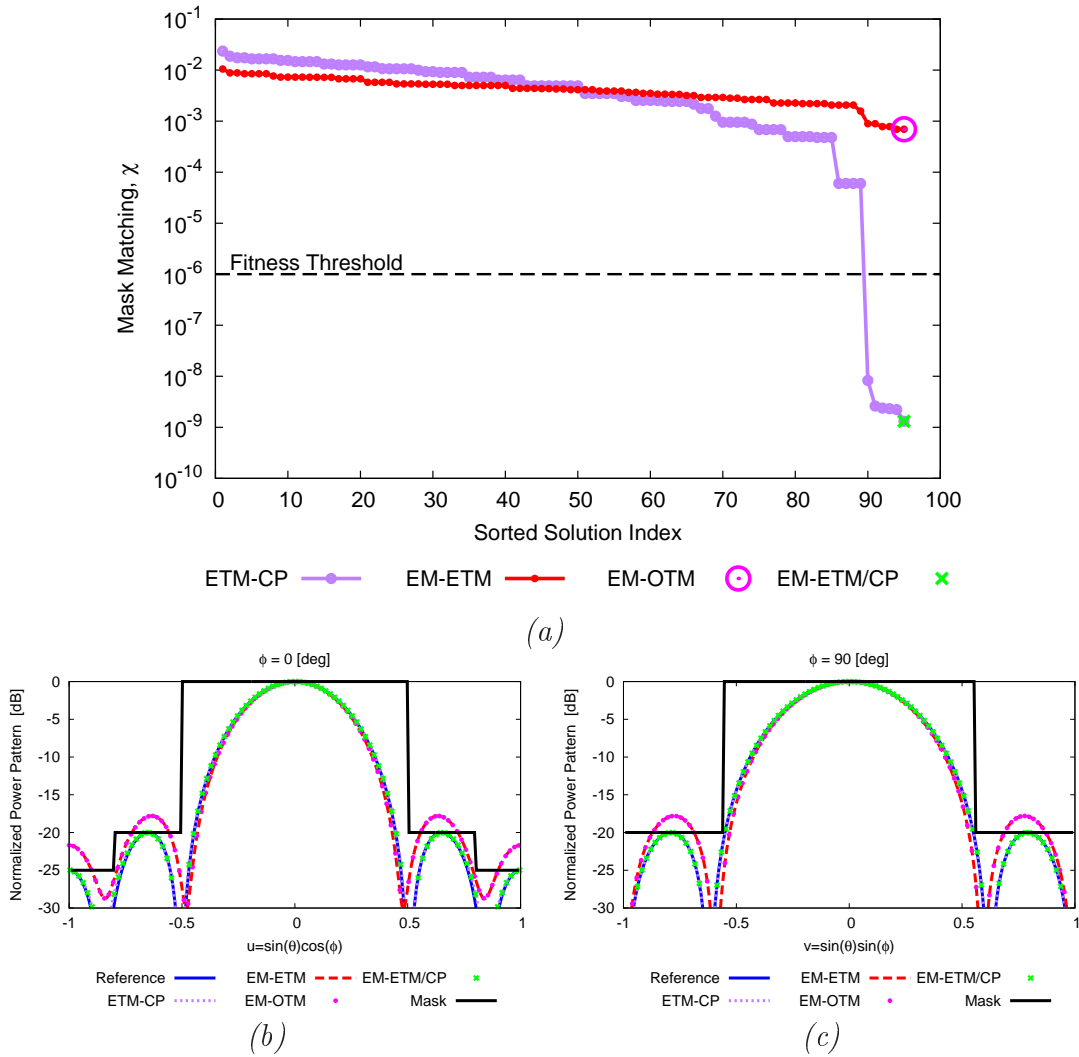
Figure 4.3: *Numerical Assessment (Small Array, Symmetric Mask*; $d = 0.5\lambda$, $M \times N = 5 \times 4$ $N_{tot} = 20$, $T = 95$) - (a) The $ETM - CP$ cost function evaluations for each of the $T = 95$ tiling solutions, as compared to the $EM - ETM$ simulation cost function evaluations, and the cost function of the $EM - ETM/CP$ simulation. $(b)(c)$ The power pattern cuts along the $u = u_0 = 0.0$ and $v = v_0 = 0.0$ plane of the $ETM - CP$, $EM - ETM$, $EM - OTM$ optimal solutions and the $EM - ETM/CP$ solution, as compared to the power mask.

59

Table 4.1: *Numerical Assessment (Small Array, Symmetric Mask*; $d = 0.5\lambda$, $M \times N = 5 \times 4$ $N_{tot} = 20$, $T = 95$) - Measured radiation indexes (SLL, D, $HPBW_{az}$, and $HPBW_{el}$), mask matching $\chi\left[P\left(u, v\right)\right]$ of the reference and optimized tilings patterns, and timings of the optimizations/simulations.

	SLL [dB]	D [dBi]	$HPBW_{az}$ [deg]	$HPBW_{el}$ [deg]	χ -	Δt [h:min:sec]
	$M \times N = 4 \times 5\ Symmetric\ Mask$					
Reference	-20.00	17.12	24.15	30.10	2.36×10^{-9}	$00:11:40$
$ETM - CP$	-20.00	16.95	24.21	30.10	1.22×10^{-9}	$09:44:30$
$EM - ETM$	-17.80	17.20	23.49	29.29	6.94×10^{-4}	$00:00:31$
$EM - OTM$	-17.80	17.20	23.49	29.29	6.94×10^{-4}	$00:00:05$
$EM - ETM/CP$	-20.00	16.95	24.21	30.10	1.22×10^{-9}	$00:00:47$

varying the beam pointing within the visible range (i.e. $0° \leq \theta_0 < 90°$ and $0° \leq \phi_0 < 360°$), has been evaluated and reported in the polar diagram of Fig. 4.5(a). It can be noticed that the steering of the beam along the $\phi_0 = 90$[deg] direction, leads to higher mask matching values for lower θ_0 angles with respect to when steering along the azimuth plane. A detail of the steering analysis is reported in Fig. 4.5(b) showing the mask matching as function of the pointing angle θ_0 along the $\phi_0 = 0$ [deg] and $\phi_0 = 90$ [deg] planes, showing a maximum off-boresight steering angle of $\theta_0 < 1$ [deg] along the $\phi_0 = 90$ [deg] plane, and $\theta_0 < 2$ [deg] along the $\phi_0 = 0$ [deg] plane. The steering of the beam in Fig. 4.5(a)-(b) has been obtained by a simple linear phase shift, using the analytic formula (3.11). Hence the reported results can be further improved by performing a CP synthesis of the steered power pattern, considering the steered mask.

In order to show the versatility of the proposed methodologies, an asymmetric power mask (Fig. 4.6) has been considered for a second assessment of the $M \times N = 4 \times 5$ array. This time both the amplitudes and phase coefficients are optimized, and the reference ideal optimal CP amplitude and phase coefficients are shown in Fig. 4.7(a) and Fig. 4.7(b) respectively, together with the synthesized reference power pattern in Fig. 4.7(c). Also in this case the $ETM - CP$ approach has been executed in order to find the optimal tiled array fitting $M\left(u, v\right)$. Two solutions reached the fitness threshold [Fig. 4.8(a)], with a final cost-function value of the global best equal to $\chi\left(\mathbf{c}^{ETM-CP}; \boldsymbol{\alpha}^{ETM-CP}, \boldsymbol{\beta}^{ETM-CP}\right) = 1.04 \times 10^{-8}$ (Tab. 4.2). The amplitude and phases coefficients, as well as the tiling configuration, have been reported in Fig. 4.9(a)-(b), together with the top view of the power pattern [Fig. 4.9(c)]. Even in this case the $EM - ETM$ and the $EM - OTM$ methods converge to the same $EM-$optimal solution [Fig. 4.8(a)], but still too far from an acceptable matching [$\chi\left(\mathbf{c}^{EM-ETM}; \boldsymbol{\alpha}^{EM-ETM}, \boldsymbol{\beta}^{EM-ETM}\right) = 8.03 \times 10^{-4}$, Tab. 4.2].
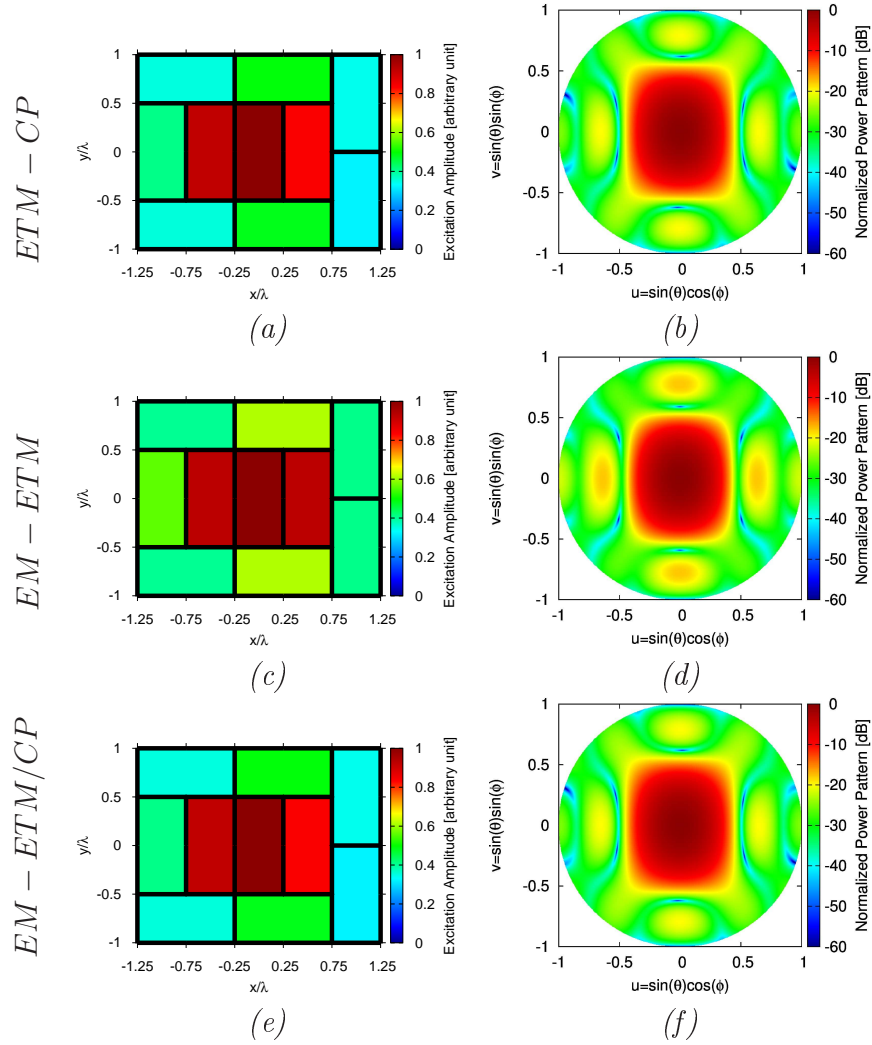
Figure 4.4: *Numerical Assessment (Small Array, Symmetric Mask*; $d = 0.5\lambda$, $M \times N = 5 \times 4$ $N_{tot} = 20$, $T = 95$) - $(a)(c)(e)$ The tiles amplitudes excitations coefficients and $(b)(d)(f)$ the respective top-view power patterns of the $ETM - CP$ optimal solution $(a)(b)$, the $EM - ETM$ optimal solution $(c)(d)$, and the $EM - ETM/CP$ solution $(e)(f)$.

(a)   *(b)*
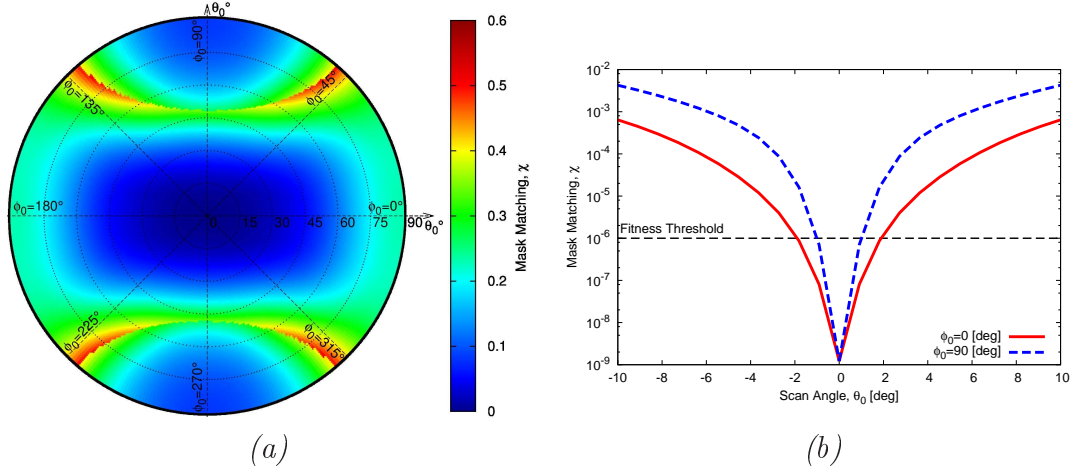
Figure 4.5: *Numerical Assessment (Small Array, Symmetric Mask*; $d = 0.5\lambda$, $M \times N = 5 \times 4$ $N_{tot} = 20$, $T = 95$) - The mask matching map, evaluated when steering the beam of the $EM - ETM/CP$ solution, within a scan cone.

It can be noticed that the tiles orientation of the solution reached by the "bare" $EM-$based methods [Fig. 4.9(d)], is slightly different from the $ETM - CP$ tiling [Fig. 4.9(a)], consequently, in this case there are no chances to converge to the global optimum through the $EM - ETM/CP$. Nevertheless, differently from the $EM - ETM$, the $EM - ETM/CP$ solution lowers the mask matching down to $\chi\left(\mathbf{c}^{EM-ETM}; \boldsymbol{\alpha}^{EM-ETM/CP}, \boldsymbol{\beta}^{EM-ETM/CP}\right) = 2.05 \times 10^{-5}$(Tab. 4.2), and, even if the cost function is above the fitness threshold, the power pattern it's very close to the reference power mask profile and to the optimal $ETM - CP$ pattern [Fig. 4.8(b)-(c)], also confirmed by the pattern descriptors reported in Tab. 4.2 ($\Delta SLL = \left|SLL^{EM-ETM/CP} - SLL^{ref}\right| = 0.41$ [dB], $\Delta D = \left|D^{EM/ETM-CP} - D^{ref}\right| = 0.28$ [dBi], $\Delta HPBW_{AZ} = \left|HPBW_{AZ}^{EM-ETM/CP} - HPBW_{AZ}^{ref}\right| = 0.55$ [deg], $\Delta HPBW_{EL} = \left|HPBW_{EL}^{EM-ETM/CP} - HPBW_{EL}^{Rref}\right| = 0.21$ [deg]). Moreover, the $EM - ETM/CP$ method allows to reach the closest solution to the optimum in a reduced amount of time, which is equal to $\Delta t^{EM-ETM/CP} = \Delta t^{ref} + \Delta t^{EM-ETM} + \Delta t^{CP} = 00 : 16 : 18$ [h:min:sec], instead of $\Delta t^{ETM-CP} = 16 : 43 : 10$ [h:min:sec] for the full $ETM - CP$ simulation. Finally, the analysis varying the scanning angle has been performed for the optimal and compromise solutions. As can be seen from Fig. 4.10(a)(c) the $ETM - CP$ solution is more robust when steering the beam along the azimuth plane, while the $EM - ETM/CP$ tiling allows better performances along the elevation plane [Fig. 4.10(b)-(d)].

62
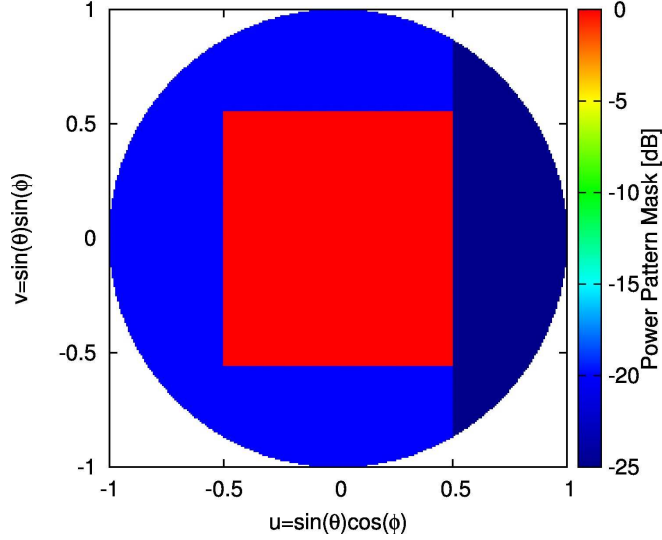
Figure 4.6: *Numerical Assessment (Small Array, Asymmetric Mask*; $d = 0.5\lambda$, $M \times N = 5 \times 4$ $N_{tot} = 20$, $T = 95$) - The power mask $M(u,v)$ defining the constraints for the synthesis of an $M \times N = 5 \times 4$ array of isotropic elements.

Table 4.2: *Numerical Assessment (Small Array, Asymmetric Mask*; $d = 0.5\lambda$, $M \times N = 5 \times 4$ $N_{tot} = 20$, $T = 95$) - Measured radiation indexes (SLL, D, $HPBW_{az}$, and $HPBW_{el}$), mask matching $\chi[P(u,v)]$ of the reference and optimized tilings patterns, and timings of the optimizations/simulations.

	SLL [dB]	D [dBi]	$HPBW_{az}$ [deg]	$HPBW_{el}$ [deg]	χ -	Δt [h:min:sec]
	$M \times N = 4 \times 5$ *Asymmetric Mask*					
Reference	-20.00	16.96	24.70	30.08	4.60×10^{-10}	$00:11:50$
$ETM - CP$	-20.00	16.81	24.95	30.08	1.04×10^{-7}	$16:43:10$
$EM - ETM$	-17.14	17.04	24.10	29.57	8.03×10^{-4}	$00:00:30$
$EM - OTM$	-17.14	17.04	24.10	29.57	8.03×10^{-4}	$00:00:09$
$EM - ETM/CP$	-19.59	16.68	25.25	30.29	2.05×10^{-5}	$00:03:58$
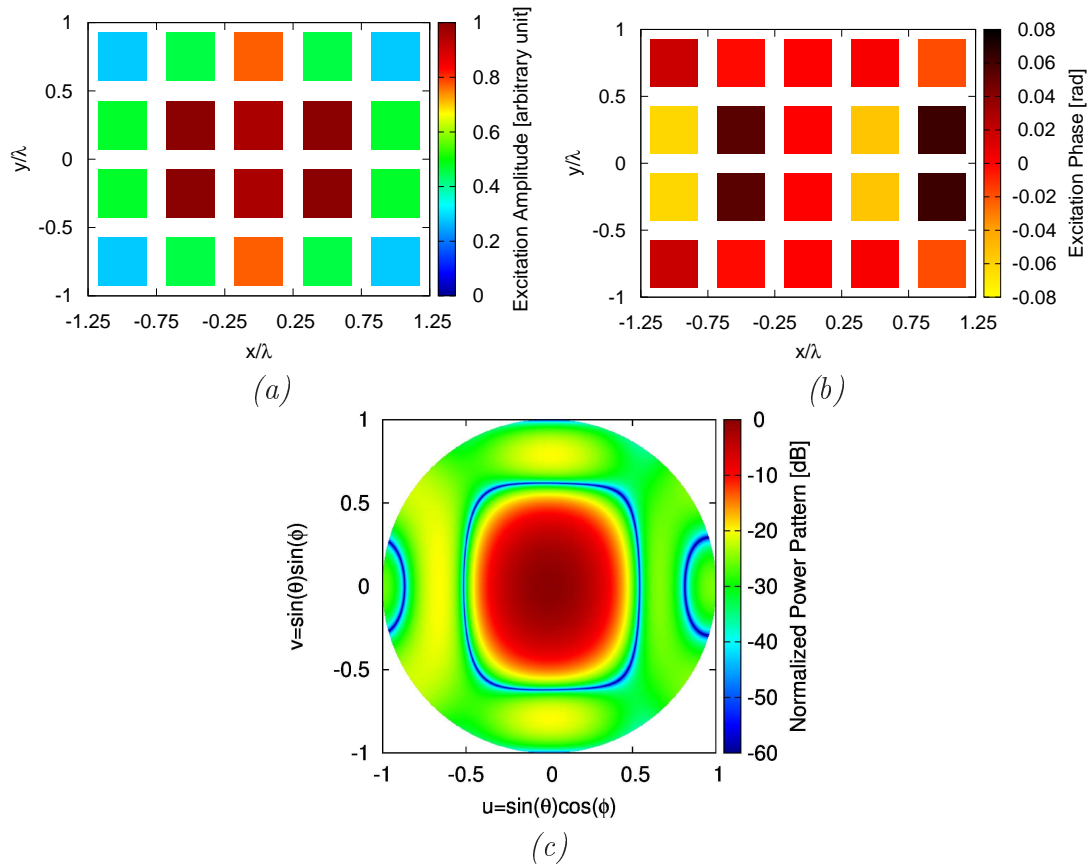
Figure 4.7: *Numerical Assessment (Small Array, Asymmetric Mask*; $d = 0.5\lambda$, $M \times N = 5 \times 4$ $N_{tot} = 20$, $T = 95$) - The reference solution of the fully-populated array obtained through a CP optimization. (a) The amplitude coefficients, (b) the phase coefficients, and (c) the top-view power pattern.
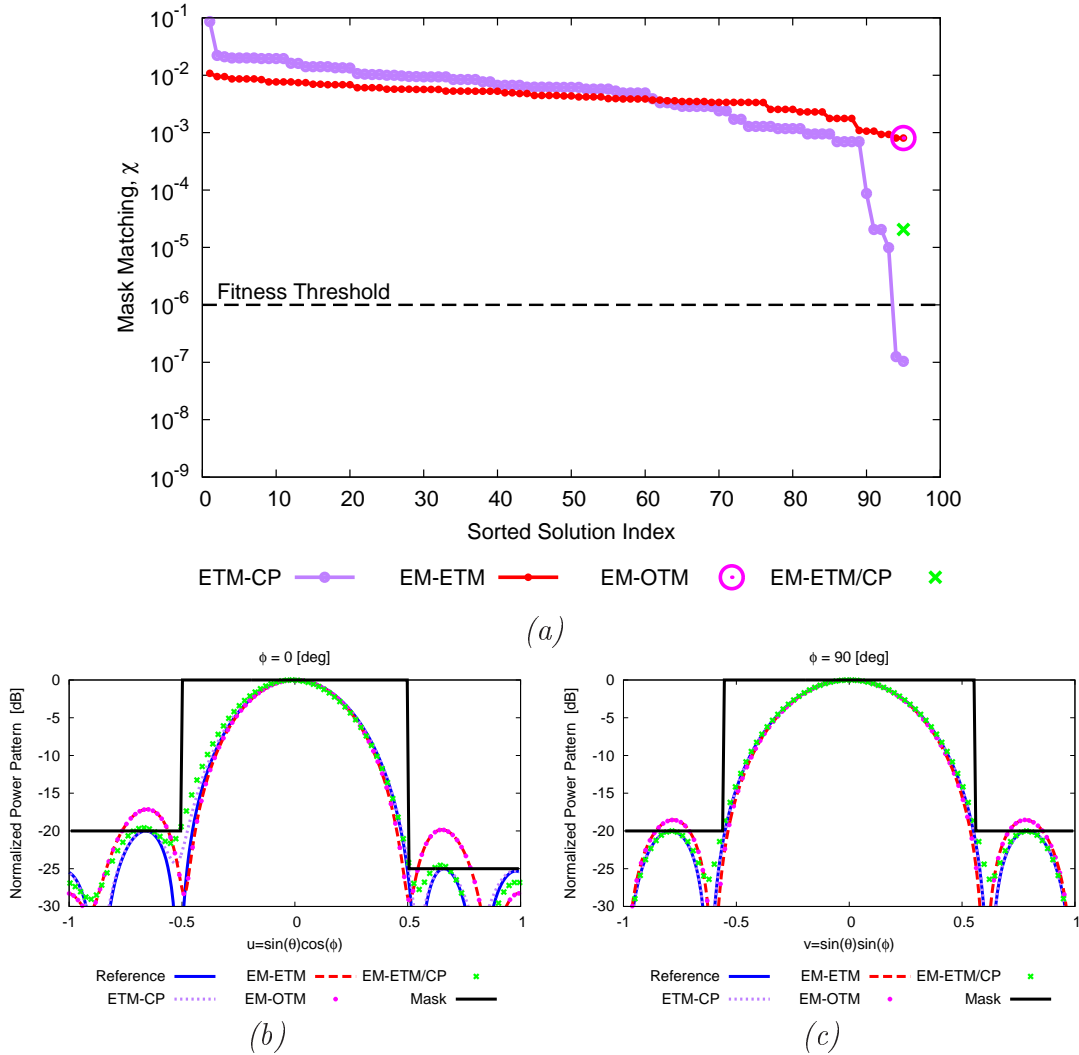
Figure 4.8: *Numerical Assessment (Small Array, Asymmetric Mask*; $d = 0.5\lambda$, $M \times N = 5 \times 4$ $N_{tot} = 20$, $T = 95$) - (a) The $ETM - CP$ cost function evaluations for each of the $T = 95$ tiling solutions, as compared to the $EM - ETM$ simulation cost function evaluations, and the cost function of the $EM - ETM/CP$ simulation, together with the full-wave results. (b)(c) The power pattern cuts along the $u = u_0 = 0.0$ and $v = v_0 = 0.0$ plane of the $ETM - CP$, $EM - ETM$, $EM - OTM$ optimal solutions and the $EM - ETM/CP$ solution, as compared to the power mask.
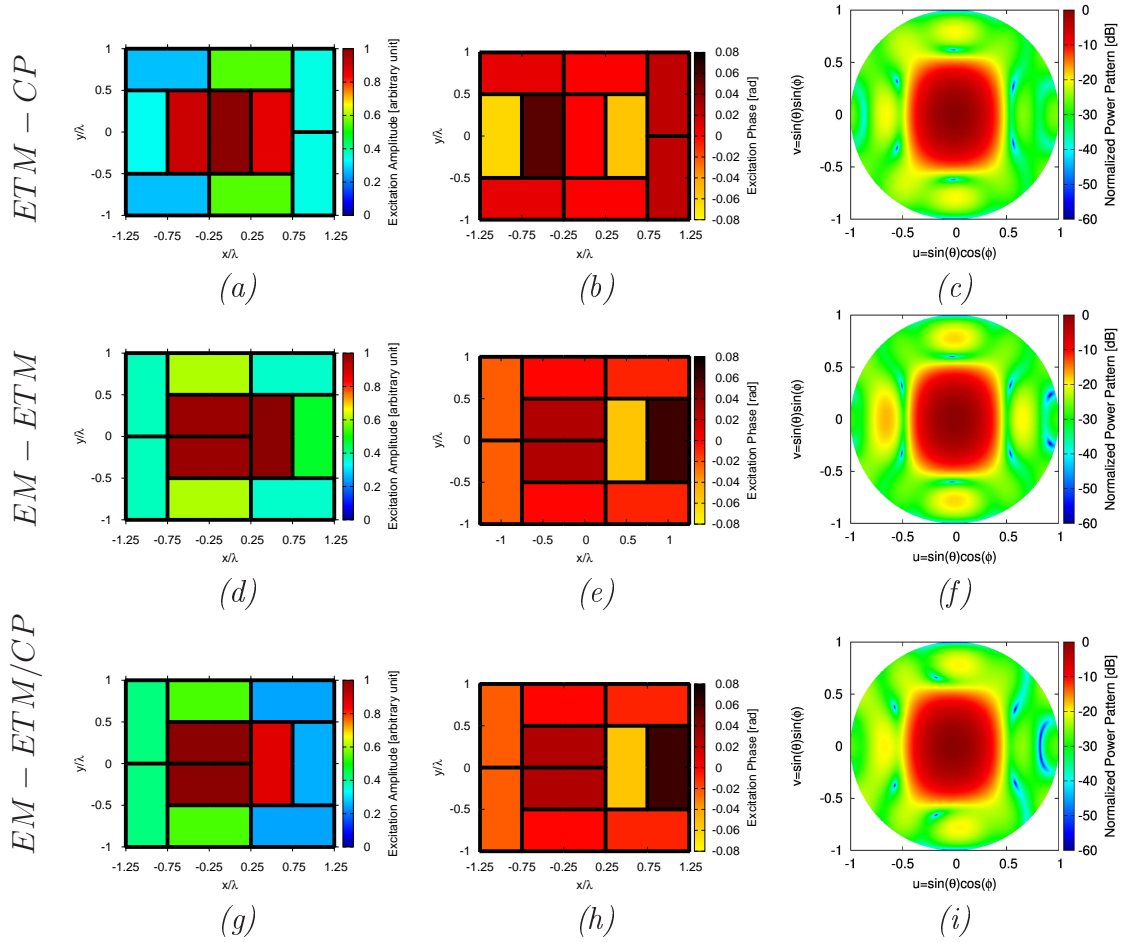
Figure 4.9: *Numerical Assessment (Small Array, Asymmetric Mask*; $d = 0.5\lambda$, $M \times N = 5 \times 4$ $N_{tot} = 20$, $T = 95$) - $(a)(d)(g)$ The tiles amplitudes excitations coefficients, $(b)(e)(h)$ the tiles phases excitations coefficients and $(c)(f)(i)$ the respective top-view power patterns of the $ETM - CP$ optimal solution $(a)(b)(c)$, the $EM - ETM$ optimal solution $(d)(e)(f)$, the $EM - ETM/CP$ solution $(g)(h)(i)$.

(a)   *(b)*

(c)   *(d)*
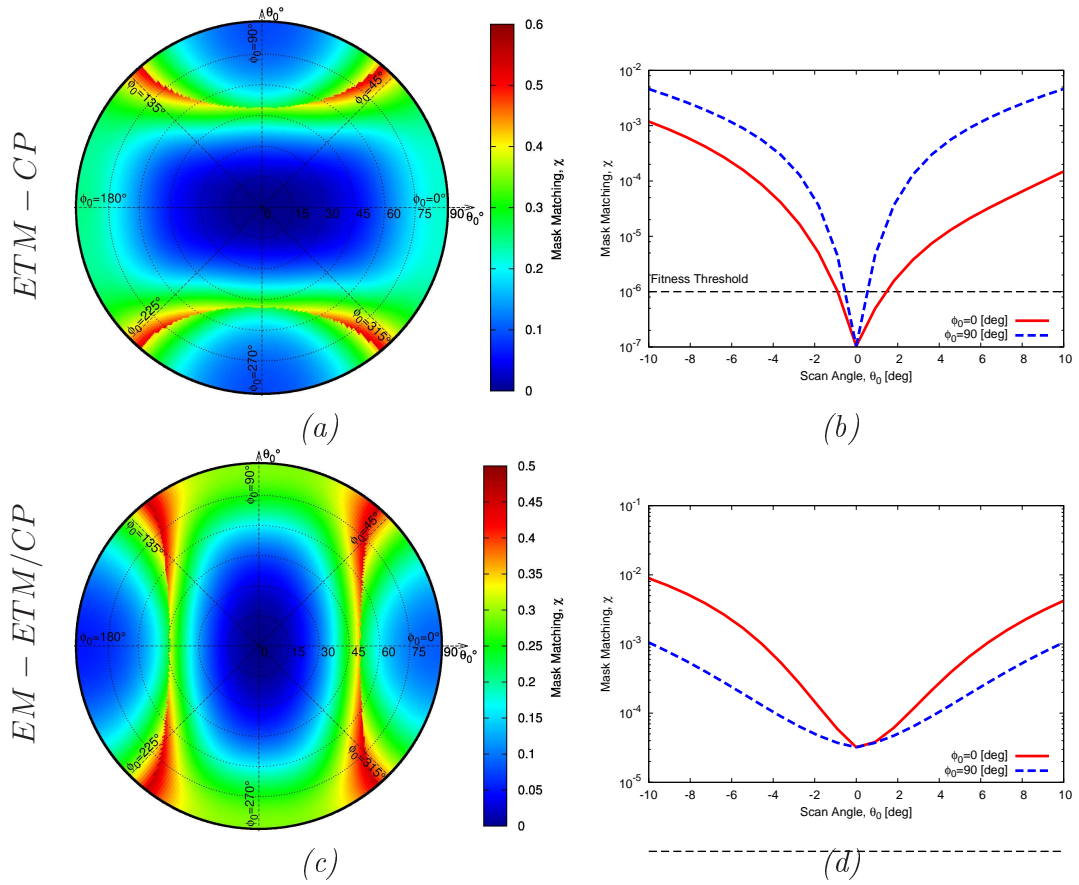
Figure 4.10: *Numerical Assessment (Small Array, Asymmetric Mask*; $d = 0.5\lambda$,
$M \times N = 5 \times 4$ $N_{tot} = 20$, $T = 95$*) - The mask matching map, evaluated when
steering the beam of the $EM - ETM/CP$ solution, within a scan cone.*

67

4.4.2 Medium Dimensions Arrays

In order to asses the proposed methodology for small/medium sized arrays, an $4.5\lambda \times 3\lambda$ rectangular aperture is now considered, filled with $N \times M = 9 \times 6$ elements located over a squared lattice and equally spaced by $d_x = d_y = \lambda/2$. The symmetric power mask of Fig. 4.11 defines the optimal pattern shape, consisting in a main beam window of dimension $BW_u \times BW_v = 0.5\,[u] \times 0.8\,[v]$, a maximum $SLL_{L1} = -20$ [dB] for the lobes nearby the main lobe, and a maximum $SLL_{L2} = -25$ [dB] in the end-fire zone. The CP optimized amplitude coefficients of the reference fully-populated array, together with the synthesized power pattern are reported in Fig. 4.13. According to (3.4) a $M \times N = 9 \times 6$ elements array can be partitioned into exactly $T = 8.17991 \times 10^5$ different tilings. It is clear that in this case the amount of time needed to complete an $ETM-CP$ simulations turns out to be very large (i.e $\Delta t \simeq 94$ days, assuming $\Delta t^{CP} \simeq 10$ [sec]). The $EM-$based techniques instead, allow to complete the optimization into a reasonable amount of time (i.e.$\Delta t^{EM-ETM} = 15 : 39 : 36$ [h:min:sec] and $\Delta t^{EM-OTM} = 00 : 20 : 12$ [h:min:sec], Tab. 4.3). The mask matching evaluated by the $EM-ETM$ for all the existing tilings has been reported in Fig. 4.13(a), together with the best solution provided by the $EM-OTM$ approach. It is worth noting that also in this case the $EM-OTM$ method (the following parameters have been used for the 10 GA optimizations: $U = 54$, $K = 500$, $p_c = 0.9$, $p_m = 0.01$), achieve the same $EM-ETM$ solution. Figure 4.14(a) reports the tiling, as well as the amplitude coefficients of the $EM-ETM/OTM$ solution, while the top-view power pattern is shown in Fig. 4.14(b). The comparison of the power pattern with the power mask is reported in Fig. 4.13(b)-(c) along the azimuth and elevation planes, respectively. As can be seen the power pattern corresponding to the $EM-ETM$ solution, does not match the optimal performances $[\chi\left(\mathbf{c}^{EM-ETM}; \boldsymbol{\alpha}^{EM-ETM}, \boldsymbol{\beta}^{EM-ETM}\right) = 4.8 \times 10^{-5}$, Tab. 4.3]. Nevertheless, the solution obtained through the proposed $EM-ETM/CP$ method [Fig. 4.9(c)-(d)] affords a power pattern that completely fits the power mask, as confirmed by the final cost function value $[\chi\left(\mathbf{c}^{EM-ETM}; \boldsymbol{\alpha}^{EM-ETM/CP}, \boldsymbol{\beta}^{EM-ETM/CP}\right) = 5.0 \times 10^{-10}$ Tab. 4.3], which is below the fitness threshold [Fig. 4.13(a)]. The analysis of the mask matching varying the scanning angle has been executed and graphically shown in the diagram of Fig. 4.15(a). Moreover, Fig. 4.15(b) reports the mask matching parameter when steering the beam along the $\phi_0 = 0$ [deg] and $\phi_0 = 90$ [deg] planes, showing a maximum scan angle of $\theta_0 = 2$ [deg], if a good matching with the power mask must be assured.

A second assessment of the 9×6 array has been performed considering the power mask of Fig. 4.16. A window of dimension $BW_u \times BW_v = 0.64\,[u] \times 0.92\,[v]$ is considered for the main beam, while three different SLL levels are asymmetrically defined in the side-lobes zone: $SLL_{L1} = -25$ [dB], $SLL_{L2} = -28$ [dB], and $SLL_{L3} = -35$ [dB]. The reference complex excitations of the fully populated array is reported in Fig. 4.17(a)-(b), and the corresponding power pattern in Fig. 4.17(c). As shown in Fig. 4.18(a), the $EM-ETM$ and
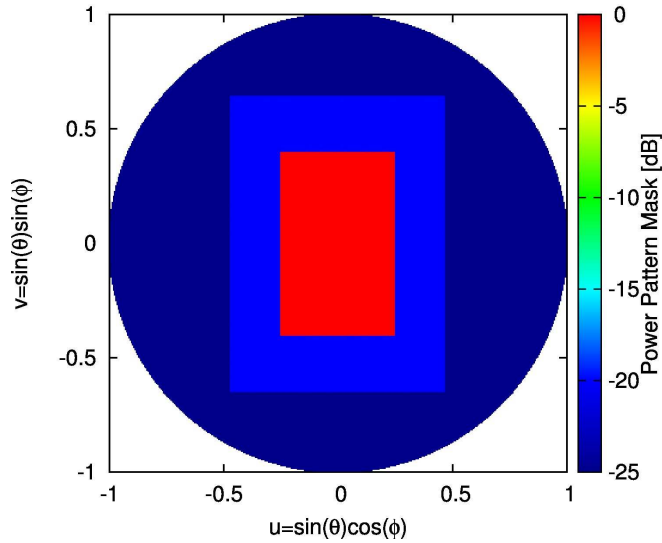
Figure 4.11: *Numerical Assessment (Medium Array, Symmetric Mask; $d = 0.5\lambda$,
$M \times N = 6 \times 9$ $N_{tot} = 54$, $T \simeq 8.2 \times 10^5$) - The power mask $M(u, v)$ defining the
constraints for the synthesis of an $M \times N = 6 \times 9$ array of isotropic elements.*

(a) (b)
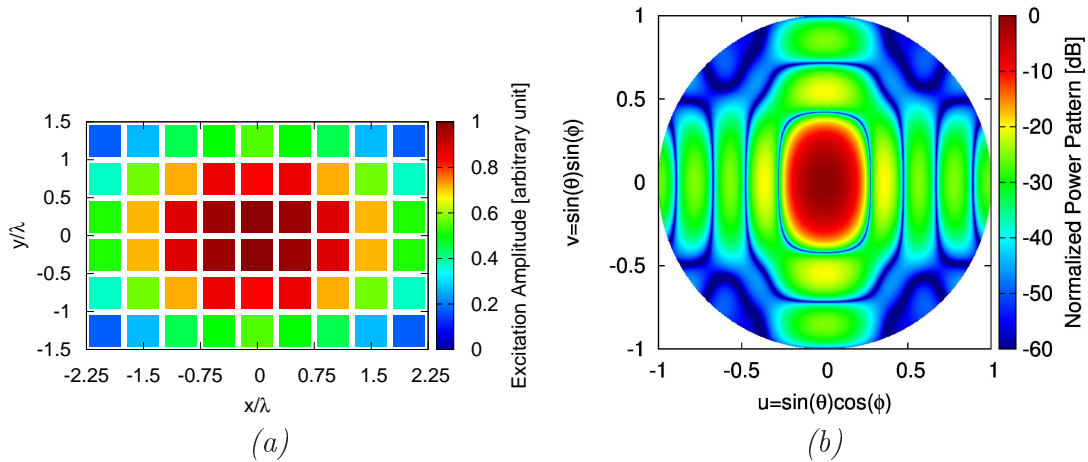
Figure 4.12: *Numerical Assessment (Medium Array, Symmetric Mask; $d = 0.5\lambda$,
$M \times N = 6 \times 9$ $N_{tot} = 54$, $T \simeq 8.2 \times 10^5$) - The reference solution of the
fully-populated array obtained through a CP optimization. (a) The amplitude
coefficients, and (b) the top-view power pattern.*

(a)

(b)   *(c)*
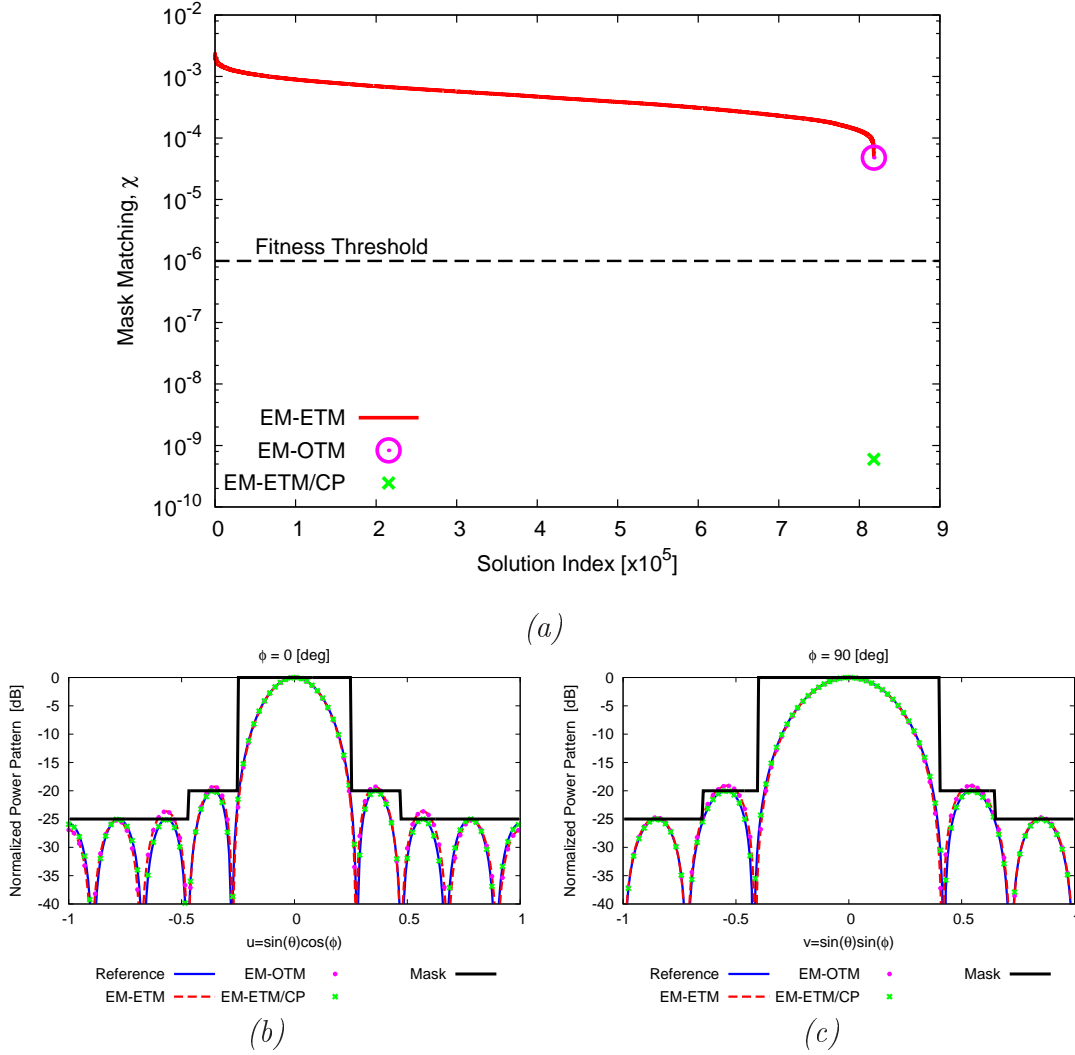
Figure 4.13: *Numerical Assessment (Medium Array, Symmetric Mask*; $d = 0.5\lambda$, $M \times N = 6 \times 9$ $N_{tot} = 54$, $T \simeq 8.2 \times 10^{5}$) - ($a$) The $EM - ETM$, $EM - OTM$ simulation cost function evaluations, and the cost function of the $EM - ETM/CP$ simulation. (b)-(c) The power pattern cuts along the $u = u_0 = 0.0$ and $v = v_0 = 0.0$ plane of the $ETM - EM$, $EM - OTM$ optimal solution and the $EM - ETM/CP$ solution, as compared to the reference fully-populated solution and to the power mask.

(a)   *(b)*

(c)   *(d)*
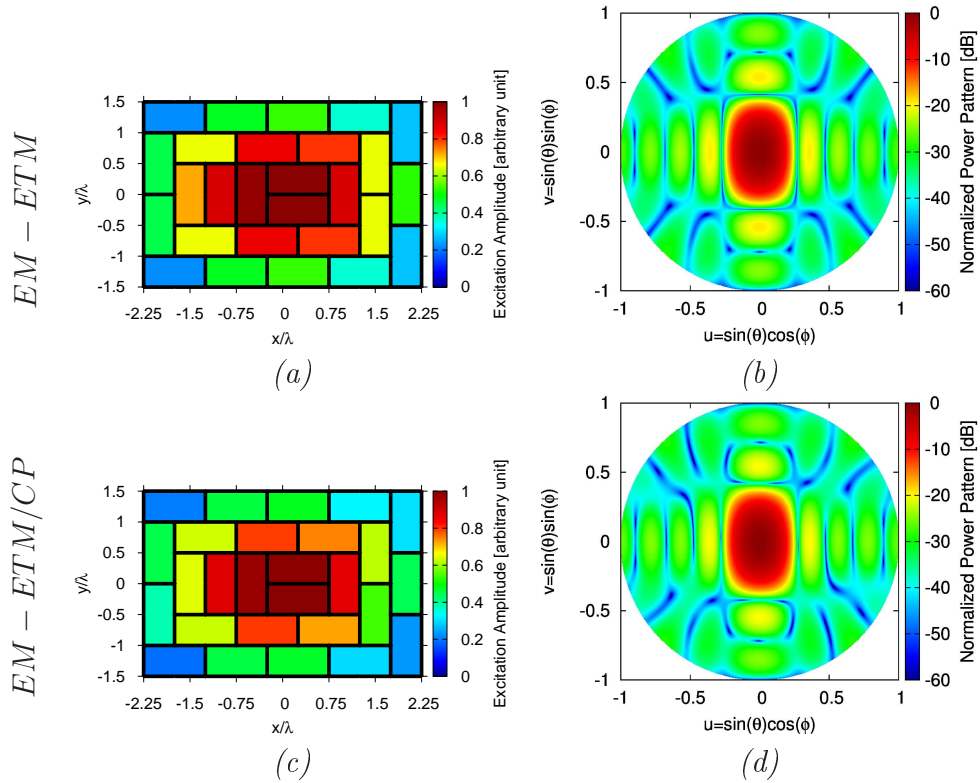
Figure 4.14: *Numerical Assessment (Medium Array, Symmetric Mask*; $d = 0.5\lambda$, $M \times N = 6 \times 9 \; N_{tot} = 54$, $T \simeq 8.2 \times 10^5$*)* - $(a)(c)$ The tiles amplitudes excitations coefficients and $(b)(d)$ the respective top-view power patterns of the the $EM - ETM$ optimal solution (a)(b), and the $EM - ETM/CP$ solution $(c)(d)$.

(a)   *(b)*
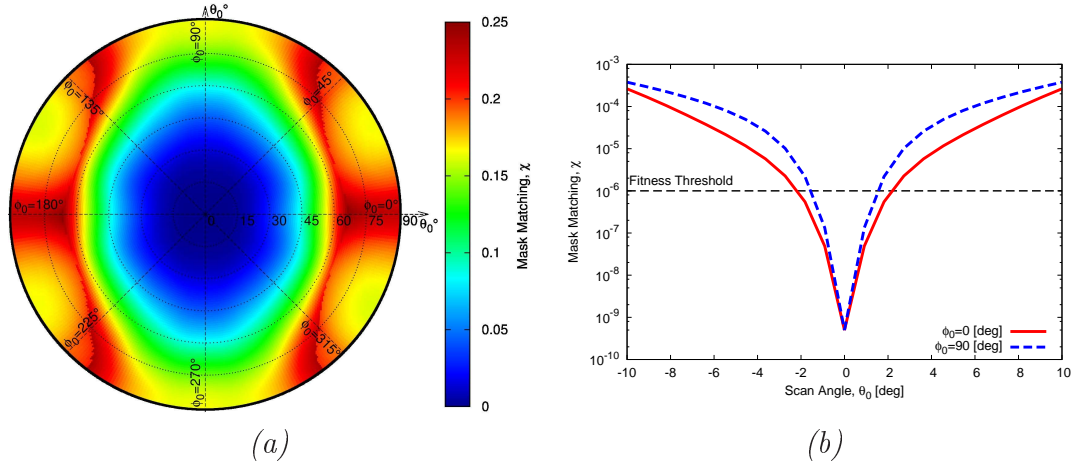
Figure 4.15: *Numerical Assessment (Medium Array, Symmetric Mask*; $d = 0.5\lambda$, $M \times N = 6 \times 9 \; N_{tot} = 54$, $T \simeq 8.2 \times 10^5$*)* - The mask matching map, evaluated when steering the beam of the $EM - ETM/CP$ solution, within a scan cone.

71

Table 4.3: *Numerical Assessment (Medium Array, Symmetric Mask*; $d = 0.5\lambda$, $M \times N = 6 \times 9$ $N_{tot} = 54$, $T \simeq 8.2 \times 10^5$) - Measured radiation indexes (SLL, D, $HPBW_{az}$, and $HPBW_{el}$), mask matching $\chi[P(u,v)]$ of the reference and optimized tilings patterns, and timings of the optimizations/simulations.

	SLL [dB]	D [dBi]	$HPBW_{az}$ [deg]	$HPBW_{el}$ [deg]	$\chi[P(u,v)]$ -	Δt [h:min:sec]
	$M \times N = 6 \times 9\ Symmetric\ Mask$					
Reference	-20.00	21.52	13.15	20.07	3.60×10^{-10}	$00:21:25$
$EM - ETM$	-19.11	21.54	13.03	19.86	4.80×10^{-5}	$15:39:36$
$EM - OTM$	-19.11	21.54	13.03	19.86	4.80×10^{-5}	$00:20:12$
$EM - ETM/CP$	-20.00	21.46	13.15	20.07	5.00×10^{-10}	$00:03:30$

$EM - OTM$ simulations converges to the same $EM-$optimal solution showing a mask matching equal to $\chi\left(\mathbf{c}^{EM-ETM}; \boldsymbol{\alpha}^{EM-ETM}, \boldsymbol{\beta}^{EM-ETM}\right) = 2.4 \times 10^{-4}$ (Tab. 4.4), whose corresponding tiling is pictured in Fig. 4.19(a)-(b), together with the $EM - ETM$ amplitude and phase coefficients, while the top view power pattern is reported in Fig. 4.19(c). The $EM - ETM/CP$ optimization still does not reach the convergence, consequently the cost function value $[\chi\left(\mathbf{c}^{EM-ETM}; \boldsymbol{\alpha}^{EM-ETM/CP}, \boldsymbol{\beta}^{EM-ETM/CP}\right) = 1.7 \times 10^{-5}$ Tab 4.4] is still above the fitness threshold [Fig. 4.18(a)], but its lower with respect to the $EM - ETM$ solution. Indeed, even if the $EM - ETM/CP$ power pattern violates the power mask [Fig. 4.18(b)-(c)], the corresponding beam pattern descriptors (Tab. 4.4) are very close to the optimal ones ($\Delta SLL = \left|SLL^{EM-ETM/CP} - SLL^{ref}\right| = 0.55$ [dB], $\Delta D = \left|D^{EM-ETM/CP} - D^{ref}\right| = 0.18$ [dBi], $\Delta HPBW_{AZ} = \left|HPBW_{AZ}^{EM-ETM/CP} - HPBW_{AZ}^{ref}\right| = 0.16$ [deg], $\Delta HPBW_{EL} = \left|HPBW_{EL}^{EM-ETM/CP} - HPBW_{EL}^{ref}\right| = 0.12$ [deg]). The analysis of the robustness against the beam steering [Fig. 4.20] shows a better performance of the $EM - ETM/CP$ along the elevation plane with respect to the azimuth plane.

4.4.3 Large Dimensions Arrays

As a final example, a larger array is considered. The array aperture is a rectangle of dimension $10\lambda \times 7.5\lambda$ filled by $N_{tot} = 300$ elements located over a 20×15 grid, equally spaced by $d_x = d_y = \lambda/2$. The considered power mask is shown in Fig. 4.21, as can bee seen, the mask is asymmetric with a main beam window of dimension $BW_u \times BW_v = 0.32\,[u] \times 0.42\,[v]$ and SLL levels equal to: $SLL_{L1} = -25$ [dB], $SLL_{L2} = -30$ [dB], and $SLL_{L3} = -40$ [dB]. Figure 4.22(a)-(b) shows the optimal CP excitation coefficients of the reference fully-populated array, and Fig. 4.22(b) shows the top-view of the synthe-
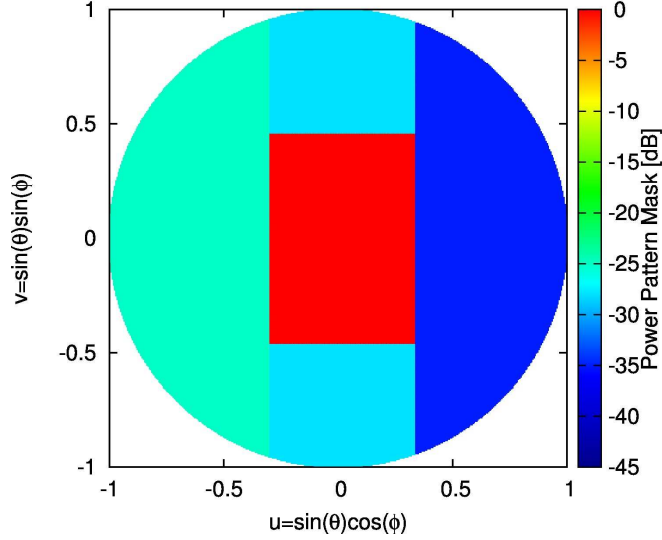
Figure 4.16: *Numerical Assessment (Medium Array, Asymmetric Mask; $d = 0.5\lambda$, $M \times N = 6 \times 9$ $N_{tot} = 54$, $T \simeq 8.2 \times 10^5$) - The power mask $M(u, v)$ defining the constraints for the synthesis of an $M \times N = 6 \times 9$ array of isotropic elements.*

Table 4.4: *Numerical Assessment (Medium Array, Asymmetric Mask; $d = 0.5\lambda$, $M \times N = 6 \times 9$ $N_{tot} = 54$, $T \simeq 8.2 \times 10^5$) - Measured radiation indexes (SLL, D, $HPBW_{az}$, and $HPBW_{el}$), mask matching $\chi[P(u, v)]$ of the reference and optimized tilings patterns, and timings of the optimizations.*

	SLL [dB]	D [dBi]	$HPBW_{az}$ [deg]	$HPBW_{el}$ [deg]	χ -	Δt [h:min:sec]
	$M \times N = 6 \times 9$ *Asymmetric Mask*					
Reference	-25.00	20.81	14.53	21.61	3.05×10^{-10}	$00:27:35$
$EM - ETM$	-23.48	20.85	14.32	21.33	2.40×10^{-4}	$16:08:10$
$EM - OTM$	-23.48	20.85	14.32	21.33	2.40×10^{-4}	$00:25:20$
$EM - ETM/CP$	-24.45	20.63	14.69	21.49	1.70×10^{-5}	$01:47:46$
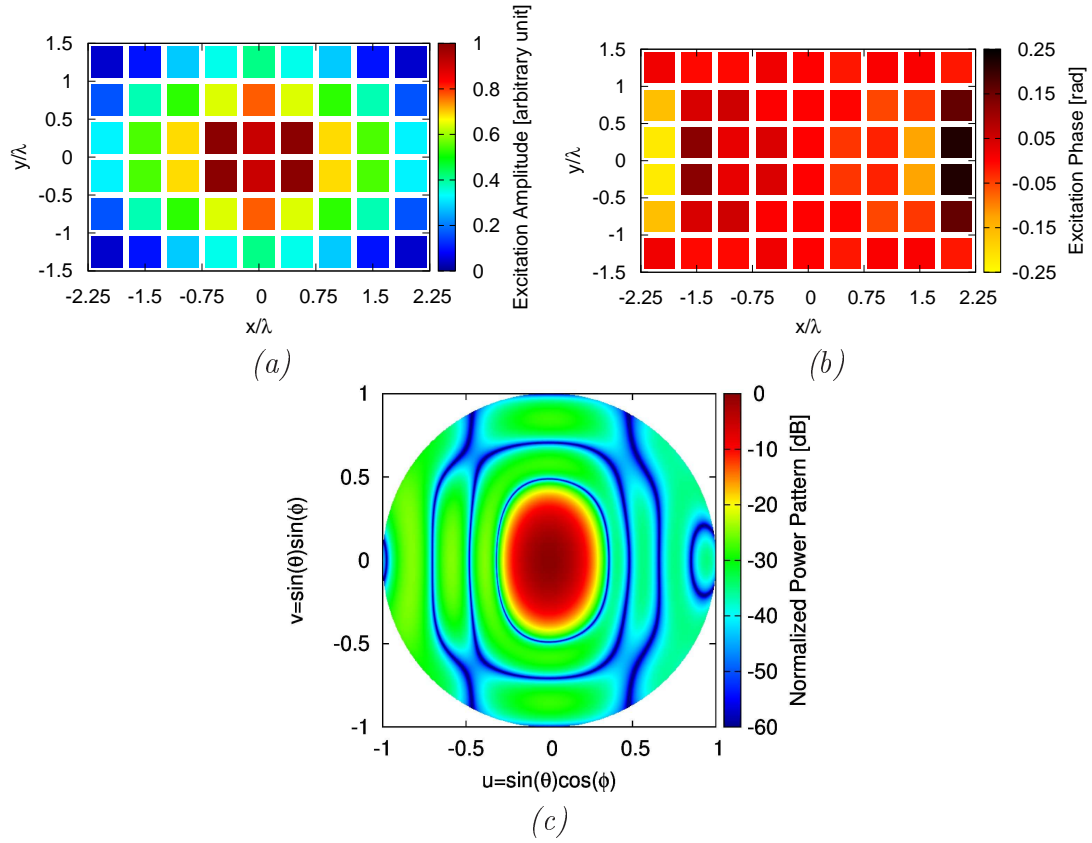
Figure 4.17: *Numerical Assessment (Medium Array, Asymmetric Mask; $d = 0.5\lambda$, $M \times N = 6 \times 9$ $N_{tot} = 54$, $T \simeq 8.2 \times 10^5$)* - The reference solution of the fully-populated array obtained through a CP optimization. (a) The amplitude coefficients, (b) the phase coefficients, and (c) the top-view power pattern.
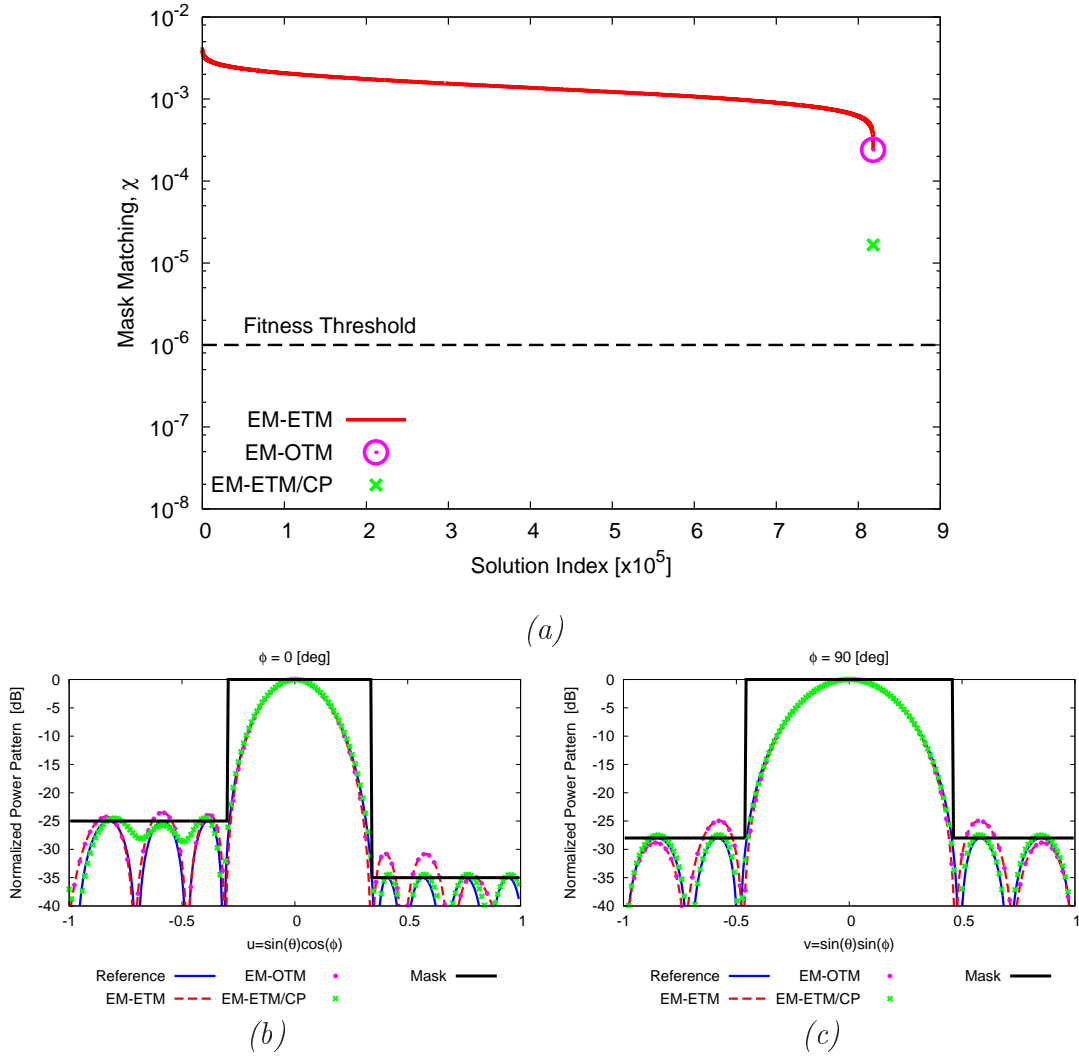
Figure 4.18: *Numerical Assessment (Medium Array, Asymmetric Mask*; $d =$
0.5λ, $M \times N = 6 \times 9$ $N_{tot} = 54$, $T \simeq 8.2 \times 10^5$*)* - (*a*) The $EM - ETM$,
$EM - OTM$ simulation cost function evaluations, and the cost function of the
$EM - ETM/CP$ simulation. (*b*)-(*c*) The power pattern cuts along the $u = u_0 =$
0.0 and $v = v_0 = 0.0$ plane of the $ETM - EM$, $EM - OTM$ optimal solution
and the $EM - ETM/CP$ solution, as compared to the reference fully-populated
solution and to the power mask.
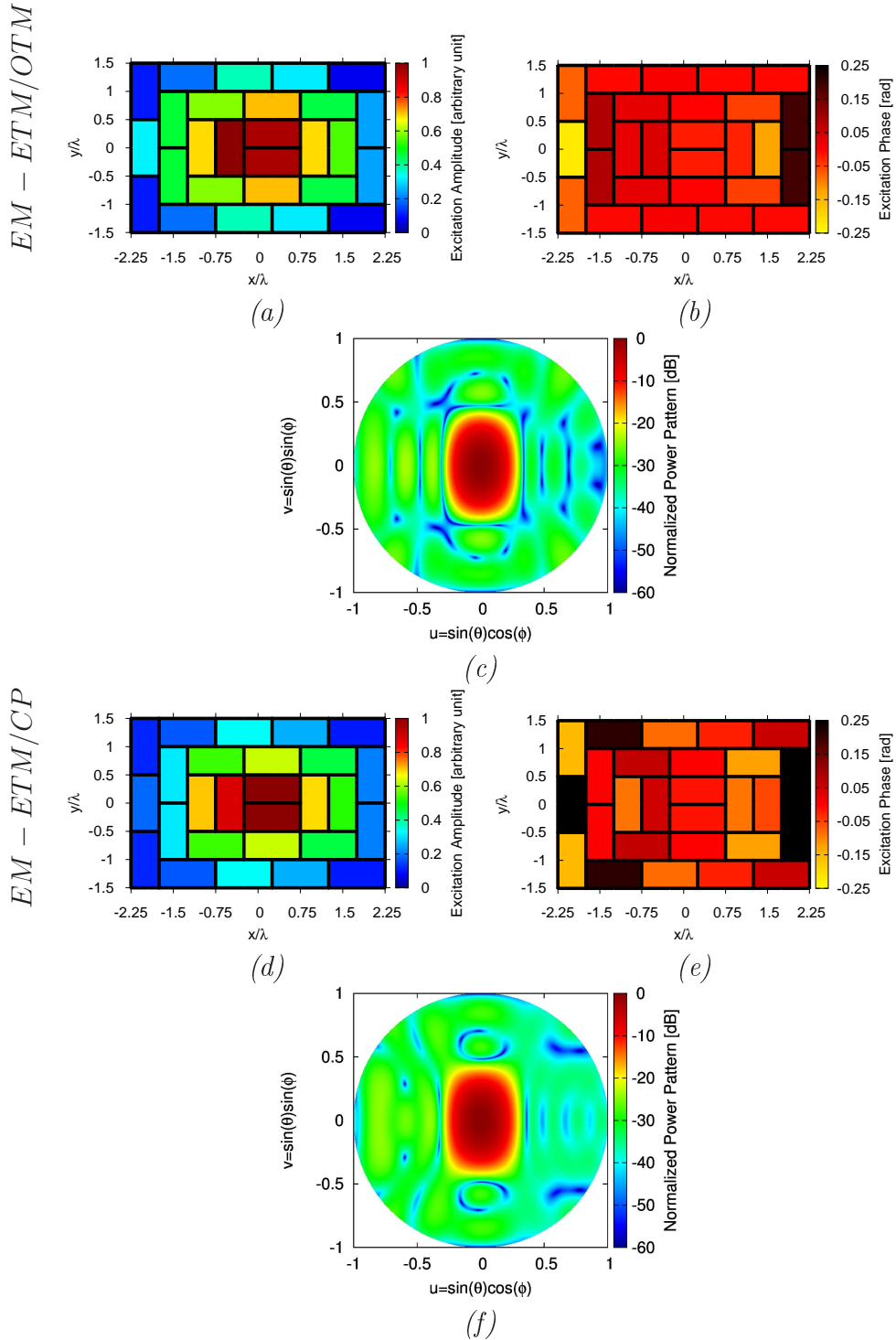
Figure 4.19: *Numerical Assessment (Medium Array, Asymmetric Mask;* $d =$ 0.5λ, $M \times N = 6 \times 9$ $N_{tot} = 54$, $T \simeq 8.2 \times 10^5$) - $(a)(d)$ The tiles amplitudes excitations coefficients, $(b)(e)$ the tiles phase excitations coefficients and $(c)(f)$ the respective top-view power patterns of the $EM - ETM$ and $EM - OTM$ optimal solution $(a)(b)(c)$, and the $EM - ETM/CP$ solution $(d)(e)(f)$.

(a)   (b)
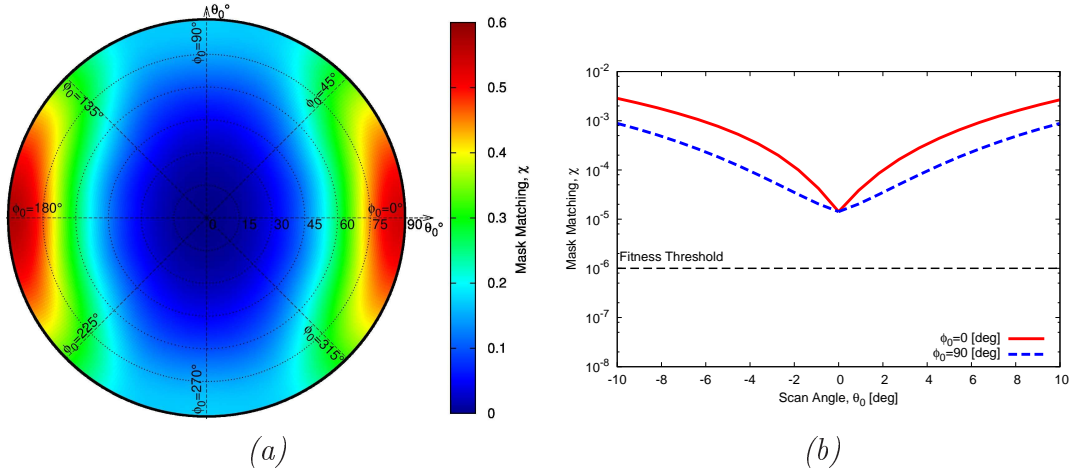
Figure 4.20: *Numerical Assessment (Medium Array, Asymmetric Mask; $d =$
0.5λ, $M \times N = 6 \times 9$ $N_{tot} = 54$, $T \simeq 8.2 \times 10^5$) - The mask matching map,
evaluated when steering the beam of the $EM - ETM/CP$ solution, within a
scan cone.*

sized power pattern. In this case the cardinality of the solution space equals
to $T = 4.9098 \times 10^{35}$, which is a too large for an exhaustive exploration, con-
sequently, the $EM - OTM$ has been chosen in order to search for the optimal
tiling in a feasible amount of time. Indeed, 10 different GA optimizations have
been executed considering $U = 800$ individuals, $K = 1000$ iterations, $p_c = 0.9$
and $p_m = 0.01$, for a total simulation time equal to $\Delta t = 16 : 42 : 30$ [h:min:sec].
The fitness of all the executed simulations are reported in Fig. 4.23(a) as
function of the iteration index. As can be seen, all the GA simulations con-
verges to cost-functions values within the interval $[2.0 \times 10^{-6}, 1.8 \times 10^{-6}]$. The
50% of the executed GA simulations converges to the same best solution hav-
ing a matching with the mask equal to $\chi\left(\underline{C}^{EM-OTM}; \underline{\alpha}^{EM-OTM}, \underline{\beta}^{EM-OTM}\right) =$
1.8×10^{-6} (Tab. 4.5). The $EM-$optimal tiling, together with the ampli-
tude and phase excitation coefficients, are reported in Fig. 4.24(a)-(b), respec-
tively, while the top view power pattern is reported in Fig. 4.24(c). Even
if the "bare" $EM - OTM$ solution does not match completely the mask, the
$EM-OTM/CP$ successfully lowers the mask matching below the fitness thresh-
old [$\chi\left(\underline{C}^{EM-OTM}; \underline{\alpha}^{EM-OTM/CP}, \underline{\beta}^{EM-E=OTM/CP}\right) = 6.2 \times 10^{-9}$, Tab. 4.5].
Finally, the mask matching has been evaluated varying the beam scanning di-
rection, graphically shown in the diagram of Fig. 4.25(a), together with a focus
in the nearby of the boresight direction along the $\phi_0 = 0$ [deg] and $\phi_0 = 90$ [deg]
planes reported in Fig. 4.25(b).
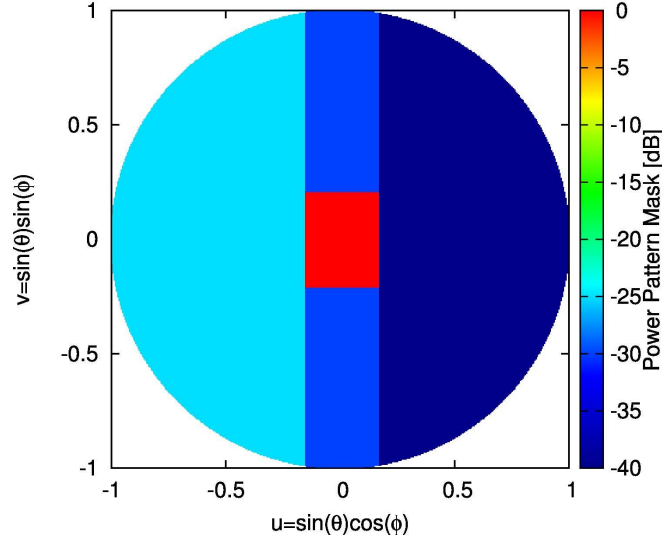
Figure 4.21: *Numerical Assessment (Large Array, Asymmetric Mask; $d = 0.5\lambda$,
$M \times N = 15 \times 20 \; N_{tot} = 300, \; T \simeq 4.9 \times 10^{35}$) - The power mask $M(u,v)$ defining
the constraints for the synthesis of an $M \times N = 6 \times 9$ array of isotropic elements.*

Table 4.5: *Numerical Assessment (Large Array, Asymmetric Mask; $d = 0.5\lambda$,
$M \times N = 15 \times 20 \; N_{tot} = 300, \; T \simeq 4.9 \times 10^{35}$) - Measured radiation indexes
(SLL, D, $HPBW_{az}$, and $HPBW_{el}$), mask matching $\chi[P(u,v)]$ of the reference
and optimized tilings patterns, and timings of the optimizations.*

	SLL [dB]	D [dBi]	$HPBW_{az}$ [deg]	$HPBW_{el}$ [deg]	χ -	Δt [h:min:sec]
	$M \times N = 15 \times 20 \; Asymmetric \, Mask$	
Reference	-25.00	28.27	6.50	8.60	9.57×10^{-9}	$02:59:03$
$EM - OTM$	-24.73	28.31	6.48	8.56	1.80×10^{-6}	$04:28:29$
$EM - OTM/CP$	-25.00	28.24	6.51	8.60	6.20×10^{-9}	$02:07:07$

(a)

(b)

(c)
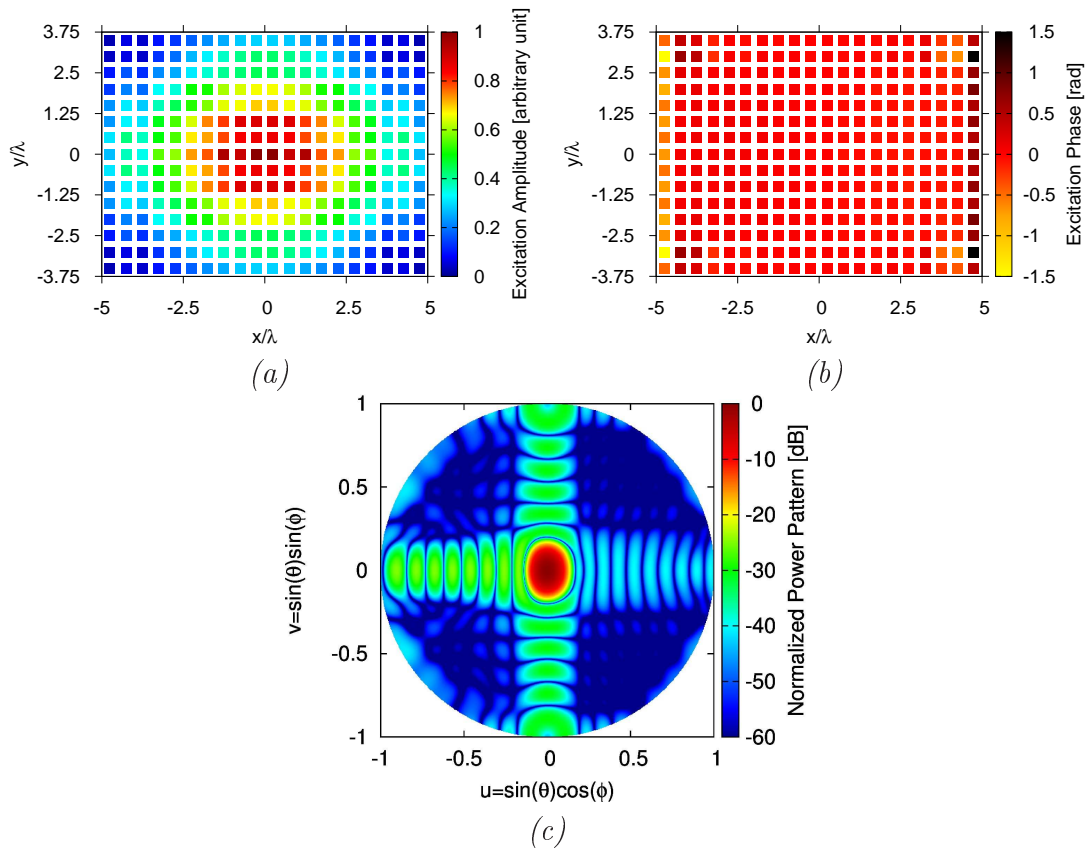
Figure 4.22: *Numerical Assessment (Large Array, Asymmetric Mask*; $d = 0.5\lambda$, $M \times N = 15 \times 20$ $N_{tot} = 300$, $T \simeq 4.9 \times 10^{35}$) - The reference solution of the fully-populated array obtained through a CP optimization. (a) The amplitude coefficients, (b) the phase coefficients, and (c) the top-view power pattern.

(a)

(b)

(c)
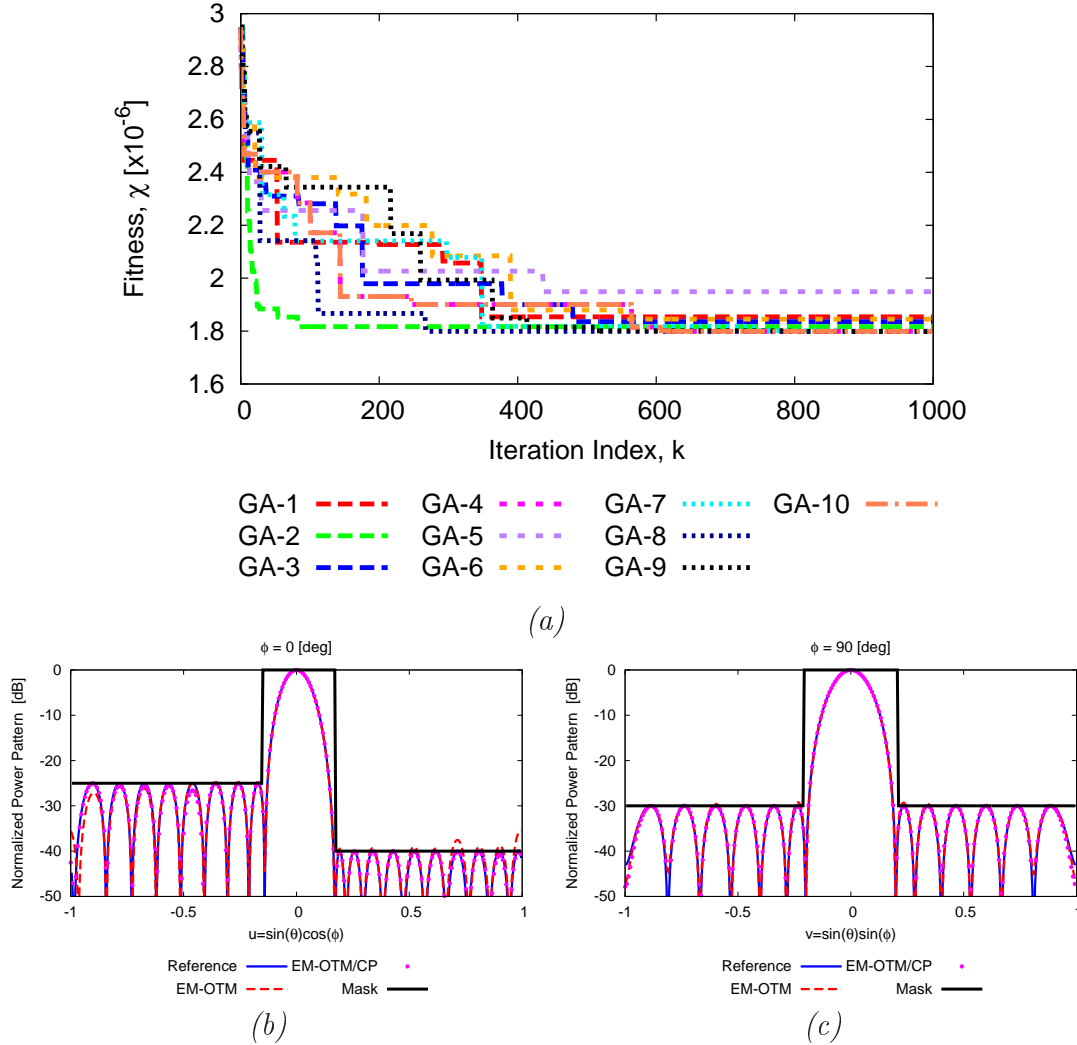
Figure 4.23: *Numerical Assessment (Large Array, Asymmetric Mask*; $d = 0.5\lambda$, $M \times N = 15 \times 20$ $N_{tot} = 300$, $T \simeq 4.9 \times 10^{35}$) - (*a*) The $EM - OTM$ simulation cost function evaluations for the 10 GA simulation runs. (*b*)(*c*) The power pattern cuts along the $u = u_0 = 0.0$ and $v = v_0 = 0.0$ plane of the $EM - OTM$ optimal solutions and the $EM - OTM/CP$, as compared to the power mask.

(a)

(b)

(c)

(d)

(e)

(f)
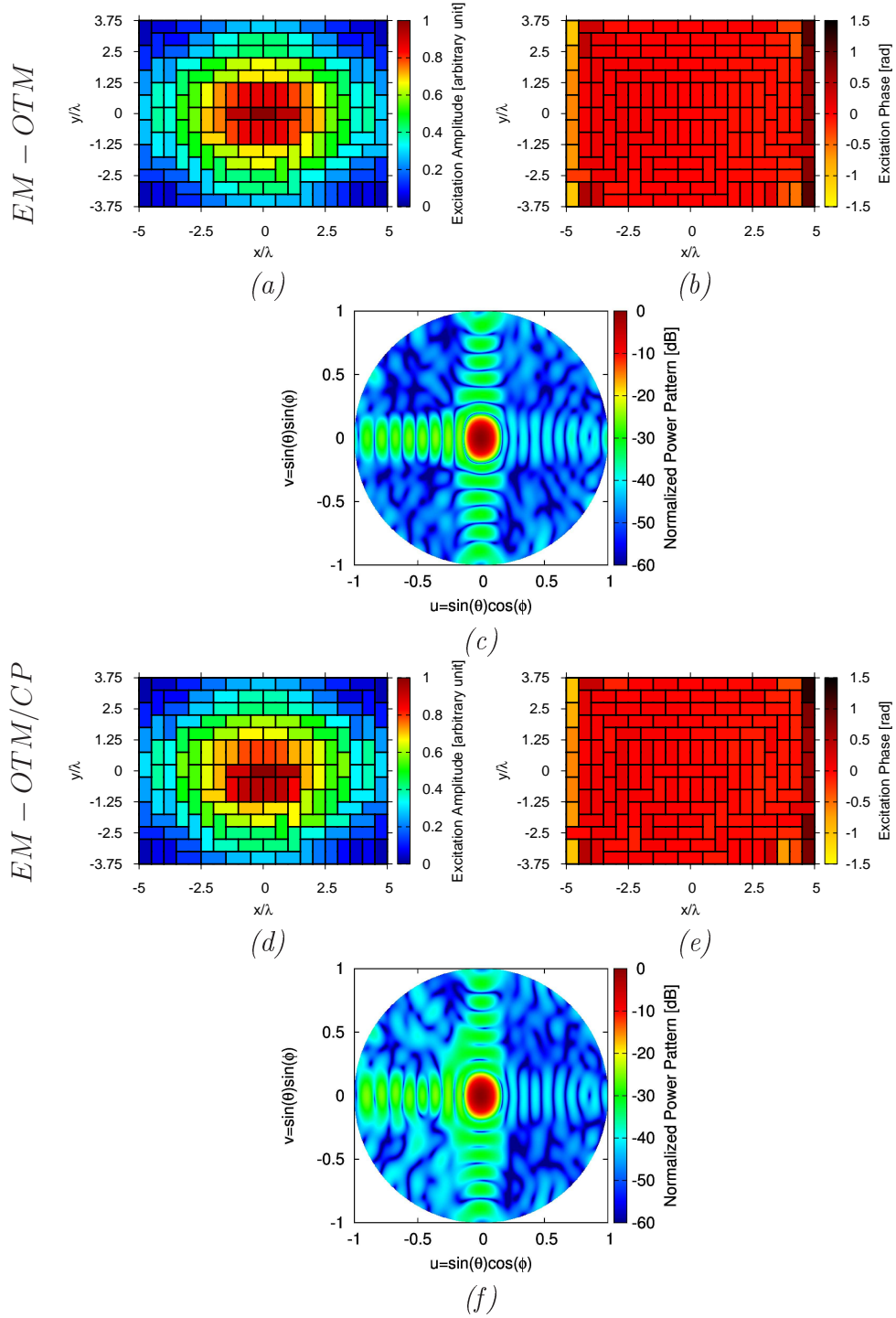
Figure 4.24: *Numerical Assessment (Large Array, Asymmetric Mask*; $d = 0.5\lambda$,
$M \times N = 15 \times 20$ $N_{tot} = 300$, $T \simeq 4.9 \times 10^{35}$) - $(a)(d)$ The tiles amplitudes
excitations coefficients, $(b)(e)$ the tiles phase excitations coefficients and $(c)(f)$
the respective top-view power patterns of the $EM - OTM$ optimal solution
(a)-(c), and the $EM - OTM/CP$ solution (d)-(f).

81

(a)   (b)
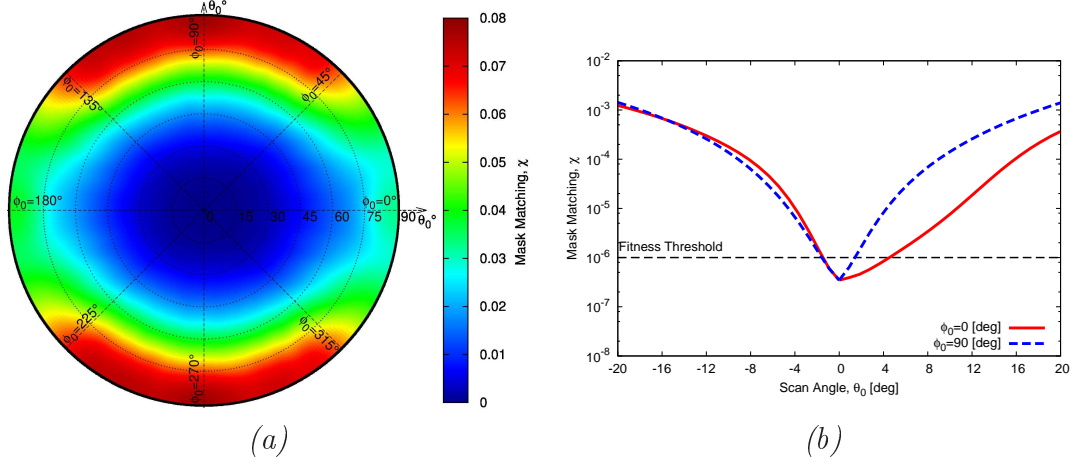
Figure 4.25: *Numerical Assessment (Large Array, Asymmetric Mask; $d = 0.5\lambda$, $M \times N = 15 \times 20$ $N_{tot} = 300$, $T \simeq 4.9 \times 10^{35}$) - The mask matching map, evaluated when steering the beam of the $EM - OTM/CP$ solution, within a scan cone.*

Table 4.6: *Numerical Assessment (*Full-Wave Simulations) - Radiation indexes *(SLL, D, $HPBW_{az}$, and $HPBW_{el}$), and mask matching $\chi\left[P\left(u,v\right)\right]$ of the tiled array power pattern, obtained simulating the entire arrays structure using a full-wave commercial software.*

$M \times N$		SLL [dB]	D [dBi]	$HPBW_{az}$ [deg]	$HPBW_{el}$ [deg]	χ -
		$Full - Wave, Patch\,Multi - Layer$				
4×5	$ETM - CP$	-22.91	16.29	23.76	28.94	1.77×10^{-8}
	$EM - ETM/CP$	-21.86	16.14	24.04	29.15	1.29×10^{-5}
	$EM - ETM$	-19.68	16.54	22.90	28.54	2.37×10^{-5}
6×9	$EM - ETM/CP$	-24.69	19.80	14.43	21.09	6.91×10^{-6}
	$EM - ETM$	-24.90	20.06	13.98	20.93	3.58×10^{-5}
15×20	$EM - OTM/CP$	-25.08	27.20	6.42	8.56	1.88×10^{-8}
	$EM - OTM$	-24.86	27.00	6.40	8.50	9.19×10^{-8}
		$Full - Wave, Patch\,Spline$				
4×5	$ETM - CP$	-21.38	17.19	24.37	28.71	0.0
	$EM - ETM/CP$	-21.38	17.06	24.51	29.12	1.42×10^{-6}
	$EM - ETM$	-19.46	17.41	23.65	28.28	2.38×10^{-4}
6×9	$EM - ETM/CP$	-25.22	20.08	14.50	21.00	1.09×10^{-6}
	$EM - ETM$	-24.60	21.10	14.20	20.80	5.94×10^{-5}
15×20	$EM - OTM/CP$	-25.30	28.40	6.40	8.50	5.62×10^{-7}
	$EM - OTM$	-25.04	28.40	6.40	8.40	1.28×10^{-6}
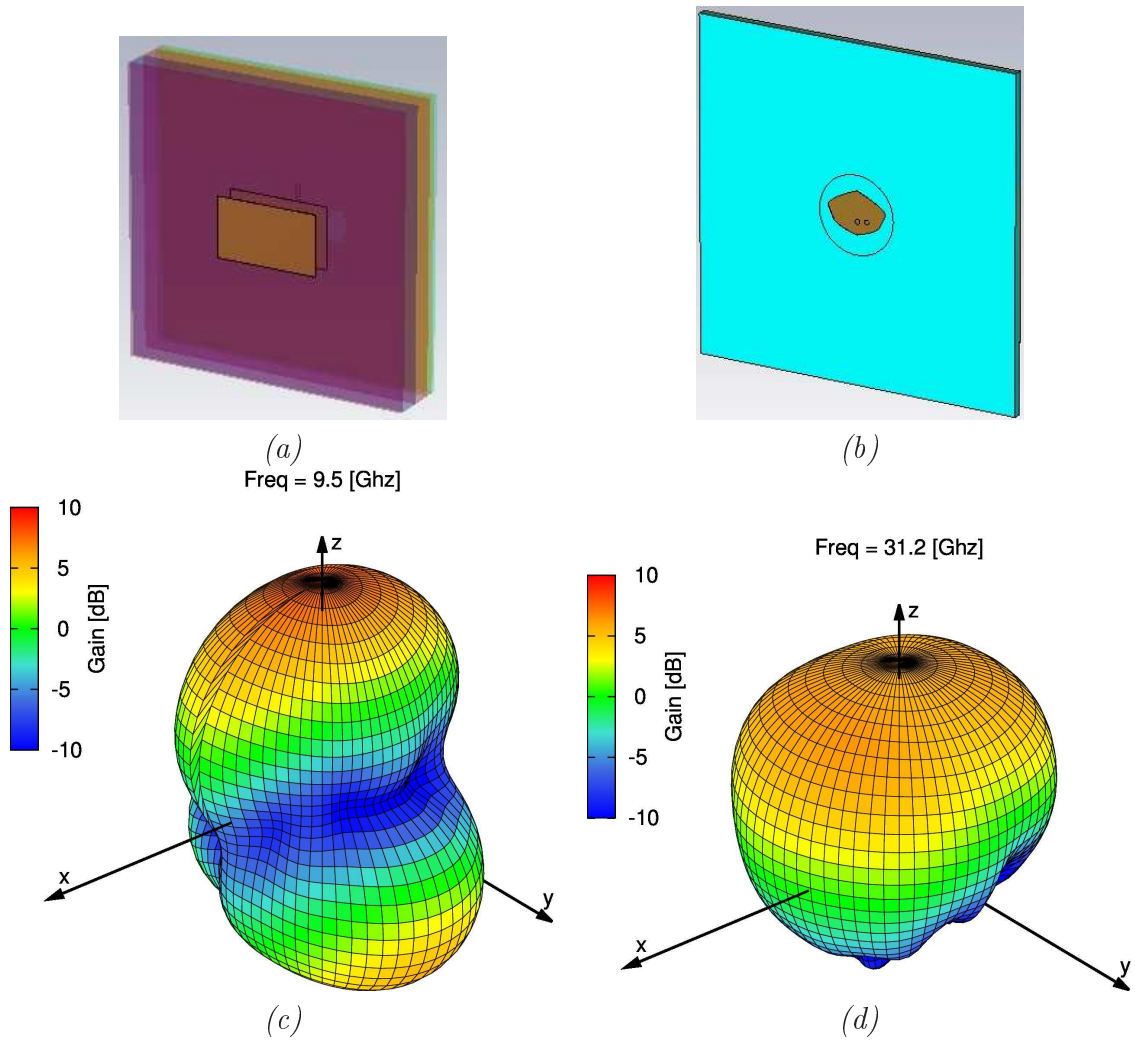
Figure 4.26: *Numerical Assessment* (*Full-Wave Simulations*) - (*a*) The model of
the multi-layer patch antenna and (*b*) the cavity backed spline patch antenna
considered for the full-wave simulations.
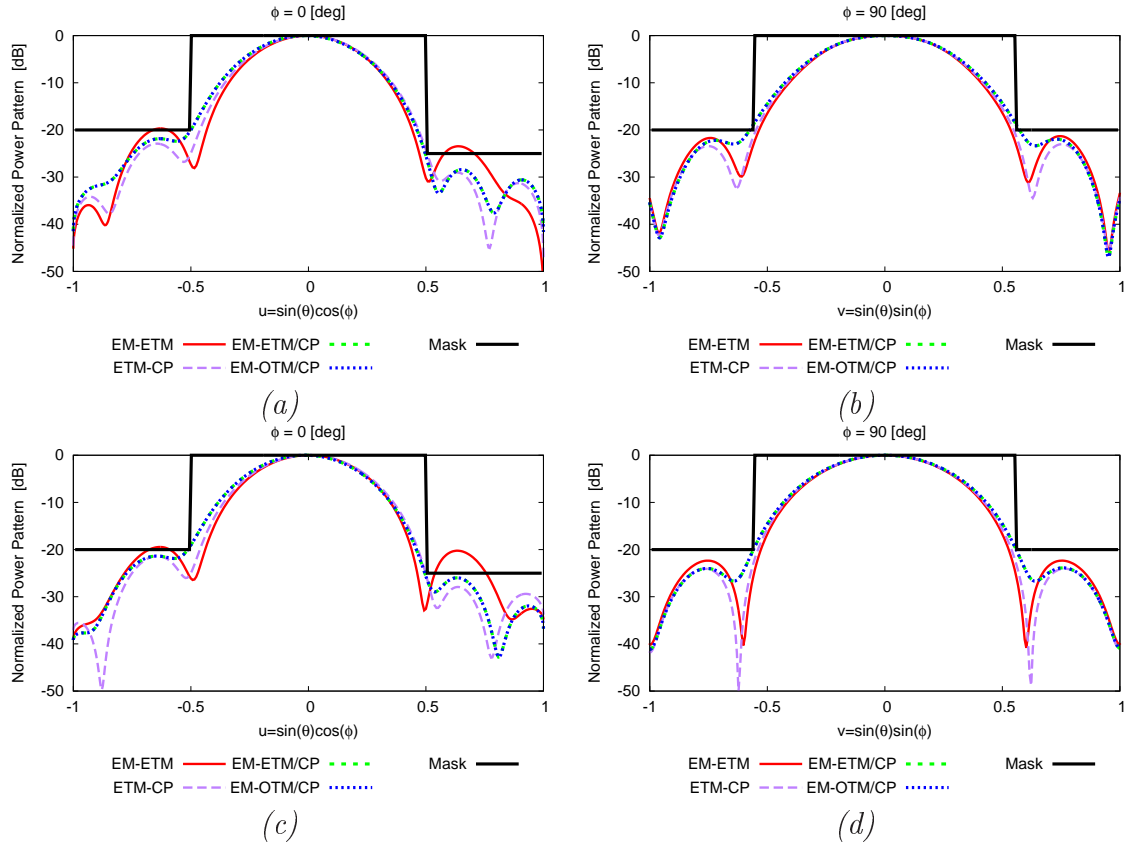
Figure 4.27: *Numerical Assessment (Full-Wave Simulations*; $d = 0.5\lambda$, $M \times N = 5 \times 4$ $N_{tot} = 20$) - The normalized power pattern cuts along $(a)(c)$ the $u = u_0 = 0.0$ and $(b)(d)$ $v = v_0 = 0.0$ planes of the $EM - ETM$, $CP - ETM$, $EM - ETM/CP$, and $EM - OTM/CP$ methods, compared to the reference mask, obtained using the full-wave solver when considering $(a)(b)$ the aperture-coupled multi-layered patch antenna and $(c)(d)$ the cavity-backed spline patch antenna.
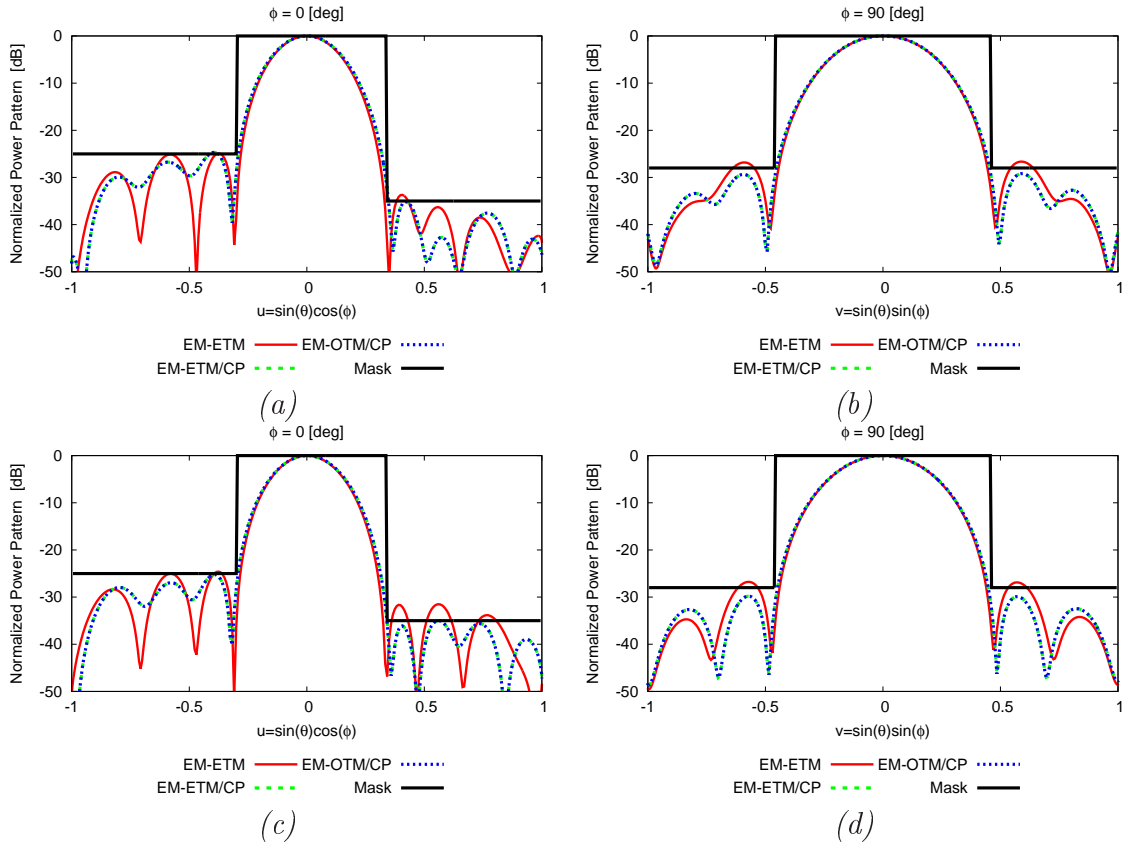
Figure 4.28: *Numerical Assessment (Full-Wave Simulations; $d = 0.5\lambda$, $M \times N = 6 \times 9$ $N_{tot} = 54$) - The normalized power pattern cuts along $(a)(c)$ the $u = u_0 = 0.0$ and $(b)(d)$ $v = v_0 = 0.0$ planes of the $EM - ETM$, $EM - ETM/CP$, and $EM - OTM/CP$ methods, compared to the reference mask, obtained using the full-wave solver when considering $(a)(b)$ the aperture-coupled multi-layered patch antenna and $(c)(d)$ the cavity-backed spline patch antenna.*
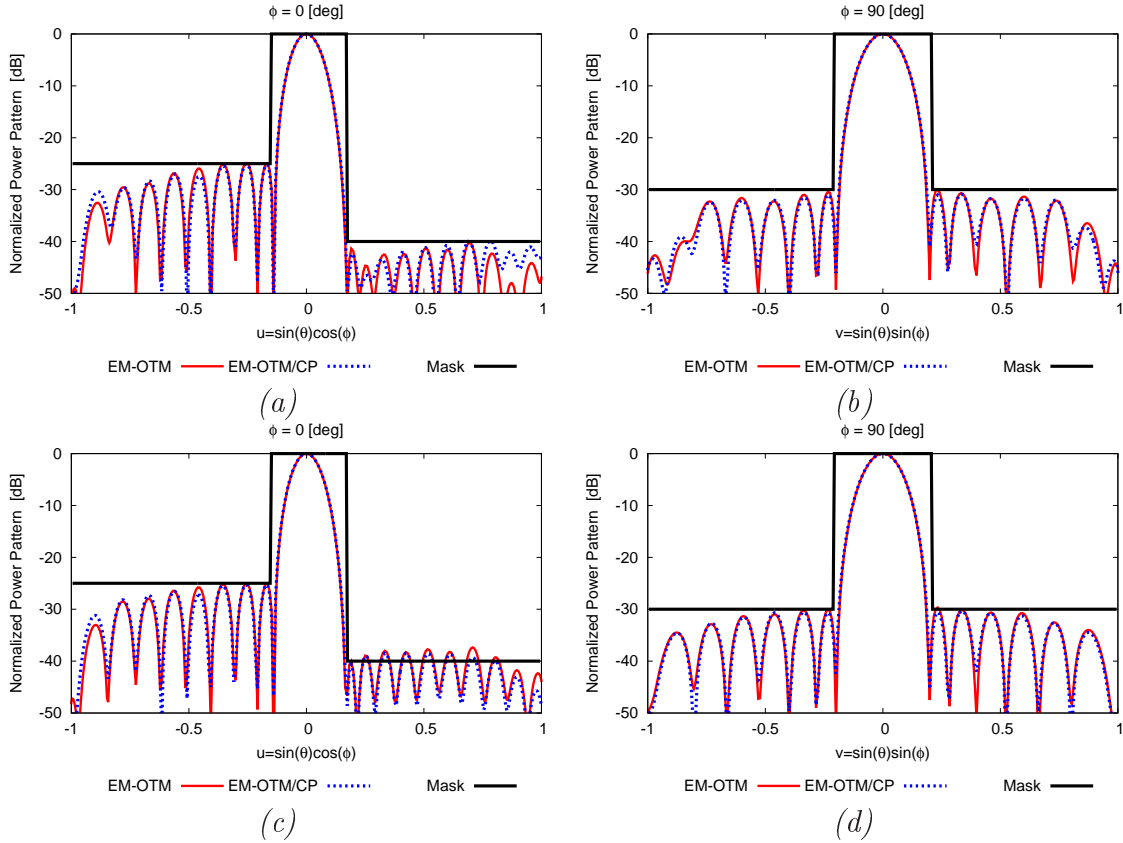
Figure 4.29: *Numerical Assessment (Full-Wave Simulations*; $d = 0.5\lambda$, $M \times N = 15 \times 20$ $N_{tot} = 300$) - The normalized power pattern cuts along $(a)(c)$ the $u = u_0 = 0.0$ and $(b)(d)$ $v = v_0 = 0.0$ planes of the $EM - OTM$, and $EM - OTM/CP$ methods, compared to the reference mask, obtained using the full-wave solver when considering $(a)(b)$ the aperture-coupled multi-layered patch antenna and $(c)(d)$ the cavity-backed spline patch antenna.

4.4.4 Reliability Assessment

In order to assess the reliability of the optimized solutions when considering real radiating elements, a set of test cases selected among the small, medium and large arrays of the previous sub-section, have been simulated using a commercial full-wave software. Two different patch antenna elements, namely the multi-layered aperture coupled patch antenna [93] [Fig. 4.26(a)] and a cavity-backed spline-shaped patch [Fig. 4.26(b)] [90], have been considered. The respective gain pattern obtained simulating the single isolated element are reported in Fig. 4.26(c) and Fig. 4.26(d), respectively, showing a different radiating behaviour among the two antennas. In this case, differently from the reliability assessment performed in Sec. 3.4.1, the entire array structure has been simulated, including the ground plane, and the microstrip antennas substrates. The power pattern cuts along the $\phi_0 = 0$ [deg] and $\phi_0 = 90$ [deg] planes of the simulated small $N \times M = 4 \times 5$ array, partitioned according to the tiling configuration obtained from the $EM - ETM$, $ETM - CP$, $EM - ETM/CP$ and $EM - OTM/CP$ methods, when considering the asymmetric power mask of Fig. 4.6, are shown in Fig. 4.27 as compared to the reference synthesis mask. As can be seen, the real power pattern corresponding to the $ETM - CP$ array, shows a good matching with the mask for both two radiating elements [$\chi\left(\mathbf{c}^{ETM-CP}; \boldsymbol{\alpha}^{ETM-CP}, \boldsymbol{\beta}^{ETM-CP}\right)\big|_{Multi-Layer}^{5\times4} = 1.77 \times 10^{-8}$ and $\chi\left(\mathbf{c}^{ETM-CP}; \boldsymbol{\alpha}^{ETM-CP}, \boldsymbol{\beta}^{ETM-CP}\right)\big|_{Spline}^{5\times4} = 0.0$, Tab. 4.6], while the $EM - ETM/CP$ real array pattern slightly violates the mask along the elevation plane when considering the multi-layered patch [Fig. 4.27(c)] ($\chi\left(\mathbf{c}^{EM-ETM}; \boldsymbol{\alpha}^{EM-ETM/CP}, \boldsymbol{\beta}^{EM-ETM/CP}\right)\big|_{Multi-Layer}^{5\times4} = 1.29\times10^{-5}$, Tab. 4.6). The mask violation is instead much more evident when using the "bare" $EM - ETM$ solution (i.e without re-optimizing the sub-array coefficients) with a mask matching equal to $\chi\left(\mathbf{c}^{EM-ETM}; \boldsymbol{\alpha}^{EM-ETM}, \boldsymbol{\beta}^{EM-ETM}\right)\big|_{Multi-Layer}^{5\times4} = 2.37\times10^{-5}$ and $\chi\left(\mathbf{c}^{EM-ETM}; \boldsymbol{\alpha}^{EM-ETM}, \boldsymbol{\beta}^{EM-ETM}\right)\big|_{Spline}^{5\times4} = 2.38 \times 10^{-4}$. Similarly, both the medium ($M \times N = 6 \times 9$) and large ($M \times N = 15 \times 20$) arrays have been validated comparing the proposed approaches solutions with the mask and to the "bare" $EM - ETM$ methodology. The comparison of the power pattern cuts with the power mask are reported in Fig. 4.28 and Fig. 4.29, for the 6×9 and 15×20 arrays. Also in this cases the full-wave analysis shows very close behaviours of the radiation patterns when considering the two different patch antennas. Moreover the full-wave pattern obtained considering the solutions the proposed methods (i.e $ETM - CP$, $EM - ETM/CP$ and $EM - OTM/CP$) outperform in terms of mask matching the $EM - ETM$ solution in all the considered cases [e.g. $\chi\left(\mathbf{c}^{EM-ETM}; \boldsymbol{\alpha}^{EM-ETM/CP}, \boldsymbol{\beta}^{EM-ETM/CP}\right)\big|_{Multi-Layer}^{6\times9} = 6.91 \times 10^{-6}$ vs. $\chi\left(\mathbf{c}^{EM-ETM}; \boldsymbol{\alpha}^{EM-ETM}, \boldsymbol{\beta}^{EM-ETM}\right)\big|_{Multi-Layer}^{6\times9} = 3.58 \times 10^{-5}$ and $\chi\left(\mathbf{c}^{EM-OTM}; \boldsymbol{\alpha}^{EM-OTM/CP}, \boldsymbol{\beta}^{EM-OTM/CP}\right)\big|_{Spline}^{15\times20} = 5.62 \times 10^{-7}$ vs. $\chi\left(\mathbf{c}^{EM-ETM}; \boldsymbol{\alpha}^{EM-ETM}, \boldsymbol{\beta}^{EM-ETM}\right)\big|_{Spline}^{15\times20} = 1.28 \times 10^{-6}$, Tab. 4.6].

Chapter 5

Multi-Objective Optimization of Orthogonal Polygons by Domino-Like Tiles

In this Chapter the tiling optimization problem of orthogonal-polygon shaped apertures is addressed. With respect to standard rectangular shaped arrays, orthogonal polygon shaped arrays allows to give to the antenna an arbitrary shape, over a rectangular grid. The synthesis of tiled phased arrays radiating a pencil beam is formulated as a multi-objective problem (*MOP*), exploiting the *ETM* and *OTM* methods introduced in the previous Chapters. A set of illustrative examples validating the proposed method are finally reported.

5.1 Problem Formulation

Let us consider an arbitrary shaped aperture array and elements positioned over a rectangular lattice. The resulting array turns out to have an orthogonal polygon shape. A polygon is called *orthogonal* (or *rectilinear*) if its edges are either horizontal or vertical (i.e., if edges meet at right angles) [95][96]. An example of two orthogonal polygon shaped arrays are reported in Fig. 5.1.

Instead of the simple minimization of a single pattern parameter (e.g. SLL) here, a multi-objective optimization approach is proposed. The multi-objective problem (MOP) is defined as:

> *Multi-Objective Optimization of Arbitrary Shaped Phased Arrays* - given an array of arbitrary aperture, with elements positioned over a rectangular lattice, and two domino-like tiles (σ^V, σ^H), find the optimal tiling/clustering configuration $\mathbf{c}^{opt}$ and the corresponding sub-array weights $\boldsymbol{\alpha}^{opt}$ and $\boldsymbol{\beta}^{opt}$, such that the radiated pattern jointly fits multiple user-defined requirements $\Phi_r(\mathbf{c}; \boldsymbol{\alpha}, \boldsymbol{\beta})$, $r = 1, ..., R$, with the main lobe steered toward (θ_0, ϕ_0).

In order to comply with multiple and conflicting objectives, a set of Pareto optimal solutions will be provided to the designer who is allowed to choose the best solution according to user-defined criterion. The set of Pareto optimal solutions are obtained as:

$$\left(\mathbf{c}^{opt}; \boldsymbol{\alpha}^{opt}, \boldsymbol{\beta}^{opt}\right) = \arg \left[\min_{\mathbf{c}; \boldsymbol{\alpha}^{EM}, \boldsymbol{\beta}^{EM}} \left\{ \begin{array}{c} \Phi_1\left(\mathbf{c}; \boldsymbol{\alpha}^{EM}, \boldsymbol{\beta}^{EM}\right) \\ \vdots \\ \Phi_R\left(\mathbf{c}; \boldsymbol{\alpha}^{EM}, \boldsymbol{\beta}^{EM}\right) \end{array} \right\} \right] \quad (5.1)$$

where $\left(\boldsymbol{\alpha}^{EM}, \boldsymbol{\beta}^{EM}\right)$ are obtained according to (4.10) and (4.11).

5.2 Tilability Condition

In Sect. 3.2 it has been described the algorithm that allows to compute the "minimal" tiling of rectangular shaped arrays, based on the height function defined in [48]. The derived tiling procedure works also for arbitrary simply connected regions, provided that the area can be totally covered by the domino tiles. In [97] the following theorem is reported for the domino tilability condition of arbitrary shaped regions:

T5 : Let A be a simply connected region in the plane defined over a rectangular lattice, and let n be the number of pixels composing A. There exists an algorithm that decides tilability of A in time $O(n \log n)$.
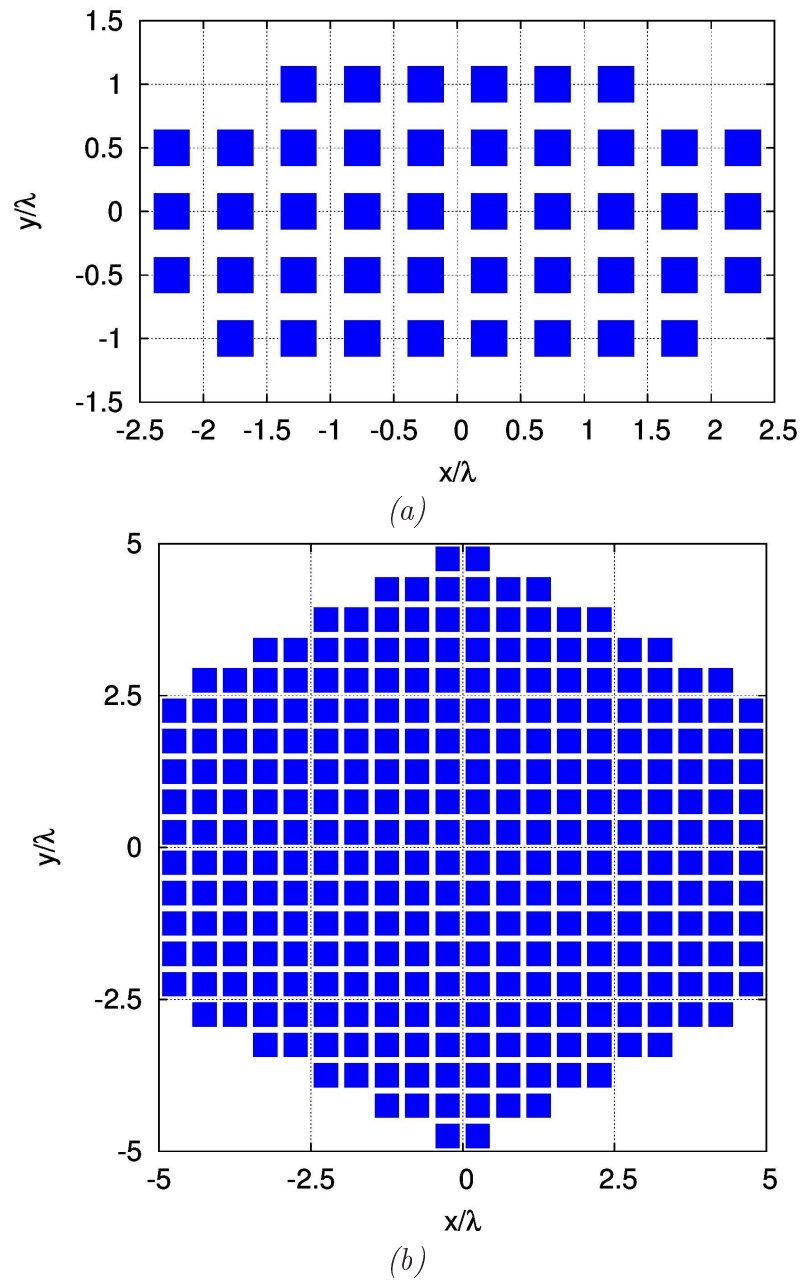
Figure 5.1: Examples of orthogonal polygon shaped arrays. *(a)* indented rectangle and *(b)* quantized hexagon.

The theorem suggests that it is always possible to verify the tilability of simple connected regions, by executing the algorithms presented in [48][53], and described in detail in Chapter 3. The algorithms allows to compute the height function on the border of the region [Sec. 3.2(A)] and on the internal vertices [Sec. 3.2(B.1)], providing the so called "minimal" tiling. Accordingly, in order to verify the tilability of an orthogonal shaped region the following two steps are required:

Step 1. *Feasibility on the boundary vertices of* A - compute the height h-value of the boundary vertices of A ($\mathbf{v}_{ext} = \{v_{mn}; [m = \{0, M\}; n = 0, ..., N] \bigcup [n = \{0, N\}; m = 0, ..., M]\}$ $\mathbf{v}_{ext} \in \partial A$ being ∂A the contour/boundary of A) and verify that the following condition holds true:

$$|h(v_{mn}) - h(v_{pg})| = 1 \tag{5.2}$$

where $v_{pg} \in \mathbf{v}_{ext}$ being a neighboring vertex of $v_{mn} \in \mathbf{v}_{ext}$. If the condition (5.2) is verified for each couple of neighboring vertices of the boundary ∂A, the following condition (*Step 2*) must be checked, otherwise it is impossible to obtain a complete tiling of A using domino tiles.

Step 2. *Feasibility on the inner vertices of* A - compute the height h-value of the inner vertices of A ($\mathbf{v}_{int}^{(t=0)} = \{v_{mn}^{(t=0)}; m = 1, ..., M-1; n = 1, ..., N-1\}$) and obtain the "minimal" tiling (i.e. $t = 0$) according to the rules defined in *A1.2* of the "*Algorithm A1*" and B1.1-4 of the "*Algorithm B1*" described in Chapter 3, and verify that the following condition holds true:

$$\left|h\left(v_{mn}^{(t=0)}\right) - h\left(v_{pg}^{(t=0)}\right)\right| = \{1, 3\} \tag{5.3}$$

$v_{pg}^{(t=0)} \in \overline{\mathbf{v}}_{mn}^{(t=0)}$ [$\overline{\mathbf{v}}_{mn}^{(t=0)} = \{v_{(m-1)n}^{(t=0)}, v_{(m+1)n}^{(t=0)}, v_{m(n-1)}^{(t=0)}, v_{m(n+1)}^{(t=0)}\}$ being the set of vertices neighbor to $v_{mn}^{(t=0)}$]. If an admissible tiling is obtained, the tilability is verified, and the whole set of complete tilings can be generated using "*Algorithm B2*" reported in Chapter 3
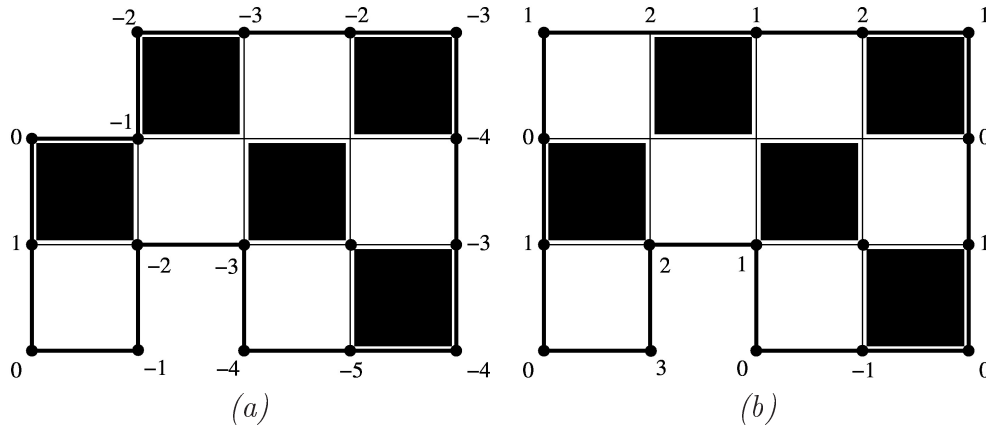
Figure 5.2: Example of tilable (a) and non-tilable (b) orthogonal polygon by dominoes, exploiting the Thurston Theorem

5.3   Estimation of the Solution Space Cardinality

For orthogonal polygon shaped apertures, for the best of the author knowledge, there is no analytic formula or theorem giving the exact number of the total admissible domino tilings T. In the following an upper and a lower bound of T are provided, exploiting the analytic formula for counting the tilings of an $M \times N$ rectangular region [eq. (3.4)]. Let us consider an arbitrary orthogonal polygon A, in order to compute the upper bound $\overline{T}$, the idea is to first compute the number of domino tilings for the smallest possible rectangle $\overline{R}$ inscribing A. Consequently we have that the number of tilings of A is for sure less than the number of tilings of $\overline{R}$. In order to have a sharper bound, the area obtained as the complement of A with respect to $\overline{R}$ is dissected into the minimum number of rectangles and the respective number of domino tilings are computed and subtracted from $\overline{T}$. Let us refer to $T(M, N)$ as the number of domino tilings of an $M \times N$ rectangle, accordingly, the upper bound $\overline{T}$ is obtained as

$$\overline{T} = T\left(\overline{M}, \overline{N}\right) - \sum_{j=1}^{J} T\left(\overline{M}_j, \overline{N}_j\right) \tag{5.4}$$

$\overline{M}$ and $\overline{N}$ being the edge of the smallest rectangle inscribing A and $T\left(\overline{M}_j, \overline{N}_j\right)$, $ij = 1, ..., J$ the number of tiling of J rectangles obtained as the complement of A with respect to $\overline{R}$ and the $\overline{M} \times \overline{N}$ rectangle;

In a similar way, the lower bound $\underline{T}$ is obtained as

$$\sum_{j=1}^{J} T\left(\underline{M}_j, \underline{N}_j\right) \tag{5.5}$$

, being $T\left(\underline{M}_j, \underline{N}_j\right)$, $j = 1, ..., J$ the minimum number of J rectangles, exactly covering A, without overlapping.

$T(\overline{M}, \overline{N})$

$T(\overline{M_1}, \overline{N_1})$ $T(\overline{M_2}, \overline{N_2})$

$T(\overline{M_3}, \overline{N_3})$ $T(\overline{M_4}, \overline{N_4})$

(a)

$T(\underline{M_1}, \underline{N_1})$

$T(\underline{M_2}, \underline{N_2})$

$T(\underline{M_3}, \underline{N_3})$

(b)
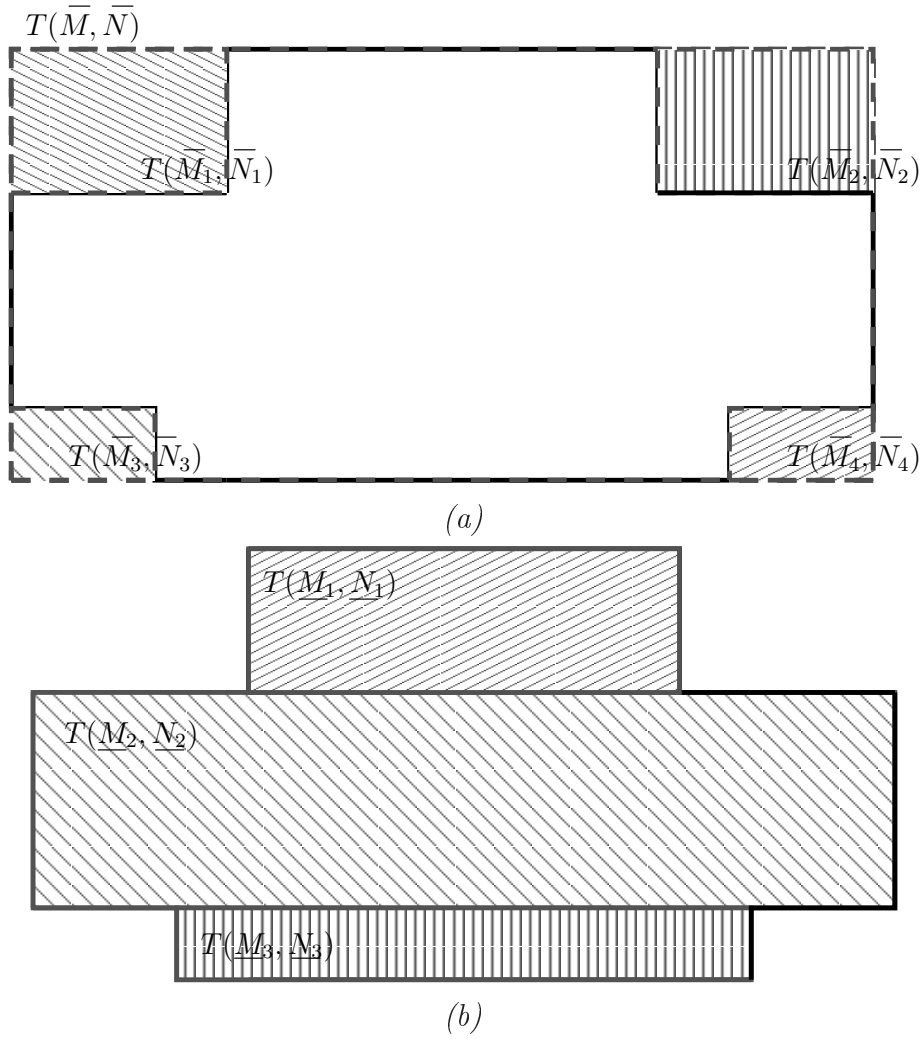
Figure 5.3: Example of estimated upper (a) and lower bound (b) of T, exploiting the cardinality theorem for rectangular regions.

5.4 Numerical Assessment

Let us consider an array of $N_{tot} = 44$ elements, located over a square lattice, equally spaced by $d_x = d_y = \lambda/2$ and positioned according to the arbitrary shape shown in Fig. 5.4(a). The reference amplitude coefficients [Fig. 5.4(a)] have been computed according to a gaussian distribution in order to obtain a power pattern with an SLL equal to $SLL = -30.20$ [dB] [Fig. 5.4(b)] and the main beam pointing toward $(\theta_0, \phi_0) = (0,0)$ [deg], consequently the phase coefficients of the fully populated array are set to $\beta_n^{ref} = 0$, $n = 1, ..., N_{tot}$. By using eq. (5.4) and eq. (5.5), the number of domino tilings is estimated within $573 < T < 1.859 \times 10^5$, which allows an exhaustive search in a feasible computational time. The $ETM-MOP$ optimization has been executed considering as a first objective ($r = 1$) the SLL of the power pattern, and as second objective ($r = 2$) the half power beamwidth along the elevation plane ($HPBW_{EL}$). The simulation has been executed in $\Delta t^{ETM-MOP} = 18:05$ [min:sec] evaluating the power pattern and the respective two objective parameters (i.e. SLL and $HPBW_{EL}$) for the effective $T = 9531$ tiling solutions. Figure 5.5(a) shows the values of the cost function in the $SLL/HPBW_{EL}$ plane, together with the Pareto front solutions. The optimal tiling solution with respect to the objective $r = 1$ (*Solution 1*, Fig. 5.5) has been reported in Fig. 5.6(a) together with the respective power pattern 5.6(b) showing a $SLL = -27.11$ [dB] and an $HPBW_{EL} = 29.00$ [deg] (Tab. 5.1), while the optimal tiling solution with respect to the objective $r = 2$ (*Solution 2*, Fig. 5.5) has been reported in Fig. 5.6(c)-(d) showing a $SLL = -11.39$ [dB] and an $HPBW_{EL} = 25.29$ [deg] (Tab. 5.1). As can be noticed from Fig. 5.5, the two objective are in contrast with each other. Let us suppose that the following design requirements are assumed: $SLL^{max} \leq -20$ [dB] and $HPBW_{EL}^{max} \leq -26.2$ [deg] (Tab. 5.1). According to Fig. 5.5 the Pareto optimal solution has been selected in order to satisfy both the requirements (*i.e. Solution* 3 Fig. 5.5, $SLL = -20.20$ [dB] and $HPBW_{EL} = 26.10$ Tab. 5.1). In order to compare the three different solutions, the cuts of the power patterns along the azimuth [Fig. 5.7(a)] and elevation [Fig. 5.7(b)] planes have been reported together with a detail of the main beam along the elevation plane [Fig. 5.7(c)].

As a second numerical example, let us consider an array of $N_{tot} = 300$ elements, located over a square lattice, equally spaced by $d_x = d_y = \lambda/2$ and positioned according to the arbitrary shape shown in Fig. 5.8(a). It is worth noting here that even if the aperture shape is very similar to a regular hexagon, it is still an orthogonal polygon, being composed by square elementary cells approximating an exact hexagon. The reference amplitude and phase coefficients [Fig. 5.8(a)-(b)] have been computed according to a gaussian distribution in order to obtain a power pattern with an SLL equal to $SLL = -20.00$ [dB] [Fig. 5.8(c)] and the main beam pointing toward $(\theta_0, \phi_0) = (30,0)$ [deg]. In order to estimate the dimension of the solution space eq. (5.5) has been used to compute $\underline{T}$, considering only the $M \times N = 14 \times 14$ square inscribed in the orthogonal

(a)

(b)
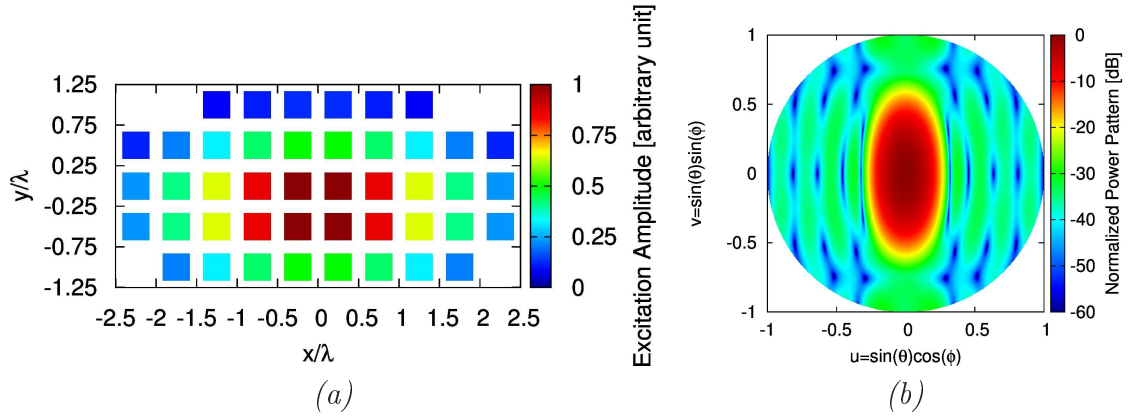
Figure 5.4: *ETM-MOP Numerical Assessment* ($N_{tot} = 44$; $d = 0.5\lambda$) - Plots of (a) the array geometry and reference excitation amplitudes (α_{mn}^{ref}; $m = 1, ..., M$; $n = 1, ..., N$) and (b) the reference power pattern, $\left| \text{AF}^{ref} (\theta, \phi) \right|^2$.
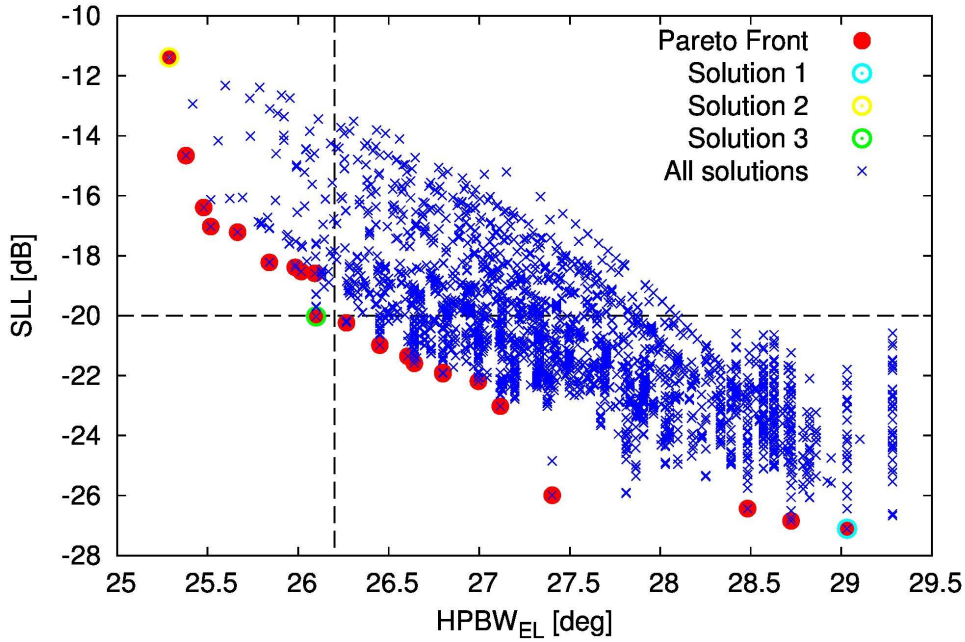
Figure 5.5: *ETM-MOP Numerical Assessment* ($N_{tot} = 44$; $d = 0.5\lambda$; $T = 9531$) - Evaluated cost functions of the exhaustive $ETM - MOP$ optimization (blue cross) considering as the first objective the SLL and as second objective the $HPBW_{EL}$ of the tiled array power pattern. The red dots are the solutions that belongs to the Pareto front.
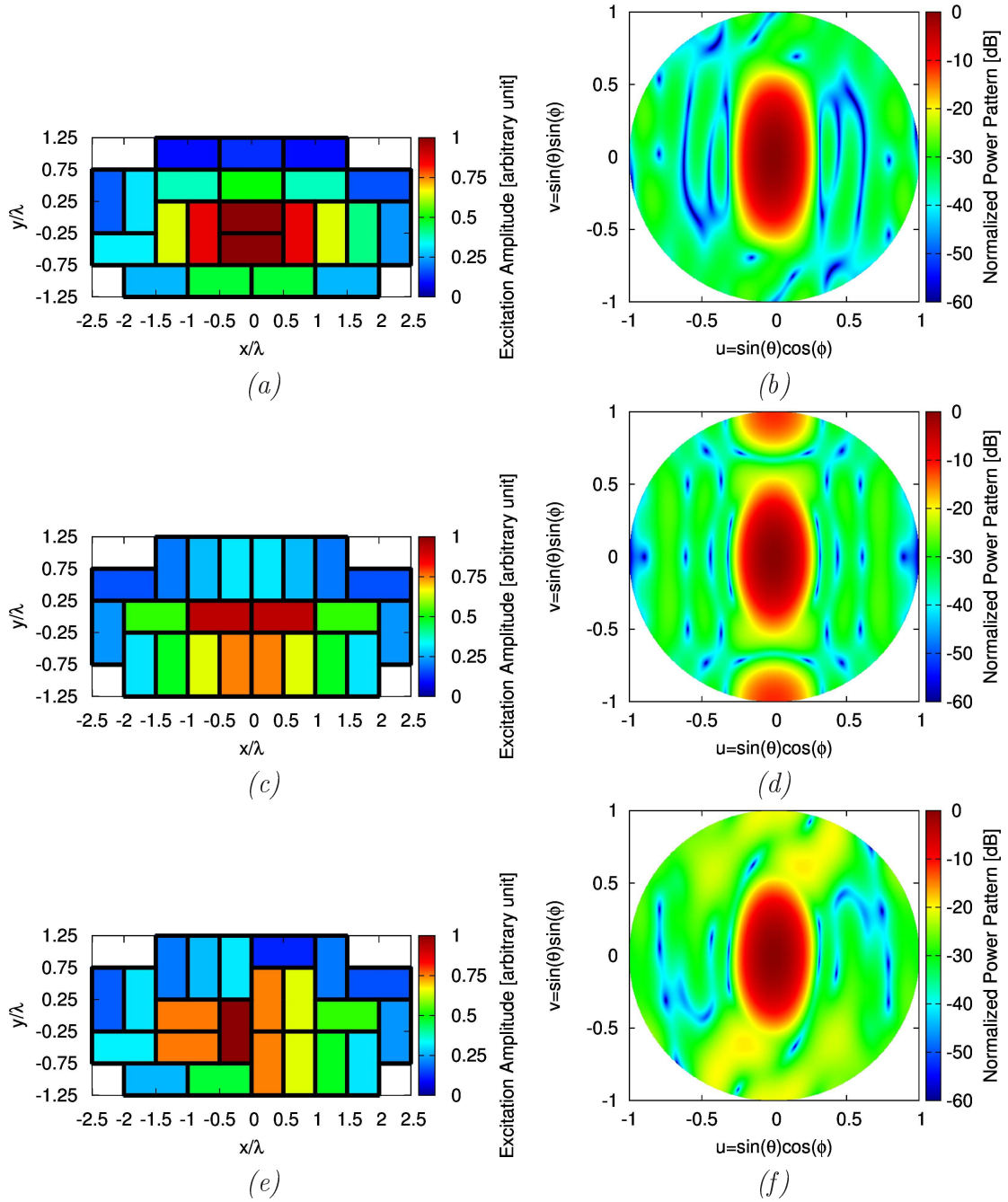
Figure 5.6: *ETM-MOP Numerical Assessment (N_{tot} = 44 ; d = 0.5λ; T = 9531)* - Plots of $(a)(c)(e)$ the tiling configurations and sub-array excitations, and $(b)(d)(f)$ the power pattern of the solutions $(a)(b)$ *Solution 1* $(t = 230)$, $(c)(d)$ *Solution 2* $(t = 5948)$, $(e)(f)$ *Solution 3* $(t = 3223)$.
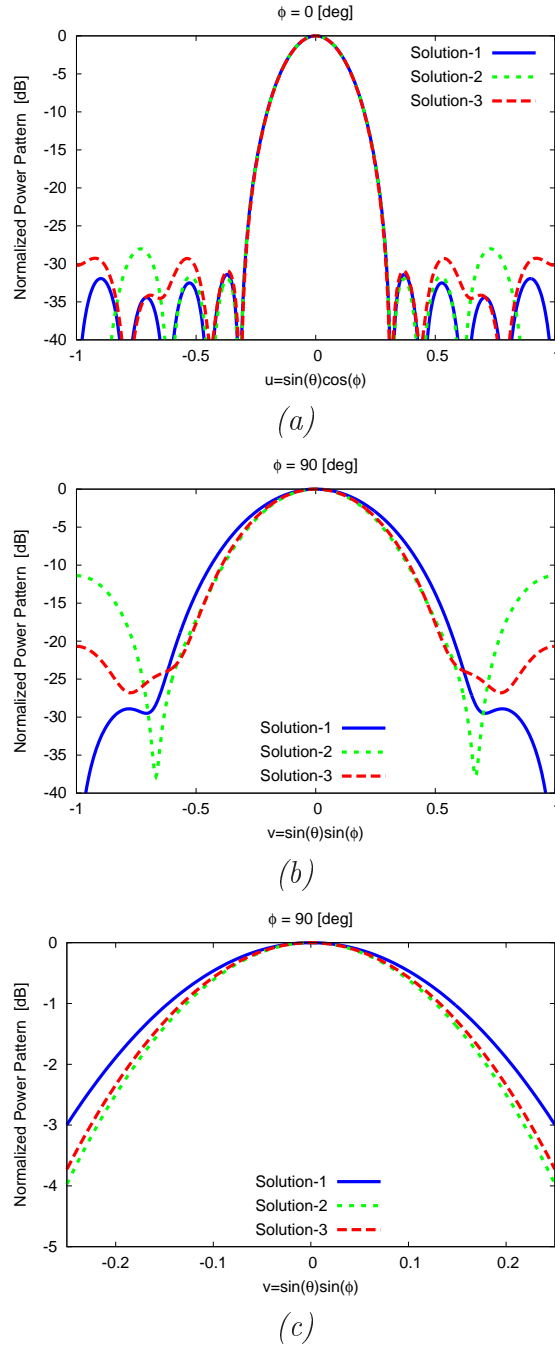
Figure 5.7: *ETM-MOP Numerical Assessment* ($M = 8$, $N = 5$; $d = 0.5\lambda$; $T = 1.4824 \times 10^4$) - Plots of *(a)* the power patterns along the $\phi = 0$ [deg] cut, *(b)* the he power patterns along the $\phi = 90$ [deg] cut and *(c)* a detail of the main beam of the power patterns along the $\phi = 90$ [deg] cut.

Table 5.1: *ETM-MOP Numerical Assessment* ($N_{tot} = 44$; $d = 0.5\lambda$; $T = 9531$) - Radiation performance (SLL, D, $HPBW_{az}$, $HPBW_{el}$) of the reference and optimized tiled solutions selected among the Pareto front of the *ETM-MOP* simulation.

	SLL [dB]	D [dBi]	$HPBW_{az}$ [deg]	$HPBW_{el}$ [deg]
Required	-20.00	$-$	$-$	26.20
Reference	-30.20	19.77	13.63	29.28
Solution -1	-27.11	19.77	13.64	29.00
Solution -2	-11.39	19.59	13.45	25.29
Solution -3	-20.20	19.90	13.40	26.10

hexagon, obtaining a lower bound equal to $\underline{T} = 1.1220 \times 10^{23}$ which is already a huge number of solutions. Being $T > \underline{T}$ an optimization based strategy is considered in this case. The $OTM-MOP$ optimization has been executed considering the NSGA-II multi-objective GA-based optimizer [98][99], considering as a first objective ($r = 1$) the SLL of the power pattern, and as second objective ($r = 2$) the half power beamwidth along the azimuth plane ($HPBW_{AZ}$). The optimization has been executed considering a population size equal to $P = 200$ and a total number of fitness evaluations (NFE) equals to $NFE = 20000$ for a total simulation time equal to $\Delta t^{OTM-MOP} = 40 : 35$ [min:sec]. Figure 5.9 *(a)* shows the values of the cost function in the $SLL/HPBW_{az}$ plane, together with the Pareto front solutions. The Pareto optimal solution has been selected according to the design requirements [$SLL^{max} \leq -16.0$ [dB] and $HPBW_{AZ}^{max} \leq -9.5$ [deg] (Tab. 5.2) and reported in Fig. 5.6 *(a)-(b)* together with the respective power pattern 5.10 *(c)* showing a $SLL = -16.00$ [dB] and an $HPBW_{EL} = 9.48$ [deg] (Tab. 5.2). The reported results show the effectiveness of a multi-objective optimization approach, that provides to the designer a flexible tool able to handle different pattern features and achieving useful trad-off solutions. Moreover the tiling of orthogonal polygons, have been successfully validated, enabling the design of arbitrary shaped arrays.

(a)

(b)

(c)
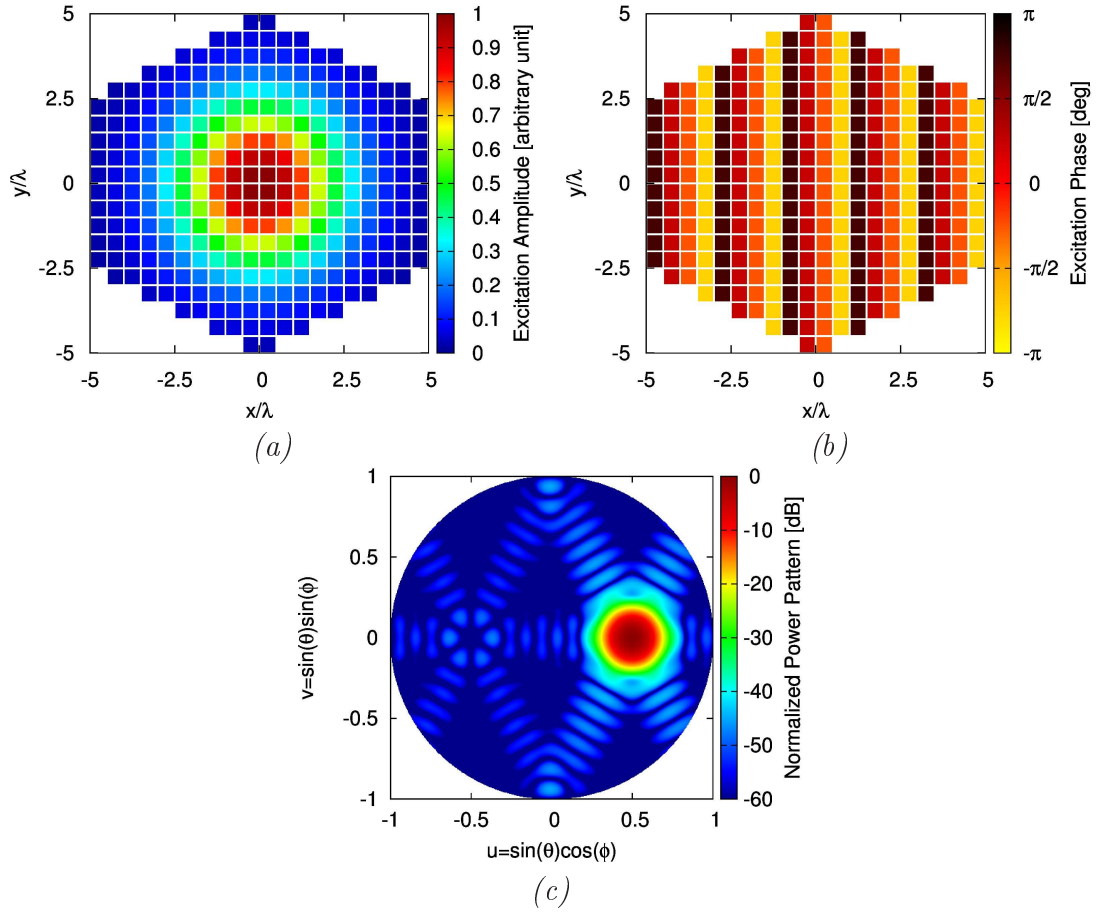
Figure 5.8: *OTM-MOP Numerical Assessment* ($N_{tot} = 40$ $d = 0.5\lambda$) - Plots of *(a)(b)* the array geometry and reference excitation *(a)* amplitudes (α_{mn}^{ref}; $m = 1, ..., M$; $n = 1, ..., N$) and *(b)* phases (β_{mn}^{ref}; $m = 1, ..., M$; $n = 1, ..., N$) and (c) the reference power pattern, $\left|\text{AF}^{ref}(\theta, \phi)\right|^2$.

Table 5.2: *OTM-MOP Numerical Assessment* ($M = 8$, $N = 5$; $d = 0.5\lambda$; $T = 1.4824 \times 10^4$) - Radiation performance (SLL, D, $HPBW_{az}$, $HPBW_{el}$) of the reference and optimized tiled solution selected among the Pareto front of the *OTM-MOP* simulation.

	SLL [dB]	D [dBi]	$HPBW_{az}$ [deg]	$HPBW_{el}$ [deg]
Required	−16.00	-	9.50	-
Reference	−20.00	25.86	10.50	8.90
$OTM - MOP$	−16.00	24.14	9.48	8.75
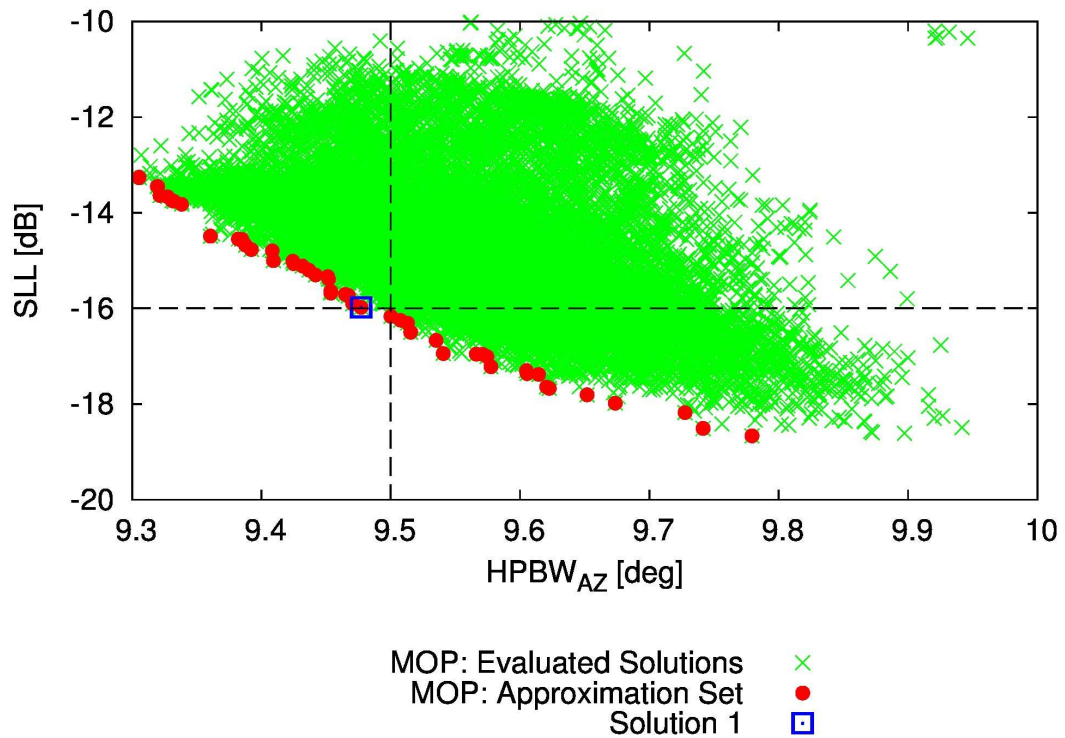
Figure 5.9: *OTM-MOP Numerical Assessment* ($M = 8$, $N = 5$; $d = 0.5\lambda$; $T = 1.4824 \times 10^4$) - Evaluated cost functions of the exhaustive $OTM - MOP$ optimization (green cross) considering as the first objective the SLL and as second objective the $HPBW_{AZ}$ of the tiled array power pattern. The red dots are the solutions that belongs to the Pareto front.
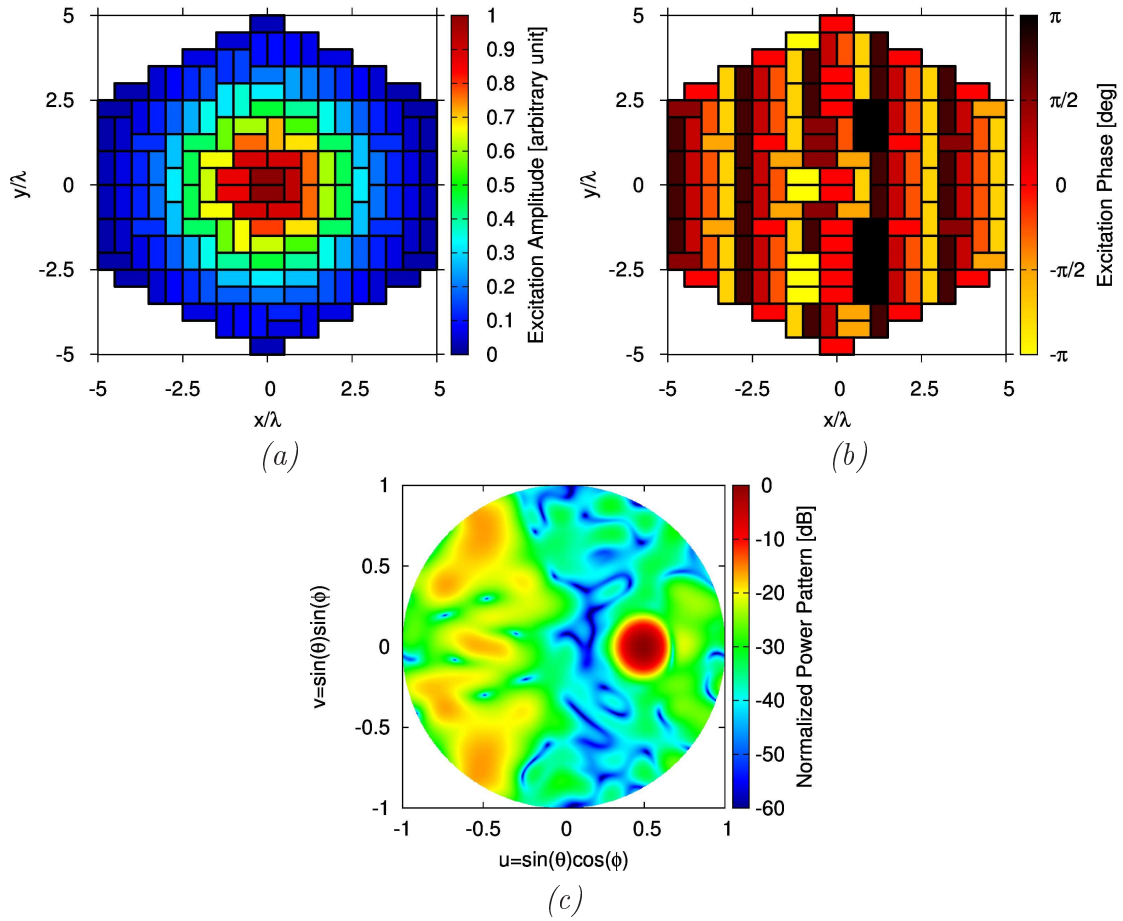
Figure 5.10: *OTM-MOP Numerical Assessment* ($N_{tot} = 40\ d = 0.5\lambda$) - Plots of *(a)(b)* the tiling configurations and sub-array *(a)* amplitude and *(b)* phase coefficients, and (c) the power pattern of the selected Pareto solution.

Chapter 6

Conclusions and Final Remarks

In this thesis a set of innovative tiling methodologies for the design of tiled phased arrays has been presented and numerically validated. The developed synthesis procedures and algorithms allow to reduce the number of control points of an array radiating mask-constrained pencil beams

1. without impacting on the feasibility and complexity of the array layout;

2. without a significant degradation of the achievable performances, for small/moderate scanning angles.

In Chapter 2 the phased array synthesis problem has been formulated, proposing theoretically unfeasible and feasible optimization strategies, and focusing, without loss of generality, to domino-like tiles. In Chapter 3 useful tiling theorems and algorithms have been reported, focusing to the problem of tiling rectangular shaped apertures with rectangular tiles, as well as a closed form formula for the enumeration of the domino tiling solution spaces. Moreover, together with the description of an optimal domino tiling generation algorithm based on an efficient encoding of the clustering configuration exploiting height function theory, two main methodologies have been introduced. A first technique, namely the *ETM*, has been developed to optimally synthesize low and medium size arrays through a suitable customization of mathematical tiling theorems and algorithms. The second one, denoted as *OTM* and based on a customized *GA*-based optimization strategy, has been derived to deal with large arrays.

The main advantages of the proposed design approach in its two different implementations are:

- the retrieval of the global optimal solution for the problem of finding the complete tiling affording the minimum *SLL* power pattern thanks to the exploitation of the mathematical theory on the optimal coverage of space surfaces through the enumerative approach (*ETM*);

- the synthesis of large clustered arrays, computationally unaffordable either by the enumerative approach (i.e., the ETM) or a standard stochastic global optimization technique, thanks to the analytic definition of a set of reference tiling arrangements and a customized GA-based algorithm allowing an effective and efficient exploration of the solution space of the complete tiling configurations, whose cardinality rapidly grows with the array size.

The numerical analysis has proved that:

- the SLLs of the solutions of the exhaustive list generated by the ETM usually vary over a wide range of values, but only a limited sub-set of tiling configurations gives performance close to that of the reference array;

- the complete tiling configuration providing the minimum/optimum SLL is generally non-unique within the list of ETM-generated solutions. This allows the array designer to select a SLL-optimal clustering that also fit additional criteria such as constraints on other radiation features and/or manufacturing characteristics;

- the OTM, as applied to synthesis problems still affordable with the ETM (i.e., small/medium size array design), proved to be able to find the optimal tiling (i.e., the same arrangement found with the ETM) with a high probability/success-rate despite the evaluation of only a fraction of the whole set of T solutions;

- the OTM, when dealing with large-scale arrays (i.e., problems with a dimensionality intractable with the ETM), is statistically robust since the convergence solutions usually lie in a narrow range of SLL values closer and closer to the reference one as the array size increases;

- the OTM and the ETM are reliable techniques for addressing pattern syntheses requiring beam steering along a generic direction (θ_0, ϕ_0).

In Chapter 5 the design of arbitrary shaped aperture arrays is addressed, considering a multi-objective optimization approach for the computation of Pareto-optimal tiling configurations. The presented numerical results positively validates the possibility to handle orthogonal-polygon shaped arrays exploiting the ETM and OTM methods of Chapter 3. The reported numerical results positively validate the ETM-MOP and OTM-MOP methods, affording flexible design tools for the optimization of small and large apertures, with the possibility to choose among a set of trade-off solutions.

In Chapter 4 an additional class of tiling optimization techniques are presented aimed at solving a mask-constrained synthesis problem. The matching between the tiled array power pattern and an user-defined power mask, defining

ideal requirements for a reference non-clustered phased array, is used as cost function of the domino tiling synthesis problem. The mask matching optimization allows to the user a flexible definition of the ideal pattern constraints, however, a perfect matching with the mask is not always assured. The proposed design methodology aims indeed at find solutions that are as close as possible to a perfect fulfilment of the constraints. According to the size of the array aperture, three different novel techniques have been proposed, namely the $ETM - CP$, $EM - ETM/CP$ and $EM - OTM/CP$, jointly optimizing the tiling configuration and the amplitude and/or phase excitation coefficients of the tiles modules. CP-based synthesis methods have been exploited in order to: (i) synthesize optimal sub-array weights, according to the clustering configuration of the tiled array; (ii) provide optimal reference excitations coefficients of the fully-populated array. A set of representative numerical results, validate the proposed methods, for small, medium and large array sizes, considering both symmetric and asymmetric masks. Moreover the robustness of the optimized tiled array when steering the main beam within the visible range, as well as the reliability assessment when considering real radiating elements, through a full-wave simulations, has been analyzed. The numerical assessment leads to the following outcomes:

- the proposed exhaustive $ETM - CP$ approach, has been effectively used for the optimization of very small arrays, but it turns out to be impractical for small/medium arrays, due to the high computational burden introduced by the optimization of the tiles control points;

- the small array design case, when considering the symmetric mask, shows that the compromise $EM - ETM/CP$-based techniques can potentially converge to the optimal $ETM - CP$ solutions, with a perfect match of the ideal design requirements. Even if a perfect matching, cannot be always ensured (e.g. as shown by the design of small/medium sized arrays considering asymmetric masks) the reported results show that the proposed $EM - ETM/CP$ and $EM - OTM/CP$ methods allows to improve the matching with the ideal mask-defined requirements, with respect to "bare" $EM - ETM$ and $EM - OTM$ optimizations.

- the reliability of the proposed methodologies has been assessed by means of full-wave simulations considering two different patch antenna elements, positively compared with respect to the "bare" $EM - ETM$ and $EM - OTM$ solutions in terms of mask matching of the radiated pattern obtained using a commercial full solver.

Future research activities, beyond the scope of the current work, will be aimed at improving the computational efficiency of both (a) the ETM and (b) the OTM to avoid the generation of tiling words corresponding to symmetric sub-array configurations. This will allow a reduction of the dimension of the solution space and, on the one hand, an extension of the range of applicability of the ETM to

larger array sizes (a), on the other, an increase of the number of samples of the solution space evaluated during the GA-evolution (b), thus a higher probability to find the optimal clustering. Moreover, the whole synthesis methodology will be extended to planar arrays that can be completely covered by tiles shapes that differs from the domino-like tiles considered in this thesis, allowing the synthesis of array having different aperture shapes (e.g. exact hexagon, circular shapes) and considering different lattices (e.g. triangular, hexagonal). Finally, a comparative assessment of the performances obtained with the the presented approaches with those achievable with alternative layouts, (e.g. sparse arrays with a smaller number of elements) will be considered in the future research.

Bibliography

[1] J. S. Herd, and M. D. Conwey, "The evolution to modern phased array architectures," *Proc. IEEE*, vol. 104, no. 3, pp. 519-529, Mar. 2016.

[2] P. Rocca, G. Oliveri, R. J. Mailloux, and A. Massa, "Unconventional phased array architectures and design methodologies - A review," *Proc. IEEE*, vol. 104, no. 3, pp. 544-560, Mar. 2016.

[3] R. L. Haupt, *Antenna Arrays: A Computational Approach.* Hoboken, NJ: John Wiley & Sons., 2010.

[4] M. Oppermann and R. Rieger. "RF modules (Tx-Rx) with multifunctional MMICs," *Microelectronics Packaging (NordPac), 2017 IMAPS Nordic Conference on. IEEE*, pp. 57-60, Jun. 2017.

[5] R. Lyon, A. Kinghorn, G. Morrison, A. Stonehouse, G. Byrne, and M. Dugan, "Active electronically scanned tiled array antenna," *IEEE International Symposium on Phased Array Systems and Technology*, pp. 160-164, Oct. 2013.

[6] R. J. Mailloux, *Phased Array Antenna Handbook*, 2nd ed. Norwood, MA: Artech House, 2005.

[7] R. J. Mailloux, "Array grating lobes due to periodic phase, amplitude and time delay quantization," *IEEE Trans. Antennas Propag.*, vol. 32, no. 12, pp. 1364-1368, Dec. 1984.

[8] R. L. Haupt, "Reducing grating lobes due to subarray amplitude tapering," *IEEE Trans. Antennas Propag.*, vol. 33, no. 8, pp. 846-850, Aug. 1985.

[9] K. S. Rao and I. Karlsson, "Low sidelobe design considerations of large linear array antennas with contiguous subarrays," *IEEE Trans. Antennas Propag.*, vol. AP-35, pp. 361- 366, 1987.

[10] V. D. Agrawal, "Grating-lobe suppression in phased arrays by subarray rotation," *IEEE Proc.*, vol. 66, pp. 347-349, Mar. 1978.

[11] P. S. Hall and M. S. Smith, "Sequentially rotated arrays with reduced sidelobe levels," *IEE Proc. Microw. Antennas Propag.*, vol. 141, pp. 321-325, Aug. 1994.

[12] A. P. Goffer, M. Kam, and P. R. Herczfeld, "Design of phased arrays in terms of random subarrays," *IEEE Trans. Antennas Propag*, vol. 42, pp. 820-826, 1994.

[13] N. Toyama, "Aperiodic array consisting of subarrays for use in small mobile earth stations," *IEEE Trans. Antennas Propag.*, vol. 53, no. 6, pp. 2004-2010, Jun. 2005.

[14] M. C. Viganó, G. Toso, G. Caille, C. Mangenot, and I. E. Lager, "Sunflower array antenna with adjustable density taper," *Int. J. Antennas Propag.*, vol. 2009, Article ID 624035, 2009.

[15] V. Pierro, V. GAldi, G. Castaldi, I. M. Pinto, and L. B. Felsen, "Radiation properties of planar antenna arrays based on certain categories of aperiodic tilings," *IEEE Trans. Antennas Propag.*, vol. 53, pp. 635-644, Feb. 2005.

[16] T. G. Spence and D. H. Werner, "Design of broadband planar arrays based on the optimization of aperiodic tilings," *IEEE Trans. Antennas Propag.*, vol. 56, pp. 76-86, Jan. 2008.

[17] R. J. Mailloux, S. G. Santarelli, and T. M. Roberts, "Wideband arrays using irregular (polyomino) shaped subarrays," *Electronics Lett.*, vol. 42, no. 18, pp. 1019-1020, Aug. 2006.

[18] R. J. Mailloux, S. G. Santarelli, T. M. Roberts, and D. Lu, "Irregular polyomino-shaped subarrays for space-based active arrays," *Int. J. Antennas Propag.*, vol. 2009, Article ID 956524, 2009.

[19] T. Isernia, M. D'Urso, and O. M. Bucci, "A simple idea for an effective subarraying of large planar sources," *IEEE Antennas Wireless Propag. Lett.*, vol. 8, pp. 169-172, 2009.

[20] A. F. Morabito, T. Isernia, M. G. Labate, M. D'Urso, and O. M. Bucci, "Direct radiating arrays for satellite communications via aperiodic tilings," *Prog. Electromagn. Res.*, vol. 93, pp. 107-124, 2009.

[21] P. Rocca, L. Manica, and A. Massa, "Synthesis of monopulse antennas through iterative contiguous partition method," *Electron. Lett.*, vol. 43, no. 16, pp. 854-856. 2007.

[22] M. D' Urso, T. Isernia, and E. F. Meliado, "An effective hybrid approach for the optimal synthesis of monopulse antennas", *IEEE Trans. Antennas Propag.*, vo. 55, no. 4, pp. 1059-1066, 2007.

[23] L. Manica, P. Rocca, A. Martini, and A. Massa, "An innovative approach based on a tree-searching algorithm for the optimal matching of independently optimum sum and difference excitations," *IEEE Trans. Antennas Propag.*, vol. 56, no. 1, pp. 58-66, Jan. 2008.

[24] R. L. Haupt, "Optimized weighting of uniform subarrays of unequal sizes," *IEEE Trans. Antennas Propag.*, vol. 55, pp. 1207-1210, 2007.

[25] S. K. Goudos, K. A. Gotsis, K. Siakavara, E. E. Vafiadis, and J. N. Sahalos, "A multi-objective approach to subarrayed linear antenna arrays design based on memetic differential evolution," *IEEE Trans. Antennas Propag.*, vol. 61, no. 6, pp. 3042-3052, Jun. 2013.

[26] G. Oliveri, M. Salucci, and A. Massa, "Synthesis of modular contiguously clustered linear arrays through a sparseness-regularized solver," *IEEE Trans. Antennas Propag.*, vol. 64, no. 10, pp. 4277-4287, Oct. 2016.

[27] B. Avser, J. Pierro, and G. M. Rebeiz, "Random feeding networks for reducing the number of phase shifters in limited-scan arrays," *IEEE Trans. Antennas Propag.*, vol. 64, no. 11, pp. 4648-4658, Nov. 2016.

[28] P. Rocca, L. Manica, R. Azaro, and A. Massa "A hybrid approach to the synthesis of subarrayed monopulse linear arrays," *IEEE Trans. Antennas Propag.*, vol. 57, no. 1, pp. 280-283, Jan. 2009.

[29] L. Manica, P. Rocca, and A. Massa, "Design of subarrayed linear and planar array antennas with SLL control based on an excitation matching approach," *IEEE Trans. Antennas Propag.*, vol. 57, no. 6, pp. 1684-1691, Jun. 2009.

[30] X. Yang, W. Xi, Y. Su, T. Zeng, T. Long, and T. K. Sarkar, "Optimization of subarray partition for large planar phased array radar based on weighted K-means clustering method *IEEE Trans. Antennas Propag.*, vol. 9, no. 8, pp. 1460-1468, Dec. 2015.

[31] P. Rocca, R. J. Mailloux, and G. Toso "GA-based optimization of irregular sub-array layouts for wideband phased arrays design," *IEEE Antennas and Wireless Propag. Letters*, vol. 14, pp. 131-134, 2015.

[32] L. Poli, G. Oliveri, P. Rocca, M. Salucci, and A. Massa, "Long-Distance WPT Unconventional Arrays Synthesis" *J. Electromagnet. Wave*, vol. 31, no. 14, pp. 1399-1420, Jul. 2017.

[33] R. Berger, "Undecidability of the Domino Problem," *Memoirs of the American Mathematical Society*, vol. 66, pp. 72, 1966.

[34] R. M. Robinson, "Undecidability and nonperiodicity for tilings of the plane," *Inventiones Mathematicae*, vol. 12, pp. 177-209, 1971.

[35] H. Wang, "Games, Logic, and Computers," *Sci. Amer.*, vol. 213, no. 5, pp. 98-106, Nov. 1965.

[36] S. W. Golomb, "Tiling with Polyominoes," *Journal of Combinatorial Theory*, vol. 1, pp. 280-296, 1966.

[37] S. W. Golomb, "Tiling with Sets of Polyominoes," *Journal of Combinatorial Theory*, vol. 9, pp. 70-71, 1970.

[38] R. L. Graham, D.E. Knuth, O. Patashnik, *Concrete Mathematics*, Addison-Wesley, New York, 1989.

[39] S. W. Golomb, *Polyominoes: Puzzles, Patterns, Problems, and Packings*, Princeton University Press, 2nd Ed., New Jersey, 1994.

[40] J. H. Conwey and J. C. Lagarias, "Tiling with polyominoes and combinatorial group theory," *J. Combinatorial Theory, Series A*, vol. 53, pp. 183-208, 1990.

[41] D. A. Klarner, *The American Mathematical Monthly*, vol. 70, no. 7, pp. 760-761, Sep. 1963.

[42] D. A. Klarner, "Packing a rectangle with congruent N-ominoes," *J. Combinatorial Theory*, vol. 7, pp. 107-115, 1969.

[43] D. Klarner, and J. Pollack, "Domino Tilings of Rectangles with Fixed Width," *Discrete Mathematics*, vol. 32, pp. 45-52, 1980.

[44] R. A. Brualdi and T. H. Foregger, "Packing boxes with harmonic bricks," *J. Combinatorial Theory*, vol. 17, pp. 81-114, 1974.

[45] F. W. Barnes, "Packing the maximum number of $m \times n$ tiles in a large $p \times q$ rectangle," *Discrete Math.*, vol. 26, pp. 93-100, 1979.

[46] P. Kasteleyn, "The statistics of dimers on a lattice I. The number of dimer arrangements on a quadratic lattice," *Physica*, vol. 27, pp. 1209-1225, 1961.

[47] J. Propp, "Enumeration of Tilings," *Enumerative Combinatorics*, CRC Press, U. Mass. Lowell, Aug. 2014.

[48] W. P. Thurston, "Conway's tiling groups," *The American Mathematical Monthly*, vol. 97, no. 8, pp. 757-773, Oct. 1990.

[49] J. C. Lagarias and D. S. Romano, "A polyomino tiling problem of Thurston and its configurational entropy," *Journal of Combinatorial Theory* Ser. A, vol. 63, no. 2, pp 338-358, 1993.

[50] J. C. Fournier, "Pavage des figures planes sans trous par des dominos: Fondement graphique de l'agorithme de Thurston, parallelisation, unicite' et decomposition," *Theoretical Computer Science*, vol. 159, pp. 105-128, 1996.

[51] S. Desreux, M. Matamala, I. Rapaport, E. Remila, "Domino tilings and related models: Space of configurations of domains with holes," *Theoretical Computer Science*, 319 (1-3), pp. 83-101, 2004.

[52] E. Remila, "The lattice structure of the set of domino tilings of a polygon," *Theoretical Comput.Sci.*, vol. 322, pp. 409-422, 2004.

[53] S. Desreux and E. Remila, "An optimal algorithm to generate tilings," *J. Discrete Alg.*, no. 4, pp. 168-180, 2006.

[54] J. Propp "Generating Random Elements of Finite Distributive Lattices," *The electronic journal of combinatorics*, no. 4, vol. 2, Jan. 1997.

[55] J. Propp, "Generalized domino-shuffling," *Theoretical Computer Science* vol. 303, no. 2, pp. 267-301, 2003.

[56] D. Beauquier, M. Nivat, E. Remila and M. Robson, "Tiling figures of the plane with two bars," *Computational Geometry*, vol. 5, pp. 1-25, 1995.

[57] E. Remila, "Tiling with bars and satisfaction of Boolean formulas." *European Journal of Combinatorics*, vol. 17, no. 5, pp. 485-491, 1996.

[58] N. G. de Bruijn, "Filling boxes with bricks", *The American Mathematical Monthly*, vol.76, pp. 37-40, 1969.

[59] C. Kenyon and R. Kenyon, "Tiling a Polygon with Rectangles," *Proceedings 33rd Annual Symposium on Foundations of Computer Science*, pp.610-619, Pittsburg, PA, 24-27 Oct. 1992.

[60] R. Kenyon, "A note on tiling with integer-sided rectangles," *J. Combin. Thy A*, vol. 74, no. 2, pp. 321-332, 1996.

[61] H. Nagamochi, and Y. Abe. "An approximation algorithm for dissecting a rectangle into rectangles with specified areas," International Symposium on Algorithms and Computation, Springer Berlin Heidelberg, 2003.

[62] E. Remila, "Tiling a polygon with two kinds of rectangles," *Discrete & Computational Geometry,* vol. 34 no. 2, pp.313-330, 2005.

[63] R. Kenyon, "Tiling a polygon with parallelograms," *Algorithmica*, vol. 9, no. 4, pp. 382-397, 1993.

[64] E. Remila, "Tiling Groups: New Applications in the Triangular Lattice," *Discrete Comput. Geom.*, vol. 20, pp. 189-204, 1998.

[65] C. Kenyon and E. Remila, "Perfect matchings in the triangular lattice," *Discrete Mathematics,* vol. 152, no. 1, pp. 191-210, 1996.

[66] S. Desreux, "An algorithm to generate exactly once every tiling with lozenges of a domain," *Theoretical Computer Science*, no. 303, pp. 375-408, 2003.

[67] M. Reid "Many L-shaped polyominoes have odd rectangular packings," *Annals of Combinatorics*, vol. 18, pp. 341- 357, 2014.

[68] D. W. Walkup, "Covering a rectangle with T-tetrominoes," *Amer. Math. Monthly*, vol. 72, pp. 986-988, 1965.

[69] M. Korn, and I. Pak, "Tiling of rectangles with T-tetrominoes," *Theoretical Computer Science*, vol. 319, no. 1-3, pp. 3-27, Jun. 2004.

[70] M. Korn, *Geometric and algebraic properties of polyomino tilings*, MIT Ph.D. thesis, 2004.

[71] C. Merino, "On the number of tilings of the rectangular board with T-tetrominoes," *Aust. J. Comb.*, vol. 14, pp. 107-114, 2008.

[72] K. K. Kayibi and S. Pirzada, "Planarity, Symmetry and Counting Tilings," *Graphs and Combinatorics*, vol. 28, no. 4, pp. 483-497, 2012.

[73] C. Lester, "Tilings with T and skew tetrominoes." *Quercus: Linfield Journal of Undergraduate Research 1.1*, 2012.

[74] K. K. Kayibi and S. Pirzada. "T-tetrominoes tiling's Markov chain mixes fast," *Theoretical Computer Science*, in press.

[75] I. Pak, "Ribbon Tile Invariants," *Trans. of the American Math. Society*, vol. 352, no. 12, pp. 5525-5561, Aug. 2000.

[76] S. Sheffield, "Ribbon tilings and multidimensional height functions," *Transactions of the American Mathematical Society,* vol. 354 no. 12, pp. 4789-4813, 2002.

[77] V. Nitica, "Every tiling of the first quadrant by ribbon L n-ominoes follows the rectangular pattern," *Open Journal of Discrete Mathematics*, vol. 5, pp. 11-25, 2015.

[78] D. Merlini, R. Sprugnoli, and M. C. Verri, "Strip Tiling and regular grammars," *Theoretical Computer Science*, vol. 242, pp. 109-124, 2000.

[79] D. Merlini, R. Sprugnoli, and M. C. Verri, "A strip-like tiling algorithm," *Theoretical Computer Science*, vol. 282, no. 2, pp. 337-352, Jun. 2002.

[80] O. Bodini, "Tiling a Rectangle with Polyominoes," *Discrete Mathematics and Theoretical Computer Science AB (DMCS)*, pp. 81-88, 2003.

[81] M. Reid, "Tile Homotopy Groups," *L'Enseignement Mathematique*, vol. 49, no. 1-2, pp. 123-155, 2003.

[82] M. Reid, "Klarner systems and tiling boxes with polyominoes," *Journal of Combinatorial Theory*, Series A, vol. 111, pp. 89-105, Jan. 2005.

[83] E. J. Janoski, "J-Omino Packings," *PhD Dissertation*. University of Delaware, 2006.

[84] F. Chavanon, M. Latapy, M. Morvan, E. Remila, L. Vuillon, "Graph encoding of 2D-gon tilings," *Theoretical Computer Science*, 346 (2-3), pp. 226-253, 2005.

[85] L. Sallows, "On Self-Tiling Tile Sets," *Mathematics Magazine*, vol. 85, no. 5, pp. 323-333, Dec. 2012.

[86] H. Holland, *Adaptation in Natural and Artificial Systems*. Ann Arbor, MI: Univ. Michigan Press, 1975.

[87] D. E. Goldberg, *Genetic Algorithms in Search, Optimization, and Machine Learning*. Boston, MA: Addison-Wesley, 1989.

[88] J. M. Johnson and Y. Rahmat-Samii, "Genetic algorithms in engineering electromagnetics," *IEEE Antennas Propag. Mag.,* vol. 39, no. 4, pp. 7-21, Aug. 1997.

[89] D. S. Weile and E. Michielssen, "Genetic algorithm optimization applied to electromagnetics: a review," *IEEE Trans. Antennas Propag.,* vol. 45, no. 3, pp. 343-353, Dec. 1997.

[90] L. Lizzi, F. Viani, R. Azaro, and A. Massa, "A PSO-driven spline-based shaping approach for ultra-wideband (UWB) antenna synthesis," *IEEE Trans. Antennas Propag.,* vol. 56, no. 8, pp. 2613-2621, Aug. 2008.

[91] R. S. Elliott, *Antenna Theory and Design*. Hoboken, NJ: John Wiley & Sons., 2003.

[92] A. Massa, G. Oliveri, M. Salucci, C. Nardin, and P. Rocca "Dealing with EM functional optimization through new generation evolutionary-based methods," IEEE Int. Conf. Numerical Electromagnetic Modeling and Optimization for RF, Microwave, and Terahertz Applications (NEMO 2014), Pavia, Italy, pp. 1-4, May 14-16, 2014.

[93] S. D. Targonski, R. B. Waterhouse, and D. M. Pozar, "Design of wide-band aperture-stacked patch microstrip antennas," *IEEE Trans. Antennas Propag.*, vol. 46, no. 9, pp. 1254-1251, Sep. 1998.

[94] P. Rocca, M. Benedetti, M. Donelli, D. Franceschini, and A. Massa, "Evolutionary optimization as applied to inverse scattering problems," *Inv. Prob.*, vol. 24, pp. 1-41, 2009.

[95] A. P. Tomas, and A. L. Bajuelos. "Generating random orthogonal polygons." *Current Topics in Artificial Intelligence.* Springer Berlin Heidelberg, pp. 364-373, 2004.

[96] Z. Su and R. Ding, "Tiling of Orthogonal Polygons with Similar Rectangles and Triangles," *J. Appl. Math. & Computing*, vol. 17, no. 1- 2, pp. 343-350, 2005.

[97] I. Pak, A. Sheffer, and M. Tassy, "Fast Domino Tileability,", *Discrete Comput. Geom.*, vol. 56, no. 2, pp. 377-394, Sep. 2016.

[98] K. Deb, A. Pratap, S. Agarwal, and T. Meyarivan, "A fast and elitist multiobjective genetic algorithm: NSGA-II," *IEEE Trans. Evol. Comput.*, vol. 6, no. 2, pp. 182-197, Apr. 2002.

[99] H. Li, and Q. Zhang, "Multiobjective optimization problems with complicated Pareto sets, MOEA/D and NSGA-II," *IEEE Trans. Evolutionary Comput.*, pp. 284-302, 2009.

[100] T. Isernia, P. Di Iorio, F. Soldovieri, "An effective approach for the optimal focusing of array fields subject to arbitrary upper bounds," *IEEE Trans. Antennas Propag.*, vol. 48, no. 12, pp. 1837-1847, Dec. 2000.

[101] O.M. Bucci, L. Caccavale, T. Isernia, "Optimal far-field focusing of uniformly spaced arrays subject to arbitrary upper bounds in nontarget directions," *IEEE Trans. Antennas Propag.*, vol. 50, no. 11, pp. 1539-1554, Nov. 2002.

[102] G. Gottardi, L. Poli, P. Rocca, A. Montanari, A. Aprile, and A. Massa, "Optimal monopulse beamforming for side-looking airborne radars," *IEEE Antennas Wireless Propag. Lett.*, vol. 16, pp. 1221-1224, 2017.